JSCSEN 76(7)947–1055(2011)

International Year of CHEMISTRY 2011

Journal of the Serbian Chemical Society

Electronic Version

VOLUME 76

No 7

BELGRADE 2011

Available on line at

www.shd.org.rs/JSCS/

The full search of JSCS is available through

DOAJ DIRECTORY OF OPEN ACCESS JOURNALS

www.doaj.org

Journal of the Serbian Chemical Society
JSCS-info@shd.org.rs • www.shd.org.rs/JSCS

J. Serb. Chem. Soc. Vol. 76, No. 7 (2011)

CONTENTS

Published by the Serbian Chemical Society
Karnegijeva 4/III, 11000 Belgrade, Serbia
Printed by the Faculty of Technology and Metallurgy
Karnegijeva 4, P.O. Box 35-03, 11120 Belgrade, Serbia

Journal of the Serbian Chemical Society
JSCS-info@shd.org.rs • www.shd.org.rs/JSCS
J. Serb. Chem. Soc. 76 (7) 947–954 (2011)
JSCS–4173
UDC 547.26'11+547.418:544.412.1
Original scientific paper

Facile and efficient conjugate additions of β-dicarbonyl compounds and nitroalkanes to 4-aryl-4-oxobut-2-enoates

XIN LV, YAOHONG ZHANG, LIEJIN ZHOU and XIAOXIA WANG*

Zhejiang Key Laboratory for Reactive Chemistry on Solid Surfaces, College of Chemistry and Life Sciences, Zhejiang Normal University, Jinhua 321004, P. R. China

(Received 9 September 2010, revised 3 January 2011)

Abstract: Facile and efficient conjugate additions of carbon nucleophiles, such as β-dicarbonyl compounds and nitroalkanes, to 4-aryl-4-oxobut-2-enoates have been achieved under simple base catalysis. A variety of multi-functional γ-keto esters could be conveniently obtained in good to excellent yields with complete regioselectivity.

Keywords: conjugate addition; multi-functional γ-keto ester; β-dicarbonyl compound; nitroalkane; 4-aryl-4-oxobut-2-enoate.

INTRODUCTION

The catalytic conjugate addition of carbon nucleophiles to electron-deficient alkenes is one of the most important synthetic strategies for direct C–C bond formation,[1–3] and many of the corresponding adducts are of great value in biological chemistry and in the field of pharmaceutical.[4]

Both β-dicarbonyl derivatives and nitroalkanes are important sources of stabilized carbanions and the employment of these C-nucleophiles for conjugate addition has drawn much attention.[4] The addition of β-dicarbonyl compounds to activated carbonyl systems could afford potential precursors for a variety of biologically active substances or medicinal intermediates;[4–6] the adducts from nitroalkanes could be conveniently converted to amines, ketones, aldehydes, hydrides, and other useful building blocks.[4,7–11]

4-Aryl-4-oxobut-2-enoates are known as biologically and medicinally important small molecules.[12] These substrates can be conveniently synthesized from readily available and low-cost materials.[12–17] In recent years, Michael addition reactions employing 4-aryl-4-oxobut-2-enoates as the acceptors have been of great interest in modern chemistry, because the corresponding multi-functionalized adducts are of potential value in synthetic or pharmaceutical

* Corresponding author. E-mail: wangxiaoxia@zjnu.cn
doi: 10.2298/JSC100909066L

areas.[18–23] For example, Han developed a practical synthesis of 2-azolyl substituted 4-oxo-4-arylbutanoates using azoles as the nucleophiles.[18] The conjugate addition between indoles and 4-aryl-4-oxobut-2-enoates facilitated by a Lewis acid was recently found.[20]

The addition of 1,3-dicarbonyl compounds to 4-aryl-4-oxobut-2-enoates could afford various synthetically or medicinally useful multi-carbonyl derivatives. For example, Tan *et al*. reported bicyclic guanidines-catalyzed Michael reaction of dimethyl malonate with fumaric derivatives, but only one example was the reaction with a 4-aryl-4-oxobut-2-enoate.[21] However, to the best of our knowledge, no systematic study on this type of addition has been reported.

Conjugate addition reactions of nitroalkanes to 4-aryl-4-oxobut-2-enoates are rare in the literature.[7,22,23] Xiao successfully employed a Cinchona alkaloid--based thiourea catalyst for the Michael addition of nitroalkanes to 4-oxo-2-enoates.[7] Tishkov *et al*. reported the 1,8-diazabicyclo[5.4.0]undec-7-ene (DBU)-catalyzed addition of nitromethane to methyl 4-phenyl-4-oxobut-2-enoate.[22] Feng and coworkers recently reported that a chiral *N*,*N*'-dioxide-Sc(OTf)$_3$ complex worked well for Michael additions of β-dicarbonyl compounds and nitromethane to 4-aryl-4-oxobut-2-enoates.[23] However, to the best of our knowledge, β-keto esters have not been employed as the C-nucleophiles for conjugate addition with 4-oxo-2-enoates.

Other approaches to these multi-functional γ-keto esters have also been developed. For example, Smirnov *et al*. reported that the reactions of 3-bromo-3--nitroacrylates with 2-phenyl-1,3-indanedione under the catalysis of triethylamine (TEA) could afford 2-[1-(alkoxycarbonyl)-2-nitroethyl]-2-phenyl-1,3-indanediones.[24] Ballini and coworkers found that polyfunctionalized nitroalkanes could be synthesized from the addition of active methylene compounds to β-nitroacrylates.[25] They also synthesized multi-functional β-nitro esters using β-nitroacrylates and silyl enol ethers as the starting materials.[26]

However, in spite of these developments, the previously described methods might suffer from harsh conditions (such as low temperatures), poor yields, narrow scopes, expensive (or special) catalysts, and/or tedious procedures. Therefore, more convenient, versatile and efficient strategies for the synthesis of multi--functional γ-keto esters derived from 4-aryl-4-oxobut-2-enoates are still in demand (Fig. 1).

Herein, as a continuation of ongoing studies on catalytic conjugate additions employing 4-aryl-4-oxobut-2-enoates as strategic starting materials, the conjugate addition of various β-dicarbonyl compounds or nitroalkanes to 4-aryl-4--oxobut-2-enoates using a common inorganic base catalyst is presented as a facile protocol to generate multi-functionalized γ-keto esters with complete regioselectivity and high efficiency.

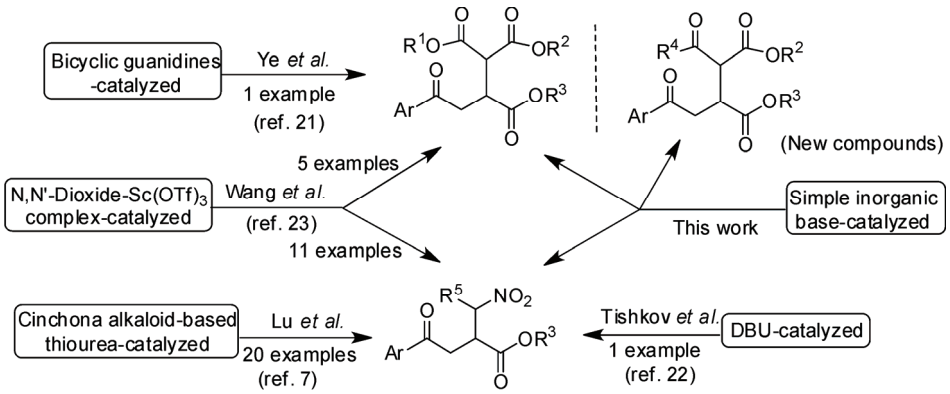

Fig. 1. Recently reported catalytic conjugate addition reactions of 4-aryl-4-oxobut-2-enoates with *β*-dicarbonyl compounds and nitroalkanes.

RESULTS AND DISCUSSION

Initially, the work focused on the catalytic conjugate addition of methyl acetoacetate **1a** to ethyl 4-phenyl-4-oxobut-2-enoate **2a**. In the first attempt performed in tetrahydrofuran, THF, with Et_3N (20 mol %) as the catalyst at room temperature, the desired product **3a** was obtained but in unsatisfactory yield (Scheme 1, Table I). Then, attempts were made to optimize the reaction conditions. Evidently, the key point in the reaction is the choice of solvent. Various solvents (THF, benzene, CH_3CN, Et_2O, CH_2Cl_2, and EtOH) were examined and the result was remarkably improved when EtOH was used as the solvent. After screening a range of bases (Et_3N, pyridine, KOH, 1,4-diazabicyclo[2.2.2]octane (DABCO), DBU and *t*-BuOK), the weak inorganic base K_2CO_3 was found to be the optimal base to promote the conjugate addition.

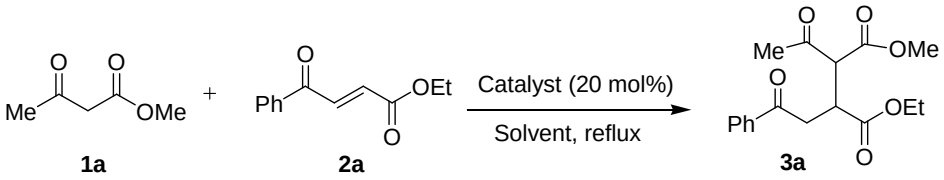

Scheme 1. The catalytic conjugate addition of methyl acetoacetate to ethyl 4-phenyl-4-oxobut-2-enoate.

Under the optimized conditions, various *β*-dicarbonyl derivatives and 4-aryl--4-oxobut-2-enoates were employed as the substrates to test the generality of the reaction (Scheme 2, Table II). Both *β*-keto esters and malonic esters undergo the conjugate additions smoothly to give the corresponding adducts in good to excellent yields within a short reaction time (within 2.5 h). Generally, neither electron--donating groups (4-Me, 3,4-dimethyl) nor electron-withdrawing groups (4-Cl,

4-Br) on the aromatic ring seemed to exert an apparent influence on the efficiency of the reaction (entries **3**, **5**, **7**, **8** and **10**), although the reaction of the 4--aryl-4-oxobut-2-enoate bearing a strong electron-donating group, such as PhO–, required a little longer time and gave a relatively lower yield (entries **4** and **9**).

TABLE I. The catalytic conjugate addition of methyl acetoacetate to ethyl 4-phenyl-4-oxobut--2-enoate under different conditions

Entry	Catalyst[a]	Solvent	Yield[b], %
1	Et_3N	THF	40
2	Et_3N	PhH	22
3	Et_3N	CH_3CN	18
4	Et_3N	Et_2O	33
5	Et_3N	CH_2Cl_2	49
6	Et_3N	EtOH	60
7	Pyridine	EtOH	42
8	DABCO	EtOH	16
9	DBU	EtOH	53
10	*t*-BuOK	EtOH	81
11	K_2CO_3	EtOH	88

[a]Catalyst load: 20 mol %; [b]isolated yields, the runs were performed under reflux conditions for 2.5 h

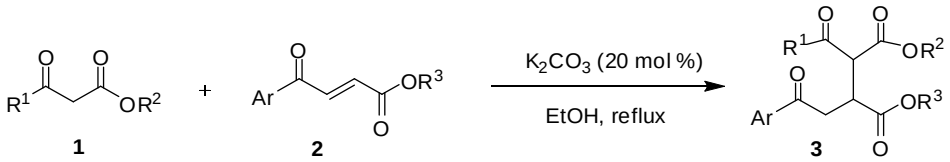

Scheme 2. K_2CO_3 catalyzed Michael addition of 1,3-dicarbonyl compounds to 4-aryl-4-oxobut-2-enoates.

TABLE II. K_2CO_3 catalyzed Michael addition of 1,3-dicarbonyl compounds to 4-aryl-4-oxobut-2-enoates (reaction conditions: β-dicarbonyl compound **1** (1 mmol), 4-aryl-4-oxobut-2--enoate **2** (1 mmol) in EtOH (10 mL) with K_2CO_3 (0.2 mmol, 20 mol %) as catalyst, stirred under reflux)

Entry	R^1	R^2	Ar	R^3	Product	Time, h	Yield[a], %
1	Me	Me	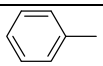	Et	**3a**[b]	2.0	88
2	Me	Et		CH_2Ph	**3b**[b]	2.0	85
3	Me	Et	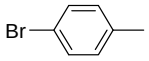	Et	**3c**[b]	2.0	82
4	Me	Et	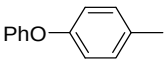	CH_2Ph	**3d**[b]	2.5	77
5	Me	Et	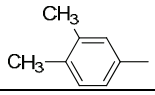	Et	**3e**[b]	2.0	89

TABLE II. Continued

Entry	R^1	R^2	Ar	R^3	Product	Time, h	Yield[a], %
6	OEt	Et	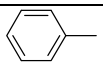	Et	**3f**	2.0	90
7	OEt	Et	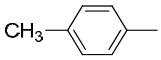	Et	**3g**[b]	2.5	82
8	OEt	Et	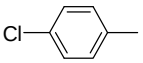	Et	**3h**[b]	2.0	86
9	OEt	Et	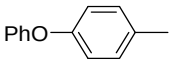	CH_2Ph	**3i**[b]	2.5	81
10	OEt	Et	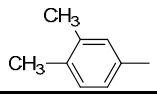	Et	**3j**[b]	2.5	85

[a]Isolated yields; [b]new compound

Using 4-aryl-4-oxobut-2-enoates as the acceptors, it was decided to investigate the addition of other carbon nucleophiles, such as nitroalkanes. Fortunately, it was found that the reactions could also proceed efficiently with K_2CO_3 as the catalyst (Scheme 3, Table III) and that CH_2Cl_2 is a superior solvent for the reactions. Various substituted 4-aryl-4-oxobut-2-enoates and nitroalkanes were employed as the substrates to examine the scope of the addition and the results are summarized in Table III. Both nitromethane and nitroethane reacted successfully with 4-aryl-4-oxobut-2-enoates and gave the corresponding products in good yields at room temperature within 3 h. With regard to the substituents on the aryl moiety in 4-aryl-4-oxobut-2-enoates, their electron properties seem to only slightly affect the efficiency of the reactions.

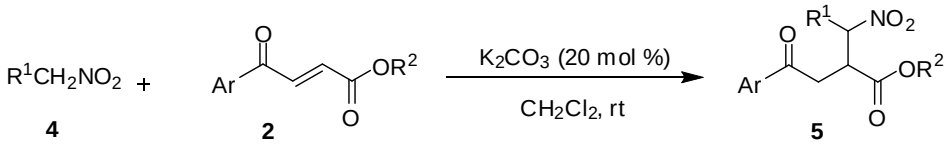

Scheme 3. K_2CO_3 catalyzed Michael addition of nitroalkanes to 4-aryl-4-oxobut-2-enoates.

TABLE III. K_2CO_3 catalyzed Michael addition of nitroalkanes to 4-aryl-4-oxobut-2-enoates (reaction conditions: nitroalkane **4** (1 mmol), 4-aryl-4-oxobut-2-enoate **2** (1 mmol), in CH_2Cl_2 (10 mL) with K_2CO_3 (0.2 mmol, 20 mol %) as catalyst, stirred at room temperature

Entry	R^1	Ar	R^2	Product	Time, h	Yield[a], %
1	H	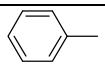	Et	**5a**	3.0	81
2	H	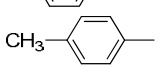	Et	**5b**	3.0	80
3	H	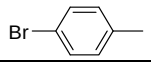	Et	**5c**	2.0	86

TABLE III. Continued

Entry	R^1	Ar	R^2	Product	Time, h	Yield[a], %
4	H	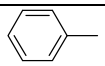	CH_2Ph	**5d**	2.5	85
5	H	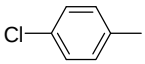	CH_2Ph	**5e**[b]	1.5	87
6	Me		CH_2Ph	**5f**[b]	3.0	82

[a]Isolated yields; [b]new compound

It is noteworthy that the above catalytic conjugate reactions exhibited complete regioselectivity. The carbon nucleophiles selectively attacked the β-position of the ketone carbonyl and no product from the addition on the β-position of the ester carbonyl was observed under the employed catalytic conditions.

Among the results, most of the products, including all adducts (**3a**–**e**) derived from the reactions with β-keto esters, are new compounds.

EXPERIMENTAL

The employed reagents were commercially available and used without further purification unless otherwise indicated. EtOH was treated with magnesium before distillation. 4--Aryl-4-oxobuten-2-oic acid,[27] and the corresponding esters **2** were prepared according to literature procedures.[28] TLC was performed on silica gel plates with F-254 indicator; viewing was by UV light (254 nm). Flash column chromatography was realized over silica gel (200––300 mesh), using ethyl acetate/petroleum ether mixtures as eluents. The ^{1}H- and ^{13}C-NMR spectra were recorded on a Bruker AVANCE 400 MHz spectrometer with $CDCl_3$ as solvent and TMS as the internal standard. The infrared (IR) spectra were recorded on a Nicolet Nexus 670 FT-IR spectrophotometer. The elemental analyses were performed on a Various-ELIII elemental analyzer.

General procedure for the conjugation of β*-dicarbonyl compounds **1** to 4-aryl-4-oxobut-2--enoates **2**. Synthesis of compounds **3***

To a solution of 4-aryl-4-oxobut-2-enoate **2** (1 mmol) and β-dicarbonyl compounds **1** (1 mmol) in anhydrous EtOH (10 mL) was added K_2CO_3 (0.2 mmol, 20 mol %) at room temperature. The mixture was stirred under reflux and monitored by TLC. After the starting material **2** had been completely consumed, the reaction mixture was cooled to room temperature and quenched by HCl (0.03 mol L^{-1}). The solvent was evaporated under vacuum and the residue was extracted with ethyl acetate. The combined organic layers were washed with saturated NaCl. Then, the organic layer was dried over anhydrous $MgSO_4$. After solvent evaporation under vacuum, the residue was purified by flash column chromatography on silica gel to give the desired products **3**.

*General procedure for the conjugation of nitroalkanes **4** to 4-aryl-4-oxobut-2-enoates **2**. Synthesis of compounds **5***

To a solution of 4-aryl-4-oxobut-2-enoate **2** (1 mmol) and nitroalkane **4** (1 mmol) in CH_2Cl_2 (10 mL) was added K_2CO_3 (0.2 mmol, 20 mol %). The mixture was stirred at room temperature and monitored by TLC. After the starting material **2** had been completely consumed, the reaction was quenched by HCl (0.03 mol L^{-1}). The mixture was extracted with ethyl acetate.

The combined organic layers were washed with saturated NaCl and then dried over anhydrous $MgSO_4$. After solvent evaporation under vacuum, the residue was purified by flash column chromatography on silica gel to give the desired products **5**.

CONCLUSIONS

In summary, a facile and efficient conjugate addition of β-dicarbonyl compounds and nitroalkanes to 4-aryl-4-oxobut-2-enoates was achieved. The obtained multi-functionalized adducts might be synthetically or pharmaceutically important. Compared with the reported methods using expensive or unavailable organic catalysts, a common and inexpensive inorganic base (K_2CO_3) was employed as the base catalyst. The presented reaction proceeded with complete regioselectivity and various substituents were tolerated. In addition, the methodology could be successfully applied to reactions with various C-nucleophiles, including β-keto esters. The common catalyst, the ready availability of the materials, the simplicity of the procedure and the potentially valuable adducts make the protocol potentially practical and useful to synthetic chemists.

SUPPLEMENTARY MATERIAL

Spectral data of the products are available electronically at http://www.shd.org.rs/JSCS/, or from the corresponding author on request.

Acknowledgement. This work was financially supported by the National Natural Science Foundation of China (No. 20802070).

И З В О Д

ЈЕДНОСТАВНА И ЕФИКАСНА КОНЈУГОВАНА АДИЦИЈА β-ДИКАРБОНИЛНИХ ЈЕДИЊЕЊА И НИТРОАЛКАНА НА 4-АРИЛ-4-ОКСОБУТ-2-ЕНОАТЕ

XIN LV, YAOHONG ZHANG, LIEJIN ZHOU и XIAOXIA WANG

Zhejiang Key Laboratory for Reactive Chemistry on Solid Surfaces, College of Chemistry and Life Sciences, Zhejiang Normal University, Jinhua 321004, P. R. China

Остварена је једноставна и ефикасна конјугована адиција угљеникових нуклеофила као што су β-дикарбинилна једињења и нитроалкани на 4-арил-4-оксобут-2-еноате, у базно-катализованим реакционим условима. Под примењеним условима могу се добити различити више-функционални γ-кето естри у добром до одличном приносу, уз потпуну региоселективност реакције.

(Примљено 9. септембра 2010, ревидирано 3. јануара 2011)

REFERENCES

1. J. Christoffers, A. Baro, *Angew. Chem. Int. Ed.* **42** (2003) 1688
2. M. P. Sibi, S. Manyem, *Tetrahedron* **56** (2000) 8033
3. P. Perlmutter, *Conjugate Addition Reactions in Organic Synthesis*, Tetrahedron Organic Chemistry Series, Vol. 9, Pergamon Press, Oxford, 1992
4. R. Ballini, G. Bosica, D. Fiorini, A. Palmieri, M. Petrini, *Chem. Rev.* **105** (2005) 933

5. A. Padmaja, G. Sudhakar Reddy, A. Venkata Nagendra Mohan, V. Padmavathi, *Chem. Pharm. Bull.* **56** (2008) 647
6. J. Vabeno, C. U. Nielsen, T. Ingebrigtsen, T. Lejon, B. Steffansen, K. Luthman, *J. Med. Chem.* **47** (2004) 4755
7. H. H. Lu, X. F. Wang, C. J. Yao, J. M. Zhang, H. Wu, W. J. Xiao, *Chem. Commun.* (2009) 4251
8. R. Ballini, A. Palmieri, P. Righi, *Tetrahedron* **63** (2007) 12099
9. R. Ballini, M. Petrini, *Tetrahedron* **60** (2004) 1017
10. R. Ballini, G. Bosica, *Tetrahedron* **51** (1995) 4213
11. G. Rosini, R. Ballini, *Synthesis* (1988) 833
12. J. P. Sonye, K. Koide, *J. Org. Chem.* **71** (2006) 6254
13. K. Onoue, T. Shintou, C. S. Zhang, I. Itoh, *Chem. Lett.* **35** (2006) 22
14. A. R. Karen, J. K. T. Richard, *Chem. Commun.* (2002) 974
15. Y. Y. Kakogawa, S. M. Himeji, S. T. Kobe, United States Patent 5 264 611, 1993
16. C. S. Chien, T. Kawasaki, M. Sakamotom, Y. Tamura, Y. Kita, *Chem. Pharm. Bull.* **33** (1985) 2743
17. M. Bianch, F. Barzaghi, United States Patent 4 500 731, 1985
18. X. Han, *Tetrahedron Lett.* **48** (2007) 2845
19. W. P. Ye, J. Y. Xu, C. T. Tan, C. H. Tan, *Tetrahedron Lett.* **46** (2005) 6875
20. X. X. Wang, Y. H. Zhang, X. H. Xiao, X. S. Li, *Chem. Lett.* **37** (2008) 1284
21. W. P. Ye, D. S. Leow, S. L. M. Goh, C. T. Tan, C. H. Chian, C. H. Tan, *Tetrahedron Lett.* **47** (2006) 1007
22. A. A. Tishkov, V. O. Smirnov, M. V. Nefed'eva, I. M. Lyapkalo, S. E. Semenov, S. L. Ioffe, Y. A. Strelenko, V. A. Tartakovskii, *Russ. J. Org. Chem.* **37** (2001) 416
23. Z. Wang, D. H. Chen, Z. G. Yang, S. Bai, X. H. Liu, L. L. Lin, X. M. Feng, *Chem. Eur. J.* **16** (2010) 10130
24. A. S. Smirnov, S. V. Makarenko, V. M. Berestovitskaya, A. I. Pekki, K. S. Konovalenko, *Russ. J. Org. Chem.* **42** (2006) 1242
25. R. Ballini, G. Bosica, A. Palmieri, K. Bakhtiari, *Synlett* (2009) 268
26. R. Ballini, G. Bosica, S. Gabrielli, A. Palmieri, *Tetrahedron* **65** (2009) 2916
27. M. Bianchi, F. Barzaghi, United States Patent 4 473 583, 1984
28. S. T. Kobe, Y. U. Takasago, Y. Yanagida, T. O. Kobe, K. W. Akashi, United States Patent 4 994 600, 1991.

Journal of the Serbian Chemical Society
JSCS@tmf.bg.ac.rs • www.shd.org.rs/JSCS
J. Serb. Chem. Soc. 76 (7) S1–S5 (2011) *Supplementary material*

SUPPLEMENTARY MATERIAL TO

Facile and efficient conjugate additions of β-dicarbonyl compounds and nitroalkanes to 4-aryl-4-oxobut-2-enoates

XIN LV, YAOHONG ZHANG, LIEJIN ZHOU and XIAOXIA WANG*

Zhejiang Key Laboratory for Reactive Chemistry on Solid Surfaces, College of Chemistry and Life Sciences, Zhejiang Normal University, Jinhua 321004, P. R. China

J. Serb. Chem. Soc. 76 (7) (2011) 947–954

SPECTRAL DATA OF THE PRODUCTS

*4-Ethyl-1-methyl 2-acetyl-3-(2-oxo-2-phenylethyl)succinate (**3a**)*. New compound. Yield: 88 %; oil; Anal. Calcd. for $C_{17}H_{20}O_6$: C, 63.74; H, 6.29 %. Found: C, 63.90; H, 6.26 %. IR (film, cm^{-1}): 3062, 2983, 2956, 1729, 1686, 1598, 1449, 1362, 1257, 1030. MS (*m*/*z*): 320 (M^+). ^{1}H-NMR (400 MHz, $CDCl_3$, δ / ppm), major: 1.18–1.22 (3H, *m*), 2.40 (3H, *s*), 3.41 (1H, *dd*, J_1 = 5.2 Hz, J_2 = 18.0 Hz), 3.53–3.62 (1H, *m*), 3.72 (3H, *s*), 3.83–3.85 (1H, *m*), 4.11–4.18 (2H, *m*), 4.25 (1H, *d*, *J* = 8.0 Hz), 7.49 (2H, *t*, *J* = 8.0 Hz), 7.60 (1H, *t*, *J* = 7.2 Hz), 7.96–7.98 (2H, *m*). ^{13}C-NMR (100 MHz, $CDCl_3$, δ / ppm), major: 13.9, 30.3, 37.5, 39.7, 52.6, 58.6, 61.4, 128.1, 128.7, 133.4, 136.7, 168.6, 172.5, 197.6, 202.3. ^{1}H-NMR (400 MHz, $CDCl_3$, δ / ppm), minor: 1.18–1.22 (3H, *m*), 2.33 (3H, *s*), 3.31 (1H, *dd*, J_1 = 5.2 Hz, J_2 = 18.0 Hz), 3.53–3.62 (1H, *m*), 3.77 (3H, *s*), 3.83–3.85 (1H, *m*), 4.11–4.18 (2H, *m*), 4.25 (1H, *d*, *J* = 8.0 Hz), 7.49 (2H, *t*, *J* = 8.0 Hz), 7.60 (1H, *t*, *J* = 7.2 Hz), 7.96–7.98 (2H, *m*). ^{13}C-NMR (100 MHz, $CDCl_3$, δ / ppm), minor: 13.9, 29.9, 37.4, 39.4, 52.7, 59.4, 61.4, 128.1, 128.7, 133.4, 136.7, 169.1, 172.4, 197.7, 202.2.

*4-Benzyl-1-ethyl 2-acetyl-3-(2-oxo-2-phenylethyl)succinate (**3b**)*. New compound. Yield: 85 %; oil; Anal. Calcd. for $C_{23}H_{24}O_6$: C, 69.68; H, 6.10 %. Found: C, 69.49; H, 6.15 %. IR (film, cm^{-1}): 2925, 1723, 1598, 1450, 1385, 1260, 1085. MS (*m*/*z*): 396 (M^+). ^{1}H-NMR (400 MHz, $CDCl_3$, δ / ppm), major: 1.22–1.32 (3H, *m*), 2.39 (3H, *s*), 3.48 (1H, *dd*, J_1 = 5.2 Hz, J_2 = 18.0 Hz), 3.60–3.74 (1H, *m*), 3.86–3.99 (1H, *m*), 4.16–4.27 (2H, *m*), 4.30 (1H, *d*, *J* = 8.0 Hz), 5.17 (2H, *d*, *J* = 4.0 Hz), 7.32–7.41 (5H, *m*), 7.40–7.54 (2H, *m*), 7.61–7.70 (1H, *m*), 7.98–8.01 (2H, *m*). ^{13}C-NMR (100 MHz, $CDCl_3$, δ / ppm), major: 13.9, 30.3, 37.4, 39.6, 59.4, 61.8, 67.2, 128.1, 128.2, 128.3, 128.5, 128.6, 133.4, 135.4, 168.1, 172.4,

* Corresponding author. E-mail: wangxiaoxia@zjnu.cn

197.6, 202.0. ^{1}H-NMR (400 MHz, $CDCl_3$, δ / ppm), minor: 1.22–1.32 (3H, *m*), 2.32 (3H, *s*), 3.38 (1H, *dd*, J_1 = 5.2 Hz, J_2 = 18.0 Hz), 3.60–3.74 (1H, *m*), 3.86––3.99 (1H, *m*), 4.16–4.27 (2H, *m*), 4.30 (1H, *d*, *J* = 8.0 Hz), 5.17 (2H, *d*, *J* = 4.0 Hz), 7.32–7.41 (5H, *m*), 7.40–7.54 (2H, *m*), 7.61–7.70 (1H, *m*), 7.98–8.01 (2H, *m*). ^{13}C-NMR (100 MHz, $CDCl_3$, δ / ppm), minor: 13.9, 29.9, 37.3, 39.4, 58.7, 61.8, 67.2, 128.1, 128.2, 128.3, 128.5, 128.6, 133.4, 135.4, 168.6, 172.3, 197.6, 202.3.

*Diethyl 2-acetyl-3-(2-(4-bromophenyl)-2-oxoethyl)succinate (**3c**)*. New compound. Yield: 82 %; oil; Anal. Calcd. for $C_{18}H_{21}BrO_6$: C, 52.31; H, 5.12 %. Found: C, 52.43; H, 5.10 %. IR (film, cm^{-1}): 3093, 2960, 1727, 1687, 1586, 1465, 1399, 1255, 1071. MS (*m*/*z*): 412 (^{79}Br, M^+), 414 (^{81}Br, M^+). ^{1}H-NMR (400 MHz, $CDCl_3$, δ / ppm), major: 1.21–1.29 (3H, *m*), 1.42–1.44 (3H, *m*), 2.37 (3H, *s*), 3.33 (1H, *dd*, J_1 = 5.2 Hz, J_2 = 18.0 Hz), 3.50 (1H, *dd*, J_1 = 6.0 Hz, J_2 = = 18.0 Hz), 3.75–3.90 (1H, *m*), 4.06–4.21 (5H, *m*), 7.60–7.62 (2H, *m*), 7.80–7.83 (2H, *m*). ^{13}C NMR (100 MHz, $CDCl_3$, δ / ppm), major: 14.0, 30.3, 37.0, 39.6, 58.7, 59.4, 61.8, 64.1, 128.6, 129.6, 132.0, 135.1, 168.1, 172.5, 196.6, 201.7. ^{1}H--NMR (400 MHz, $CDCl_3$, δ / ppm), minor: 1.21–1.29 (3H, *m*), 1.52–1.54 (3H, *m*), 2.30 (3H, *s*), 3.22 (1H, *dd*, J_1 = 5.2 Hz, J_2 = 18.0 Hz), 3.59 (1H, *dd*, J_1 = 6.0 Hz, J_2 = 18.0 Hz), 3.75–3.90 (1H, *m*), 4.06–4.21 (5H, *m*), 7.60–7.62 (2H, *m*), 7.80–7.83 (2H, *m*). ^{13}C-NMR (100 MHz, $CDCl_3$, δ / ppm), minor: 14.0, 29.9, 37.3, 39.4, 58.7, 59.4, 61.9, 64.1, 128.6, 129.6, 132.0, 135.1, 168.5, 172.3, 196.7, 202.0.

*4-Benzyl-1-ethyl 2-acetyl-3-(2-oxo-2-(4-phenoxyphenyl)ethyl)succinate (**3d**)*. New compound. Yield: 77 %; oil; Anal. Calcd. for $C_{29}H_{28}O_7$: C, 71.30; H, 5.78 %. Found: C, 71.15; H, 5.81 %. IR (film, cm^{-1}): 3066, 2982, 2931, 1731, 1679, 1679, 1584, 1488, 1245, 1023. MS (*m*/*z*): 488 (M^+). ^{1}H-NMR (400 MHz, $CDCl_3$, δ / ppm), major: 1.14–1.21 (3H, *m*), 2.30 (3H, *s*), 3.33 (1H, *dd*, J_1 = 5.2 Hz, J_2 = = 18.0 Hz), 3.48–3.55 (1H, *m*), 3.88–3.91 (1H, *m*), 4.07–4.16 (2H, *m*), 4.23 (1H, *d*, *J* = 8.0 Hz), 5.08 (2H, *s*), 6.96 (2H, *d*, *J* = 8.0 Hz), 7.04 (2H, *d*, *J* = 8.0 Hz), 7.18 (1H, *t*, *J* = 7.4 Hz), 7.27–7.35 (5H, *m*), 7.37 (2H, *t*, *J* = 7.8 Hz), 7.89 (2H, *d*, *J* = 8.8 Hz). ^{13}C-NMR (100 MHz, $CDCl_3$, δ / ppm), major: 14.0, 30.3, 37.2, 39.7, 58.8, 61.7, 67.2, 117.3, 120.2, 124.7, 128.3, 128.5, 130.1, 130.4, 130.5, 135.4, 150.6, 162.2, 168.1, 172.5, 196.1, 201.7. ^{1}H-NMR (400 MHz, $CDCl_3$, δ / ppm), minor: 1.14–1.21 (3H, *m*), 2.18 (3H, *s*), 3.23 (1H, *dd*, J_1 = 5.2 Hz, J_2 = 18.0 Hz), 3.48–3.55 (1H, *m*), 3.88–3.91 (1H, *m*), 4.07–4.16 (2H, *m*), 4.23 (1H, *d*, *J* = 8.0 Hz), 5.09 (2H, *s*), 6.96 (2H, *d*, *J* = 8.0 Hz), 7.04 (2H, *d*, *J* = 8.0 Hz), 7.18 (1H, *t*, *J* = 7.4 Hz), 7.27–7.35 (5H, *m*), 7.37 (2H, *t*, *J* = 7.8 Hz), 7.89 (2H, *d*, *J* = 8.8 Hz). ^{13}C-NMR (100 MHz, $CDCl_3$, δ / ppm), minor: 14.0, 29.9, 37.2, 39.5, 59.5, 61.8, 67.2, 117.3, 120.2, 124.7, 128.3, 128.5, 130.1, 130.4, 130.5, 135.4, 150.6, 162.2, 168.6, 172.5, 196.1, 202.0.

*Diethyl 2-acetyl-3-(2-(3,4-dimethylphenyl)-2-oxoethyl)succinate (**3e**)*. New compound. Yield: 89 %; oil; Anal. Calcd. for $C_{20}H_{26}O_6$: C, 66.28; H, 7.23 %. Found: C, 66.13; H, 7.25 %. IR (film, cm^{-1}): 2981, 2927, 1733, 1681, 1608, 1573, 1450, 1257, 1028. MS (*m/z*): 362 (M^+). ^{1}H-NMR (400 MHz, $CDCl_3$, δ / / ppm), major: 1.18–1.30 (6H, *m*), 2.33 (6H, *s*), 2.39 (3H, *s*), 3.38 (1H, *dd*, J_1 = = 5.2 Hz, J_2 = 18.0 Hz), 3.54 (1H, *dd*, J_1 = 5.6 Hz, J_2 = 18.0 Hz), 3.75–3.90 (1H, *m*), 4.18–4.24 (5H, *m*), 7.23 (1H, *d*, J = 8.0 Hz), 7.69–7.74 (2H, *m*). ^{13}C-NMR (100 MHz, $CDCl_3$, δ / ppm), major: 14.0, 20.1, 30.3, 37.3, 39.7, 58.8, 61.3, 61.8, 125.8, 129.2, 129.9, 134.3, 137.0, 143.0, 168.2, 172.7, 197.5, 202.3. ^{1}H-NMR (400 MHz, $CDCl_3$, δ / ppm), minor: 1.18–1.30 (6H, *m*), 2.33 (6H, *s*), 2.39 (3H, *s*), 3.28 (1H, *dd*, J_1 = 5.2 Hz, J_2 = 18.0 Hz), 3.59 (1H, *dd*, J_1 = 5.6 Hz, J_2 = 18.0 Hz), 3.75–3.90 (1H, *m*), 4.18–4.24 (5H, *m*), 7.23 (1H, *d*, J = 8.0 Hz), 7.69–7.74 (2H, *m*). ^{13}C-NMR (100 MHz, $CDCl_3$, δ / ppm), minor: 14.0, 19.8, 29.9, 37.4, 39.4, 59.7, 61.3, 61.8, 125.8, 129.2, 129.9, 134.3, 137.0, 143.0, 168.0, 172.6, 197.5, 201.9.

*Triethyl 4-oxo-4-phenylbutane-1,1,2-tricarboxylate (**3f**)*.[1] Yield: 90 %; oil. IR (film, cm^{-1}): 2983, 2930, 1732, 1688, 1597, 1449, 1370, 1261, 1031. ^{1}H--NMR (400 MHz, $CDCl_3$, δ / ppm): 1.06–1.16 (9H, *m*), 3.19–3.32 (1H, *m*), 3.47––3.60 (1H, *m*), 3.68–3.71 (1H, *m*), 3.90 (1H, *d*, J = 6.6 Hz), 4.03–4.11 (6H, *m*), 7.32–7.45 (3H, *m*), 7.83–7.86 (2H, *m*). ^{13}C-NMR (100 MHz, $CDCl_3$, δ / ppm): 13.83, 13.85, 37.3, 39.5, 52.2, 61.13, 61.15, 61.56, 61.58, 127.9, 128.5, 133.2, 136.4, 167.8, 167.9, 171.9, 197.0.

*Triethyl 4-oxo-4-*p*-tolylbutane-1,1,2-tricarboxylate (**3g**)*. New compound. Yield: 82 %; oil; Anal. Calcd for $C_{20}H_{26}O_7$: C, 63.48; H, 6.93 %. Found: C, 63.24; H, 6.96 %. IR (film, cm^{-1}): 2983, 2936, 1733, 1683, 1607, 1558, 1369, 1228, 1097. MS (*m/z*): 378 (M^+). ^{1}H-NMR (400 MHz, $CDCl_3$, δ / ppm): 1.14––1.23 (9H, *m*), 2.36 (3H, *s*), 3.26 (1H, *dd*, J_1 = 4.8 Hz, J_2 = 17.8 Hz), 3.53 (1H, *dd*, J_1 = 7.0 Hz, J_2 = 17.8 Hz), 3.79–3.80 (1H, *m*), 3.95 (1H, *d*, J = 6.6 Hz), 4.09––4.17 (6H, *m*), 7.21 (2H, *d*, J = 8.0 Hz), 7.82 (2H, *d*, J = 8.0 Hz). ^{13}C-NMR (100 MHz, $CDCl_3$, δ / ppm): 13.92, 13.94, 21.6, 37.2, 39.6, 52.4, 61.2, 61.6, 61.7, 128.2, 129.2, 134.0, 144.1, 168.00, 168.02, 172.1, 196.7.

*Triethyl 4-(4-chlorophenyl)-4-oxobutane-1,1,2-tricarboxylate (**3h**)*. New compound. Yield: 86 %; oil; Anal. Calcd. for $C_{19}H_{23}ClO_7$: C, 57.22; H, 5.81 %. Found: C, 57.01; H, 5.76 %. IR (film, cm^{-1}): 2983, 2937, 1732, 1689, 1590, 1466, 1370, 1221, 1093. MS (*m/z*): 398 (^{35}Cl, M^+), 400 (^{37}Cl, M^+). ^{1}H-NMR (400 MHz, $CDCl_3$, δ / ppm): 1.23–1.33 (9H, *m*), 3.32 (1H, *dd*, J_1 = 4.8 Hz, J_2 = = 17.8 Hz), 3.35–3.68 (1H, *dd*, J_1 = 7.4 Hz, J_2 = 17.8 Hz), 3.85–3.94 (1H, *m*), 4.05 (1H, *d*, J = 6.4 Hz), 4.18–4.26 (6H, *m*), 7.49 (2H, *d*, J = 8.4 Hz), 7.96 (2H, *d*, J = 8.4 Hz). ^{13}C-NMR (100 MHz, $CDCl_3$, δ / ppm): 13.96, 13.98, 37.3, 39.5, 52.2, 61.4, 61.78, 61.81, 128.9, 129.5, 134.8, 139.7, 168.0, 172.0, 196.1.

*2-Benzyl-1,1-diethyl 4-oxo-4-(4-phenoxyphenyl)butane-1,1,2-tricarboxylate (**3i**)*. New compound. Yield: 81 %; oil; Anal. Calcd. for $C_{30}H_{30}O_8$: C, 69.49; H, 5.83 %. Found: C, 69.33; H, 5.85 %. IR (film, cm^{-1}): 3066, 2982, 2936, 1731, 1681, 1584, 1489, 1369, 1245, 1030. MS (*m*/*z*): 518 (M^+). ^{1}H-NMR (400 MHz, $CDCl_3$, δ / ppm): 1.22–1.26 (6H, *m*), 3.31 (1H, *dd*, J_1 = 4.8, J_2 = 18.0 Hz), 3.61 (1H, *dd*, J_1= 6.8, J_2 = 18.0 Hz), 3.93 (1H, *m*), 4.03–4.17 (5H, *m*), 5.11 (2H, *d*, *J* = = 4.0 Hz), 6.95 (2H, *d*, *J* = 8.8 Hz), 7.03 (2H, *d*, *J* = 8.0 Hz), 7.16 (1H, *t*, *J* = 7.6 Hz), 7.25–7.28 (5H, *m*), 7.36 (2H, *t*, *J* = 7.6 Hz), 7.91 (2H, *d*, *J* = 8.8 Hz). ^{13}C--NMR (100 MHz, $CDCl_3$, δ / ppm): 13.91, 13.95, 37.2, 39.7, 52.3, 61.70, 61.73, 67.1, 117.3, 120.2, 124.7, 128.2, 128.3, 128.4, 130.1, 130.4, 131.1, 135.5, 155.4, 162.1, 167.9, 168.0, 172.0, 195.6.

*Triethyl 4-(3,4-dimethylphenyl)-4-oxobutane-1,1,2-tricarboxylate (**3j**)*. New compound. Yield: 85 %; oil; Anal. Calcd. for $C_{21}H_{28}O_7$: C, 64.27; H, 7.19 %. Found: C, 64.43; H, 7.16 %. IR (film, cm^{-1}): 2982, 2935, 1725, 1679, 1608, 1573, 1409, 1261, 1034. MS (*m*/*z*): 392 (M^+). ^{1}H-NMR (400 MHz, $CDCl_3$, δ / / ppm): 1.19–1.28 (9H, *m*), 2.31 (6H, *s*), 3.31 (1H, *dd*, J_1 = 4.8, J_2 = 17.8 Hz), 3.59 (1H, *dd*, J_1 = 7.0, J_2 = 17.8 Hz), 3.83–3.84 (1H, *m*), 3.99 (1H, *d*, *J* = 6.4 Hz), 4.14–4.21 (6H, *m*), 7.21 (1H, *d*, *J* = 8.0 Hz), 7.69–7.73 (2H, *m*). ^{13}C-NMR (100 MHz, $CDCl_3$, δ / ppm): 13.95, 13.96, 19.7, 20.0, 30.3, 37.3, 39.6, 52.4, 61.3, 61.68, 61.70, 125.8, 129.2, 129.8, 134.4, 136.9, 142.8, 168.06, 168.08, 172.2, 197.0.

*Ethyl 2-(nitromethyl)-4-oxo-4-phenylbutanoate (**5a**)*.[2] Yield: 81 %; oil. IR (film, cm^{-1}): 3063, 2982, 2925, 1732, 1685, 1556, 1379. ^{1}H-NMR (400 MHz, CDCl, δ / ppm): 1.24 (3H, *t*, *J* = 6.4 Hz), 3.37 (1H, *dd*, J_1 = 6.8 Hz, J_2 = 18.4 Hz), 3.60 (1H, *dd*, J_1 = 5.2 Hz, J_2 = 18.4 Hz), 3.76–3.81 (1H, *m*), 4.18–4.24 (2H, *m*), 4.77 (1H, *dd*, J_1 = 5.6 Hz, J_2 = 14.4 Hz), 4.86 (1H, *dd*, J_1 = 6.0 Hz, J_2 = 14.4 Hz), 7.46–7.50 (2H, *m*), 7.58–7.60 (1H, *m*), 7.94–7.96 (2H, *m*). ^{13}C-NMR (100 MHz, $CDCl_3$, δ / ppm): 14.0, 37.0, 38.4, 61.9, 74.8, 128.1, 128.8, 133.8, 135.9, 170.9, 196.5.

*Ethyl 2-(nitromethyl)-4-oxo-4-*p*-tolylbutanoate (**5b**)*.[2] Yield: 80 %; oil. IR (film, cm^{-1}): 2983, 2925, 1734, 1682, 1557, 1379. ^{1}H-NMR (400 MHz, $CDCl_3$, δ / ppm): 1.24 (3H, *t*, *J* = 7.2 Hz), 2.41 (3H, *s*), 3.34 (1H, *dd*, J_1 = 7.2 Hz, J_2 = = 18.4 Hz), 3.56 (1H, *dd* , J_1 = 5.2 Hz, J_2 = 18.4 Hz), 3.73–3.75 (1H, *m*), 4.17– –4.23 (2H, *m*), 4.75 (1H, *dd*, J_1 = 5.2 Hz, J_2 = 14.4 Hz), 4.85 (1H, *dd*, J_1 = 6.4 Hz, J_2 = 14.4 Hz), 7.26–7.28 (2H, *m*), 7.83–7.86 (2H, *m*). ^{13}C-NMR (100 MHz, $CDCl_3$, δ / ppm): 14.0, 21.7, 36.9, 38.4, 61.8, 74.8, 128.2, 129.4, 133.5, 144.7, 171.0, 196.1.

*Ethyl 4-(4-bromophenyl)-2-(nitromethyl)-4-oxobutanoate (**5c**)*.[2] Yield: 86 %; oil. IR (film, cm^{-1}): 2982, 2925, 1731, 1685, 1556, 1380. ^{1}H-NMR (400 MHz, $CDCl_3$, δ / ppm): 1.23–1.27 (3H, *m*), 3.33 (1H, *dd*, J_1 = 6.8 Hz, J_2 = 18.4 Hz), 3.58 (1H, *dd*, J_1 = 5.2 Hz, J_2 = 18.4 Hz), 3.73–3.76 (1H, *m*), 4.18–4.24 (2H, *m*),

4.79 (1H, *dd*, J_1 = 5.2 Hz, J_2 = 14.4 Hz), 4.85 (1H, *dd*, J_1 = 6.0 Hz, J_2 = 14.4 Hz), 7.60–7.63 (2H, *m*), 7.80–7.83 (2H, *m*). ^{13}C-NMR (100 MHz, $CDCl_3$, δ / ppm): 14.0, 37.0, 38.3, 61.9, 74.8, 129.0, 129.6, 132.1, 134.7, 170.7, 195.6.

*Benzyl 2-(nitromethyl)-4-oxo-4-phenylbutanoate (**5d**)*.[2] Yield: 85 %; oil. IR (film, cm^{-1}): 3064, 3033, 2923, 1734, 1684, 1554, 1380. ^{1}H-NMR (400 MHz, $CDCl_3$, δ / ppm): 3.40 (1H, *dd*, J_1 = 6.8 Hz, J_2 = 18.4 Hz), 3.62 (1H, *dd*, J_1 = 5.2 Hz, J_2 = 18.4 Hz), 3.80–3.85 (1H, *m*), 4.83 (1H, *dd*, J_1 = 5.2 Hz, J_2 = 14.4 Hz), 4.88 (1H, *dd*, J_1 = 6.0 Hz, J_2 = 14.4 Hz), 5.19 (2H, *s*), 7.29–7.36 (5H, *m*), 7.48 (2H, *t*, *J* = 7.6 Hz), 7.61 (1H, *t*, *J* = 7.2 Hz), 7.94 (2H, *d*, *J* = 7.6 Hz). ^{13}C-NMR (100 MHz, $CDCl_3$, δ / ppm): 37.0, 38.4, 67.6, 74.7, 128.1, 128.3, 128.5, 128.7, 128.8, 133.9, 135.1, 135.9, 170.8, 196.4.

*Benzyl 4-(4-chlorophenyl)-2-(nitromethyl)-4-oxobutanoate (**5e**)*. New compound. Yield: 87 %; oil; Anal. Calcd. for : $C_{18}H_{16}ClNO_5$: C, 59.76; H, 4.46; N, 3.87 %. Found: C, 59.60; H, 4.49; N, 3.79 %. IR (film, cm^{-1}): 3034, 2923, 1736, 1686, 1555, 1380. MS (*m*/*z*): 361 (^{35}Cl, M^+), 363 (^{37}Cl, M^+). ^{1}H-NMR (400 MHz, $CDCl_3$, δ / ppm): 3.35 (1H, *dd*, J_1 = 6.4 Hz, J_2 = 18.4 Hz), 3.60 (1H, *dd*, J_1 = 5.2 Hz, J_2 = 18.4 Hz), 3.83 (1H, *t*, *J* = 5.8 Hz), 4.82 (1H, *dd*, *J* = 5.2, 14.4 Hz), 4.90 (1H, *dd*, J_1 = 6.0 Hz, J_2 = 14.4 Hz), 5.20 (2H, *s*), 7.31–7.38 (5H, *m*), 7.45 (2H, *d*, *J* = 8.4 Hz), 7.88 (2H, *d*, *J* = 8.4 Hz). ^{13}C-NMR (100 MHz, $CDCl_3$, δ / / ppm): 37.0 , 38.4, 67.7, 74.7, 128.3, 128.6, 128.7, 129.1, 129.5, 134.2, 135.0, 140.3, 170.6, 195.3.

*Benzyl 2-(1-nitroethyl)-4-oxo-4-phenylbutanoate (**5f**)*. New compound. Yield: 82 %; oil; Anal. Calcd. for $C_{19}H_{19}NO_5$: C, 66.85; H, 5.61; N, 4.10 %. Found: C, 66.70; H, 5.64; N, 4.06 %. IR (film, cm^{-1}): 3064, 2980, 2921, 1728, 1683, 1585, 1553, 1398, 1263, 1071. MS (*m*/*z*): 341 (M^+). ^{1}H-NMR (400 MHz, $CDCl_3$, δ / / ppm), major: 1.55 (3H, *d*, *J* = 6.8 Hz), 3.02–3.07 (1H, *m*), 3.54–3.72 (2H, *m*), 5.01–5.05 (1H, *m*), 5.11–5.19 (2H, *m*), 7.29–7.34 (5H, *m*), 7.45 (2H, *t*, *J* = 7.6 Hz), 7.57 (1H, *t*, *J* = 7.2 Hz), 7.92 (2H, *d*, *J* = 8.0 Hz). ^{13}C-NMR (100 MHz, $CDCl_3$, δ / ppm), major: 16.9, 36.0, 44.4, 67.6, 82.7, 128.1, 128.2, 128.4, 128.6, 128.8, 133.7, 135.1, 136.0, 170.7, 196.5. ^{1}H-NMR (400 MHz, $CDCl_3$, δ / ppm), minor: 1.55 (3H, *d*, *J* = 6.8 Hz), 3.23–3.28 (1H, *m*), 3.54–3.72 (2H, *m*), 5.01–5.05 (1H, *m*), 5.11–5.19 (2H, *m*), 7.29–7.34 (5H, *m*), 7.45 (2H, *t*, *J* = 7.6 Hz), 7.57 (1H, *t*, *J* = 7.2 Hz), 7.92 (2H, *d*, *J* = 8.0 Hz). ^{13}C-NMR (100 MHz, $CDCl_3$, δ / / ppm), minor: 16.5, 36.0, 43.8, 67.5, 82.2, 128.1, 128.2, 128.3, 128.5, 128.7, 133.7, 135.1, 136.0, 170.6, 196.5.

REFERENCES

1. Z. Wang, D. H. Chen, Z. G. Yang, S. Bai, X. H. Liu, L. L. Lin, X. M. Feng, *Chem. Eur. J.* **16** (2010) 10130
2. H. H. Lu, X. F. Wang, C. J. Yao, J. M. Zhang, H. Wu, W. J. Xiao, *Chem. Commun.* (2009) 4251.

Journal of the Serbian Chemical Society
JSCS-info@shd.org.rs • www.shd.org.rs/JSCS
J. Serb. Chem. Soc. 76 (7) 955–963 (2011)
JSCS–4174
UDC 547.367+547.279.3+54–328+546.215:544.478
Original scientific paper

$H_5PV_2Mo_{10}O_{40}$ as an efficient catalyst for the oxidation of thiols to the corresponding disulfides using hydrogen peroxide as the oxidant

ABDOLLAH FALLAH SHOJAEI[1]*, MOHAMAD ALI REZVANI[1] and MAJID HERAVI[2]

[1]*Department of Chemistry, Faculty of Science, University of Guilan, Rasht, 419961-3769 and* [2]*Department of Chemistry, School of Science, Alzzahra University, Vanak, Tehran, Iran*

(Received 4 September 2010, revised 10 January 2011)

Abstract: The $H_5PV_2Mo_{10}O_{40}$ catalyzed the oxidation of thiols to their homodisulfides using hydrogen peroxide as the oxidant under mild conditions is reported. This system provides an efficient, convenient and practical method for the syntheses of symmetrical disulfides. In this work, comparisons of Keggin and Dawson type polyoxometalates are addressed in term of relative stability, hardness and acidity.

Keywords: heteropolyacids; thiols; disulfides; hydrogen peroxide; Keggin type; polyoxometalate; Dawson.

INTRODUCTION

Disulfides play an important role in synthetic organic chemistry[1–3] as well as in biology, notably to control cellular redox potentials in biological systems in which thiols are oxidized to prevent oxidative damage.[4] The disulfide functionality is used as a protecting group under oxidative conditions for thiols, which can be regenerated by S–S bond cleavage.[5] Disulfides have also found industrial applications as vulcanizing agents and as important synthetic intermediates in organic synthesis.[6,7] Thiols can also be over-oxidized to sulfoxides and sulfones; therefore, controlled and selective studies were performed in the present investigation regarding the oxidation of thiols.[8] Various reagents and oxidants have been employed for the oxidation of thiols to homodisulfides.[9–16] Some of these methods suffer from obvious disadvantages, such as long reaction times, limited availability of the oxidant, toxicity of reagents and difficulty in the isolation of the products. Consequently, the introduction of readily available, safe and stable reagents for the oxidation of thiols to disulfide is still a necessity. In continuation of on-going research on the synthetic application of heteropolyacids (HPAs) in

* Corresponding author. E-mail: shja47@gmail.com
doi: 10.2298/JSC100904086S

organic synthesis,[17–23] the applicability of various mixed HPAs for the efficient oxidation of thiols to their homodisulfides using hydrogen peroxide as the oxidizing reagent and under mild conditions is reported herein.

The catalytic function of heteropolyacids (HPAs) and related polyoxometalate compounds has attracted great attention, particularly over the last two decades.[16] In this context, heteropolyacids (HPAs) are promising catalysts. A common and important class of these acids and those used in the majority of catalytic applications is the Keggin class of compounds of general formula $H_nXM_{12}O_{40}$ (X = P, Si, As, Ge, B; M = Mo, W).[24] These solid acids are usually insoluble in non-polar solvents but highly soluble in polar ones. They can be used in bulk or supported forms in both homogeneous and heterogeneous systems. Furthermore, these HPAs have several advantages, including high flexibility in modification of the acid strength, ease of handling, environmental compatibility, non-toxicity, and experimental simplicity.[25] Keggin type polyoxoanions have been widely studied as homogeneous and heterogeneous catalyst for the oxidation of organic compounds.[26]

Another catalytically important subclass of Keggin compounds are the mixed vanadium(V)-substituted HPAs of the general formula $H_{3+n}PV_nM_{12n}O_{40}$ (M = = Mo and W; n = 1–6). These compounds exhibit high activity in acid–base type catalytic reactions; hence they are used in many catalytic areas as homogeneous and heterogeneous catalysts. The most well-known of these HPAs is $H_5PV_2Mo_{10}O_{40}$.

Previously reported procedures for the synthesis of large ring disulfides from thiols using dichlorodioxomolybdenum(VI) as a catalyst produced poor to moderate yields.[13] However, a very efficient and simple method for the oxidative coupling of thiols into the disulfides using hydrogen peroxide as an oxidizing reagent catalyzed by mixed vanadium(V)-substituted HPAs under mild conditions is now reported.

EXPERIMENTAL

All reagents and solvents used in this work are available commercially and were used as received, unless otherwise indicated. Previously reported methods were used to purify the thiols.[24] Preparation of the $H_5PV_2Mo_{10}O_{40}$ catalyst and other mixed heteropolyacids and salts were based on a literature procedure with the following modifications.[25] The acids of $[NaP_5W_{30}O_{110}]^{14-}$, $[P_2W_{18}O_{62}]^{6-}$ and $[P_2Mo_{18}O_{62}]^{6-}$ were prepared according to published methods and were identified by infrared spectroscopy.[26–28] All chemicals were purchased from Merck and used without purification. The ^{1}H-NMR spectra were recorded on a FT-NMR Bruker 100 MHz Aspect 3000 with tetramethylsilane as an internal standard and $CDCl_3$ as the solvent. The IR spectra were recorded on a Buck 500 Scientific Spectrometer in KBr pellets.

Preparation of $H_5PV_2Mo_{10}O_4$[25]

Sodium metavanadate (12.2 g, 100 mmol) was dissolved by boiling in 50 mL of water and then mixed with Na_2HPO_4 (3.55 g, 25 mmol in 50 mL of water). After cooling the solution, concentrated sulfuric acid (5 mL, 17 M, 85 mmol) was added, whereby the solution

developed a red color. $Na_2MoO_4 \cdot 2H_2O$ (60.5 g, 250 mmol) dissolved in 100 mL of water was added to the red solution under vigorous stirring, followed by the slow addition of concentrated sulfuric acid (42 mL, 17 M, 714 mmol). The hot solution was allowed to cool to room temperature. The 10-molybdo-2-vanadophosphoric acid was then extracted with 500 mL of diethyl ether. Air was passed through the heteropoly etherate (bottom layer) to free it of ether. The solid residue was dissolved in water, concentrated to first crystal formation, as already described, and then allowed to crystallize further. The large red crystals that formed were filtered, washed with water and air-dried.

Preparation of $H_4PVMo_{11}O_{40}$

Na_2HPO_4 (3.55 g, 25 mmol) was dissolved in 50 mL of water and mixed with sodium metavanadate (3.05 g, 25 mmol) that had been dissolved by boiling in 50 mL of water. The mixture was cooled and acidified to a red color with concentrated sulfuric acid (2.5 mL, 17 M, 42.5 mmol). To this mixture was added a solution of $Na_2MoO_4 \cdot 2H_2O$ (66.5 g, 274.8 mmol) dissolved in 100 mL of water. Finally, 42.5 mL of concentrated sulfuric acid was added slowly with vigorous stirring of the solution. With this addition, the dark red color changed to a lighter red. After cooling the aqueous solution, the heteropoly acid was extracted with 200 mL of diethyl ether. In this extraction, the heteropoly etherate was present as a middle layer; the bottom layer (water) was yellow and probably contained vanadyl species. After separation, a stream of air was passed through the heteropoly etherate layer to free it of ether. The orange solid that remained was dissolved in 50 mL of water, concentrated to the first appearance of crystals in a vacuum desiccator over concentrated sulfuric acid, and then allowed to crystallize further. The orange crystals that formed were filtered, washed with water and air-dried.

General procedure for the oxidation of thiols to disulfides

$H_5PV_2Mo_{10}O_{40}$ (0.5 g, 0.2 mmol) was dissolved in a mixture of 25 mL of ethanol and 5 mL of H_2O. The substrate thiol (4 mmol) and 1.5 mL (13 mmol) of 30 % H_2O_2 were added to the solution. The reaction mixture was stirred at room temperature until thin layer chromatography, TLC, indicated the reaction was complete. After completion of the reaction, the solid product was filtered off and recrystallized, while in the case of liquid disulfides, after completion of the reaction, the excess H_2O_2 was destroyed by 2 mL of 3×10^{-3} M sodium sulfite. The mixture was treated with dichloromethane (2×25 mL). The organic layer was dried by anhydrous $MgSO_4$ and then concentrated to obtain the required product. General reaction for the oxidation of thiols catalyzed by $H_5PV_2Mo_{10}O_{40}$ is shown in Scheme 1.

$$2RSH \xrightarrow[H_2O_2,\ Solvent]{H_5PV_2Mo_{10}O_{40}} RSSR$$

Scheme 1. General reaction for the oxidation of thiols catalyzed by $H_5PV_2Mo_{10}O_{40}$.

Recycling of the catalyst

In order to ascertain whether the catalyst had succumbed to poisoning and lost its catalytic activity during the reaction, the reusability of the catalyst was investigated. For this purpose, after completion of the model reaction (Scheme 1), dichloromethane was added to the solid reaction mixture. All the products were soluble in dichloromethane but the catalyst was not. Thus, the catalyst was separated by simple filtration, washed with dichloromethane and dried at 90 °C for 1 h, and then reused in further reaction with the same substrate.

RESULTS AND DISCUSSION

Effect of the solvent

4-Chlorothiophenol was taken as a model compound and the reaction conditions were optimized by varying the solvent, Table I. In EtOH + H_2O, the reaction was completed within 2 h. The other solvents provided moderate yields with longer reaction times, except CH_3CN and CH_3NO_2, in which the yields were very low even after 5 h (14 %, entry **12** and 18 %, entry **11**, respectively). Notably, in the absence of catalyst, very low yields were obtained (25 %, entry **2** and 21 %, entry **7**).

TABLE I. Results of the oxidation of 4-chlorothiophenol using H_2O_2 as the oxidant and $H_5PV_2Mo_{10}O_{40}$ as the catalyst in different solvents

Entry	Amount of $H_5PV_2Mo_{10}O_{40}$, g	Solvent	Time, h	Temperature, °C	Yield, %[a]
1	0.5	EtOH + H_2O	2	25	97
2	None		5	50	25
3	1.0		2	25	96
4[b]	0.5		2	25	97
5[c]	0.5		2	25	97
6	0.5	MeOH + H_2O	3	25	90
7	None		5	50	21
8	0.5	EtOH	4	25	73
9	0.5	MeOH	2	25	68
10	0.5	H_2O	4	50	45
11	0.5	CH_3NO_2	5	50	18
12	0.5	CH_3CN	5	50	14
13	0.5	CH_2Cl_2	2	50	74
14	0.5	DMF	2	50	63

[a]Isolated yield based on the weight of the pure product obtained; [b]the reaction was performed with the first recycled catalyst; [c]the reaction was performed with the second recycled catalyst

Effect of the catalyst structure

The effect of the structure of the catalyst on the oxidation of 4-chlorothiophenol, as a model compound, in EtOH + H_2O is presented in Table II. The amount of each catalyst was constant throughout the series. In the Keggin-type polyoxometalates series, $H_5PV_2Mo_{10}O_{40}$ showed the highest catalytic activity. In general, the heteropoly salt type catalysts were less efficient than the heteropolyacids. The Keggin-type polyoxometalates led to more effective reactions in comparison with the Wells–Dawson type polyoxometalates. However, $H_6P_2Mo_{18}O_{62}$ was more effective than $H_6P_2W_{18}O_{62}$ in the oxidation of thiols, possibly due to the difference in tungsten and molybdenum reduction potentials. However, the results indicated that the highest yield of disulfide was obtained with $H_5PV_2Mo_{10}O_{40}$ as catalyst (Table II). This behavior was found to be quite general. The high activity of $H_5PV_2Mo_{10}O_{40}$ in comparison of other HPAs (Tab-

le II) confirmed that in addition to H^+, V^{5+} probably play a catalytic role in the reaction.

TABLE II. Oxidation of 4-chlorothiophenol by H_2O_2 in the presence of a variety of heteropolyacids

Entry	Catalyst	Time, h	Temperature, °C	Yield, %[a]
1	$H_5PV_2Mo_{10}O_{40}$	2	25	97
2	$H_4PVMo_{11}O_{40}$	2	25	95
3	$H_6PV_3Mo_9O_{40}$	2	25	96
4	$H_3PMo_{12}O_{40}$	4	45	92
5	$H_3PW_{12}O_{40}$	4	52	90
6	$H_4SiW_{12}O_{40}$	4	50	89
7	$H_{14}[NaP_5W_{30}O_{110}]$	5	70	75
8	$Na_3PMo_{12}O_{40}$	5	80	68
9	$Na_3PW_{12}O_{40}$	5	90	63
10	$(NH_4)_3H[PMo_{11}VO_{40}]$	5	120	56
11	$H_6P_2Mo_{18}O_{62}$	4	90	79
12	$H_6P_2W_{18}O_{62}$	4	90	72
13	None	4	90	28

[a]Isolated product

Effect of the substituent

The effects of various substituents on a range of aromatic thiols on the oxidation yield in EtOH + H_2O were examined using $H_5PV_2Mo_{10}O_{40}$ as the catalyst. The results are given in Table III. Halogens were chosen as electron-withdrawing groups (entries **3**–**5**), while methyl, phenolic hydroxyl and methylthio groups (entries **1**, **6** and **7**, respectively) were chosen as electron-donating substituents. One heteroaromatic thiol, *i.e.*, pyridine-2-thiol, was successfully oxidized in good yield (entry **9**) as well as benzylthiol (entry **8**) as a benzylic aliphatic representative. The yields were generally very good (>75 %) to excellent (>90 %) with no obvious relationship between the aromatic substituent and yield (compare entries **4** with **5** and **2** with **10**). A highlight of the method is the ease by which the product may be isolated *via* simple filtration followed by removal of the solvent.

TABLE III. Oxidation of thiols with different substituents by H_2O_2 with $H_5PV_2Mo_{10}O_{40}$ as catalyst

Entry	Thiol	Disulfide	Time, h	Yield[a,b], %	M.p., °C Found	M.p., °C Lit.[12,14,29]
1	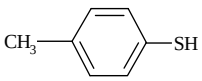	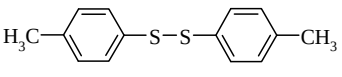	2	97	43–44	44–45

TABLE III. Continued

Entry	Thiol	Disulfide	Time h	Yield[a,b] %	M.p., °C Found	M.p., °C Lit.[12,14,29]
2	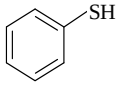	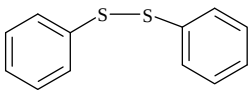	2	96	60–61	61
3	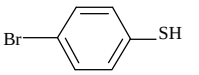	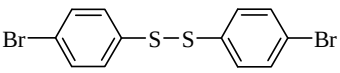	2	95	90–92	91–93
4	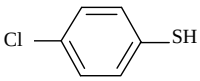	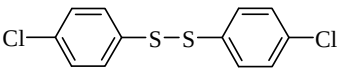	2	97	72–73	70–71
5	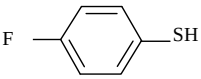	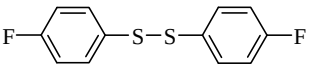	3	79	49–51	–
6	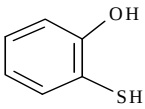	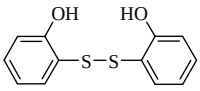	3	89	Liquid[29]	–
7	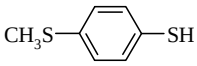	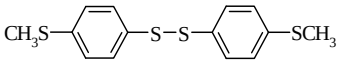	3	82	40–43	40–43
8	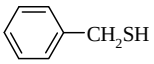	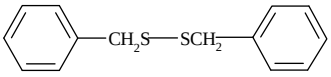	3	78	69–71	69–70
9	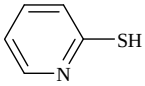	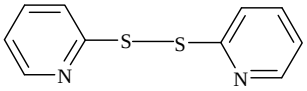	3	77	55–56	55–57
10	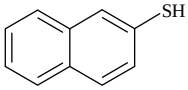	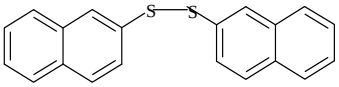	4	78	144–146	142–145

[a]Isolated yield based on the weight of the pure product obtained; [b]The products were identified by comparison of their physical and spectroscopic properties with the respective authentic compound

Reusability of the catalyst

After recovery of the catalyst, it was repeatedly used for further oxidation reactions. Even after five consequent employments, the catalytic activity of $H_5PV_2Mo_{10}O_{40}$ was almost the same as that of fresh catalyst. The results are summarized in Table IV. The IR spectra of the resulting solids indicated that the catalyst can be recovered without structural degradation.

Structures of the obtained disulfides

The structures and purity of the obtained disulfides were verified by ^{1}H- and ^{13}C-NMR spectroscopy and the obtained data are given in Table V, as well as by their melting points that are given in Table III.

TABLE IV. Reuse of the catalyst for oxidation of chlorothiophenol (see Table III, entry **4**, for the reaction conditions)

Entry	Isolated yield, %
1	96
2	94
3	95
4	96
5	92

TABLE V. ^{1}H-NMR and ^{13}C-NMR spectral data of the products

Entry	Product	^{1}H-NMR δ/ ppm	^{13} C-NMR, δ/ ppm
1	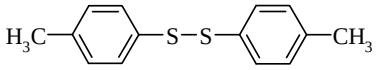	2.42 (6H, *s*, –CH_3), 7.07–7.14 (4H, *m*, Ar), 7.29–7.33 (4H, *m*, Ar)	135.8 (C1, C1′), 134 (C4, C4′), 130 (C3, C5, C3′, C5′), 127 (C2, C6, C2′, C6′), 21 (C7, C7′)
2	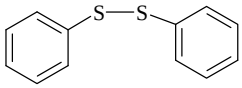	7.11–7.15 (2H, *m*, Ar), 7.29–7.33 (4H, *m*, Ar), 7.44–7.48 (4H, *m*, Ar)	136 (C1, C1′), 129 (C3, C5, C3′, C5′), 126.4 (C4, C4′), 126 (C2, C6, C2′, C6′)
3	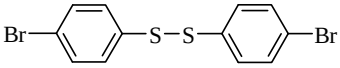	7.11–7.16 (4H, *m*, Ar), 7.34–7.39 (4H, *m*, Ar)	135.8 (C1, C1′), 134 (C4, C4′), 130 (C3, C5, C3′, C5′), 127 (C2, C6, C2′, C6′)
4	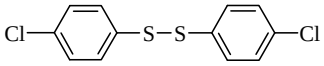	6.57–6.61 (4H, *m*, Ar), 7.21–7.25 (4H, *m*, Ar)	135.3 (C4, C4′), 130 (C2, C6, C2′, C6′), 127 (C3, C5, C3′, C5′), 120 (C1, C1′)
5	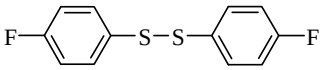	6.37–6.44 (4H, *m*, Ar), 7.33–7.42 (4H, *m*, Ar)	154 (C4, C4′), 132 (C1, C1′), 129 (C2, C6, C2′, C6′), 115 (C3, C5, C3′, C5′)
6	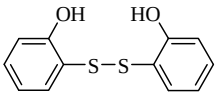	4.50 (2H, *s*, –OH), 6.72–6.76 (2H, *d*, Ar), 6.83–6.88 (2H, *t*, Ar), 7.17–7.22 (2H, *d*, Ar)	155.8 (C2, C2′), 131 (C4, C4′), 127 (C6, C6′), 126 (C1, C1′), 120 (C5, C5′), 113 (C3, C3′)
7	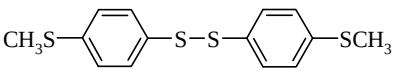	2.40 (6H, *s*, –SCH_3), 6.67–6.73 (4H, *m*, Ar), 7.19–7.23 (4H, *m*, Ar)	136 (C4, C4′), 134 (C1, C1′), 130 (C3, C5, C3′, C5′), 129 (C2, C6, C2′, C6′), 16.4 (C7, C7′)

TABLE V. Continued

Entry	Product	^{1}H-NMR δ/ ppm	^{13}C-NMR, δ/ ppm
8	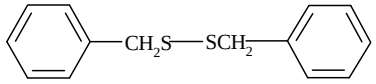	3.53 (4H, *s*, –SCH_2), 7.19–7.22 (2H, *m*, Ar), 7.31–7.35 (4H, *m*, Ar) 7.40–7.45 (4H, *m*, Ar)	137 (C1, C1′), 129 (C2, C2′), 128 (C3, C5, C3′, C5′), 127.4 (C4, C4′), 42.6 (C7, C7′)
9	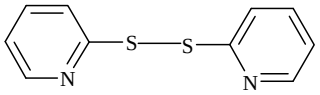	6.89–6.92 (4H, *m*, Py), 7.39–7.41 (2H, *m*, Py), 8.21–8.25 (2H, *m*, Py)	158 (C2, C2′), 147 (C6, C6′), 135 (C4, C4′), 122(C5, C5′), 118(C3, C3′)
10	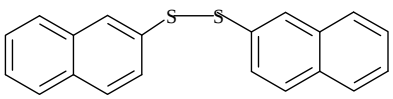	7.40 (2H, *m*, Ar), 7.45 (2H, *m*, Ar), 7.62 (2H, *m*, Ar), 7.70 (2H, *m*, Ar), 7.74 (2H, *m*, Ar), 7.79 (2H, *m*, Ar), 7.96 (2H, *m*, Ar)	138 (C10, C10′), 137 (C8, C8′), 133 (C3, C3′), 134 (C1, C1′), 129.58 (C4, C4′), 128 (C5, C5′), 127 (C9, C9′), 126 (C7, C7′), 125(C2, C2′), 122(C6, C6′)

CONCLUSIONS

The $H_5PV_2Mo_{10}O_{40}$ heteropolyacid was the most successful heteropolyacid in the oxidation of the thiols. Although it is difficult to offer an explanation for the different activity between these HPAs, certainly there is a complex relationship between the activity and structure of the polyanion. By changing the constituent elements of the polyanion (both hetero and addenda atoms), the acid strength of HPAs as well as their catalytic activity are able to vary over a wide range.[18] For the first time, using an inexpensive and easily prepared $H_5V_2PMo_{10}O_{40}$ solid catalyst, the oxidation of thiols with electron-withdrawing and electron-donating groups to the corresponding disulfides was studied. The results showed that the catalyst type is important as well as solvent and temperature, but that the reaction withstands a range of substituents. Furthermore, the reusability of the catalysts was confirmed.

ИЗВОД

$H_5PV_2Mo_{10}O_{40}$ КАО УСПЕШАН КАТАЛИЗАТОР ЗА ОКСИДАЦИЈУ ТИОЛА ДО ОДГОВАРАЈУЋИХ ДИСУЛФИДА ПОМОЋУ ВОДОНИК-ПЕРОКСИДА КАО ОКСИДАЦИОНОГ СРЕДСТВА

ABDOLLAH FALLAH SHOJAEI[1], MOHAMAD ALI REZVANI[1] и MAJID HERAVI[2]

[1]*Department of Chemistry, Faculty of Science, University of Guilan, Rasht 419961-3769 и* [2]*Department of Chemistry, School of Science, Alzzahra University, Vanak, Tehran, Iran*

$H_5PV_2Mo_{10}O_{40}$ катализује оксидацију тиола до одговарајућих дисулфида помоћу водоник-пероксида као оксидационог средства, под благим реакционим условима. Примењени

реакциони услови омогућавају ефикасну и погодну синтезу симетричних дисулфида. У овом раду извршено је поређење са Keggin-овим и Dawson-овим полиоксометалатима у погледу релативне стабилности, јачине и киселости.

(Примљено 4. септембра 2010, ревидирано 10. јануара 2011)

REFERENCES

1. D. C. Jocelyn, *Biochemistry of Thiol Group*, Academic Press, New York, 1992
2. M. C. Carreno, *Chem. Rev*. **95** (1995) 1717
3. N. Iranpoor, B. Zeynizadeh, *Synthesis* **1** (1999) 49
4. J. C. Bardwell, *J. Mol. Microbiol*. **14** (1994) 199
5. A. Ogawa, Y. Nishiyama, N. Kambe, S. Murai, N. Sonoda, *Tetrahedron Lett*. **28** (1987) 3271
6. K. Ramadas, N. Srinivasan, *Synth. Commun*. **25** (1995) 227
7. V. Srivastav, R. Gupta, R. R. Gupta, *Indian J. Chem*. **39B** (2000) 223
8. T. L. Ho, C. M. Wong, *J. Org. Chem*. **39** (1974) 562
9. C. C. Silveira, S. R. Mendes, *Tetrahedron Lett*. **48** (2007) 7469
10. J. Drabowicz, M. Mikolajczyk, *Synthesis* **1** (1980) 32
11. X. Wu, R. D. Rieke, L. Zhu, *Synth. Commun.* **26**(1996)191.
12. A. McKillop, D. Kuyuncu, *Tetrahedron Lett*. **31** (1990) 5007
13. R. Sanz, R. Aguado, M. R. Pedrosa, F. J. Arnaiz, *Synthesis* **7** (2002) 856
14. M. M. Khodaei, I. Mohammadpoor-Baltork, K. Nikoofar, *Bull. Korean Chem. Soc*. **24** (2003) 885
15. V. Kesavan, D. Bonnet-Delpon, J.-P. Begue, *Synthesis* **2** (2000) 223
16. C. A. S. Regino, D. E. Richardson, *Inorg. Chim. Acta* **360** (2007) 3971
17. M. M. Heravi, K. Bakhtiari, F. F. Bamoharram, *Catal. Commun.* **7** (2006) 373
18. F. F. Bamoharram, M. M. Heravi, M. Roshani, A. Gharib, M. Jahangir, *J. Mol. Catal. A: Chem.* **252** (2006) 90
19. M. M. Heravi, R. Motamedi, N. Seifi, F. F. Bamoharram, *J. Mol. Catal. A: Chem.* **249** (2006) 1
20. F. F. Bamoharram, M. M. Heravi, M. Roshani, M. Jahangir, A. Gharib, *J. Appl. Catal. A: Gen.* **302** (2006) 42
21. F. F. Bamoharram, M. M. Heravi, *J. Mol. Catal. A: Chem.* **255** (2006) 193
22. M. M. Heravi, S. Taheri, K. Bakhtiari, *Catal. Commun.*, in press
23. M. M. Heravi, F. K. Behbahani, *J. Mol. Catal. A: Chem.* **253** (2006) 16
24. I. V. Kozhevnikov, Chem. Rev. **98** (1998) 171
25. Y. Izumi, K. Urabe, M. Onaka, *Zeolites Clay and Heteropolyacid in Organic Reactions*, Kodansha, Tokyo, 1992, p. 99
26. I. V. Kozhevnikov, *Chem. Rev*. **98** (1998) 171
27. I. V. Kozhevnikov, *Catalysis for Fine Chemical Synthesis, Catalysis by Polyoxometalates*, Wiley, New York, 2002, p. 2
28. X. López, *PhD Thesis*, Universitat Rovira i Virgili, Tarragona, Spain, 2003
29. H. Golchoubian, F. Hosseinpoor, *Catal. Commun*. **8** (2007) 697.

Journal of the Serbian Chemical Society
JSCS-info@shd.org.rs • www.shd.org.rs/JSCS
J. Serb. Chem. Soc. 76 (7) 965–972 (2011)
JSCS–4175
UDC 66.011+577.152.3+663.1:579.852
Original scientific paper

Optimization of the growth and α-amylase production of *Bacillus subtilis* IP 5832 in shake flask and laboratory fermenter batch cultures

NATAŠA BOŽIĆ[1]*, JORDI RUIZ[2], JOSEP LÓPEZ-SANTÍN[2] and ZORAN VUJČIĆ[3]

[1]*Institute of Chemistry, Technology and Metallurgy-Centre of Chemistry, University of Belgrade, Studentski trg 12–16, Belgrade, Serbia,* [2]*Departament d'Enginyeria Química, Escola d'Enginyeria, Unitat de Biocatàlisi Aplicada associada al IIQA (CSIC), Universitat Autònoma de Barcelona, Edifici Q, 08193-Bellaterra, Spain and* [3]*Faculty of Chemistry, University of Belgrade, Studentski trg 12–16, Belgrade, Serbia*

(Received 25 October, revised 27 December 2010)

Abstract: Cell growth and the level of α-amylase in response to the carbon and nitrogen sources used for the growth of the strain *Bacillus subtilis* IP 5832 were examined. Based on the amylase productivity level in shake flask cultures after 24 hours of growth, the growth medium containing starch and peptone was selected as the best medium. Amylase production was greatly reduced when glutamate or citrate as sources of carbon were used. Experiments performed at different initial concentrations of starch showed that although the strain grew well with all the starch concentration used, 0.5 % starch was necessary for maximum α-amylase production, inducing 1.55 IU mL^{-1} of amylase to be secreted after 8 h of cultivation in shaking flasks. During the batch fermentation of *B. subtilis* IP 5832 strain in 2 L laboratory fermenter, a 60 % higher activity (2.5 IU mL^{-1}) was obtained. The production of the enzyme was directly related to the growth of the strain. Maximum enzyme activity was obtained at the beginning of the stationary growth phase.

Keywords: growth; α-amylase; *Bacillus subtilis*; fermenter; batch cultures.

INTRODUCTION

The production of economically important alpha-amylases is essential for the conversion of starches into oligosaccharides.[1] This enzyme is extensively used in starch liquefaction, and the paper, food, pharmaceutical and sugar industries.[2–4] α-Amylase with suitable properties can be very useful in a specific industry, thus it has become essential to characterize all available microbial strains for their

* Corresponding author. E-mail: nbozic@chem.bg.ac.rs
doi: 10.2298/JSC101010098B

productivity. Since almost all microorganisms of the *Bacillus* genus synthesise α-amylase, this genus has the potential to dominate the enzyme industry.

Bacillus species are heterogeneous forms of organisms and they are very versatile in their adaptability to the environment. Various factors influence the nature of their metabolic process and the enzyme produced. The composition and concentration of media greatly affect the growth and production of extracellular amylase in bacteria.[5] Optimization of cultural conditions is important for maximum production of microbial strains.[6] In this regard, appropriate media components and suitable conditions must be attained for optimal production of the required products. *Bacillus* species and other forms of microorganisms grow at different rates with specificity to different substrates in the culture medium. The growth conditions also influence their enzymatic activities.[7]

Bacillus subtilis IP 5832 has not hitherto been tested for its amylase activity; hence, the present work describes the effects of culture conditions on the growth of the strain and on α-amylase production in batch experiments in shake flasks and under controlled conditions in a laboratory fermenter.

EXPERIMENTAL

Chemicals

All the employed reagents and solvents were of the highest available purity and at least of analytical grade. They were purchased from Merck (Darmstadt, Germany) and Sigma-Aldrich (St. Louis, MO, USA) unless otherwise stated.

Strain and cultivation conditions

Frozen stock aliquots containing glycerol were prepared from exponential phase *Bacillus subtilis* IP 5832 cultures grown in Luria–Bertani media (LB) and stored at –80 °C. Precultures were routinely grown in Luria–Bertani (LB) broth medium composed of (g L^{-1}): peptone, 10.0, yeast extract, 5.0 and NaCl, 10.0. Pre-inoculum cultures were grown from glycerol stocks in 100 mL shake flasks containing 15 mL LB media and incubated overnight at 37 °C in a rotary shaker at 150 rpm. For the shake flasks experiments, 5 mL of pre-inoculum cultures were transferred aseptically to a 500 mL baffled shake flask containing 100 mL of semi-complex growth medium. Unless otherwise stated, the growth medium (BM – basal medium) used for α-amylase production was composed of (g L^{-1}): soluble starch, 5.0; peptone, 20.0; $MgSO_4 \cdot H_2O$, 1.0 and K_2HPO_4, 3.0. The medium was adjusted to pH 7.0. Cultivations were maintained at 37 °C with agitation at 150 rpm for 24 h.

Effect of different semi-synthetic media on growth and α-amylase production

In addition to the described basal medium (BM) for testing the growth and amylase production, the following media, that have been used by others for testing amylase production, were also used: semi-synthetic medium I (SM I) containing (g L^{-1}): tryptone, 2.0; $MgSO_4 \cdot 7H_2O$, 0.05; KH_2PO_4, 1; Na_2HPO_4, 2.5; NaCl, 1; $(NH_4)_2SO_4$, 2 and $CaCl_2 \cdot 2H_2O$, 0.05; semi-synthetic medium II (SM II) containing (g L^{-1}): yeast extract, 20.0; glucose, 5.0; $MgSO_4 \cdot 7H_2O$, 1.0; $FeCl_3$, 0.05; KH_2PO_4, 1; Na_2HPO_4, 2.5; NaCl, 0.5; $(NH_4)_2SO_4$, 7.5; $CaCl_2 \cdot 2H_2O$, 1.0 and thiamine, 0.025, semi-synthetic medium III (SM III) containing (g L^{-1}): starch, 5.0; $MgSO_4 \cdot 7H_2O$, 1.0; $FeCl_3$, 0.05; KH_2PO_4, 1; Na_2HPO_4, 2.5; NaCl, 0.5; $(NH_4)_2SO_4$, 7.5; $CaCl_2 \cdot 2H_2O$, 1.0 and thiamine, 0.025, and Luria–Bertani medium (LB).

Effect of different carbon sources on the growth and α-amylase production

The effect of different carbon sources (0.4 % citrate and 0.4 % glutamate instead of 0.5 % starch) and different levels of starch (0.05–1.0 %) in the basal medium (BM) on amylase production were examined.

Amylase production in a laboratory fermenter

For the bioreactor experiments, 100 mL of pre-inoculum culture (grown in LB medium) were transferred to the bioreactor containing 900 mL of BM growth medium. All growths were performed using a Biostat B bioreactor (Sartorius) equipped with a 2 L fermentation vessel under constant temperature, pH and pO_2 values. The pH was maintained at 7.00±0.05 by adding 30 % H_3PO_4 solution to the reactor. The temperature was kept at 37 °C. The pO_2 value was maintained at 50 % of air saturation by adapting the stirrer speed between 450 and 900 rpm and supplying air (enriched with pure oxygen when necessary, *i.e.*, when the *OD*600 reached 25). The end of the batch phase was identified by a reduction in the oxygen consumption rate and an increase in the acid addition rate. The cultures were centrifuged at 10000 rpm for 20 min at 4 °C using a Beckman J2-21 M/E centrifuge and the cell-free supernatants were used as crude enzyme preparations.

Biomass assay

Growth was followed by optical density measurements at 600 nm (*OD*600). Samples were diluted with deionised water and adjusted to *OD*600 values between 0.2–0.8.

α-Amylase activity assay

The α-amylase activity was determined by measuring the formation of reducing sugars released during starch hydrolysis. The reaction mixture containing 0.05 mL of appropriately diluted enzyme and 0.45 mL of 1.0 % (w/v) soluble starch (Merck) in 50 mM phosphate buffer (pH 6.5) was incubated at 50 °C for 15 min. The amount of liberated reducing sugar was determined by the dinitrosalicylic (DNS) acid method.[8] One unit of amylase activity was defined as the amount of enzyme that released 1 μmol of reducing end groups per min at 50 °C. D-Glucose was used to construct a standard curve.

RESULTS AND DISCUSSION

As the nature and amount of carbon and nitrogen sources in culture media are important for the growth and production of extracellular amylase in bacteria,[9,10] optimization of culture conditions is important for maximum enzyme production by microbial strains. The results of the time-course studies on α-amylase production and cell growth of *B. subtilis* IP 5832 grown in different semi-synthetic media are shown in Fig. 1. The biomass and levels of amylase in the crude culture supernatants varied greatly in response to the carbon and nitrogen source used for the growth of the strain. The maximal growth rate and production of extracellular amylase was obtained when the strain was grown in BM and LB (Fig. 1A). Peptone (BM, LB media) promoted α-amylase productivity. Moreover, the α-amylase biosynthesis appeared to be independent of the availability of starch, since enzyme activity was detected in the culture broth containing tryptone as the single carbon source (SM I). This was also the case with amylase from *B. subtilis.*[11] Nevertheless, the addition of starch to the growth medium in-

creased the level of secreted enzyme. These results are in agreement with previously reported maximum α-amylase production when starch was used as the carbon source.[12,13] Based on the amylase productivity level in the shake flask cultures after 24 h of growth (Fig. 1B), the growth medium containing starch and peptone (BM) was selected as the best medium. Amylase activity during growth of the strain in BM was detected from the early stages of growth (results not shown) and it peaked (1.55 IU mL^{-1}) at 8 h and was found to decline gradually up to 24 h (0.45 IU mL^{-1}). The reason for this might be the simultaneous production of peptidases, which can influence the amylase activity during time. The main advantage of growing *B. subtilis* IP 5832 on BM for amylase production is the very fast production time. Similarly, the production of amylase by *B. thermooleovorans* NP54 peaked at 12 h of growth,[14] while the maximum amylase production by *B. stearothermophilus* AN 002 occurred at 6 h of cultivation.[6] Nevertheless, more often amylase cannot be detected in the culture broth of *Bacillus* sp. before 12 h of incubation.[15–17]

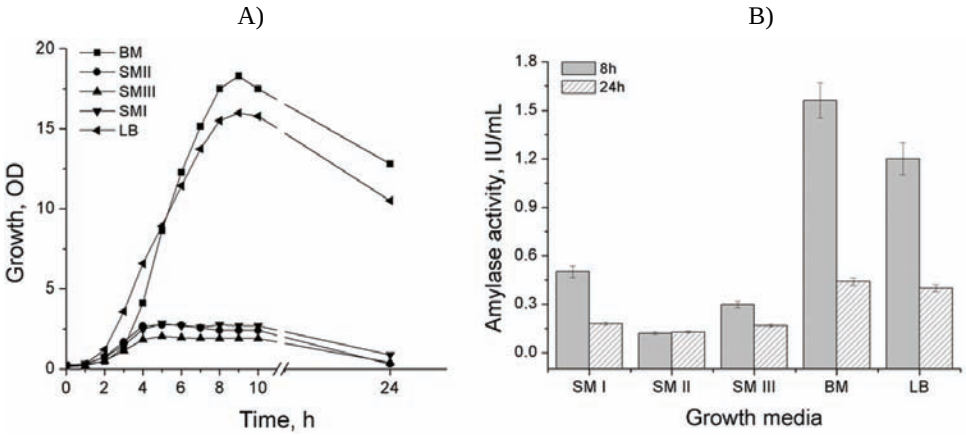

Fig. 1. A) Pattern of growth during 24 h of submerged fermentation of *B. subtilis* IP 5832 at 37 °C in shaking flasks in various growth media. SM I – semi-synthetic medium I; SM II – semi-synthetic medium II; SM III – semi-synthetic medium III; BM – basal medium; LB - Luria–Bertani medium. B) Extracellular α-amylase activity in the time of maximal production (8 h) and at the end of growth (24 h). Each data point represents the mean of three independent assays (the standard errors were less than 5 % of the means).

The synthesis of amylase was greatly suppressed when the bacterium was grown on glucose (Fig. 1, SM II and SM III) or citrate (Fig. 2B), although in the case of citrate, the growth of the bacterium was comparable to the growth on starch (Fig. 2B). The level of growth resulting from the utilization of various carbon sources (Fig. 2A) did not correlate with the amylase activity (Fig. 2B). Amylase production was greatly reduced when glutamate or citrate were used. These results are in agreement with the reports of others who reported maximum amy-

lase production when starch was used as a carbon source.[12,13,18] On the contrary, *B. subtilis* isolated from Turkish soil produced maximum amylase with citrate as the carbon source.[19]

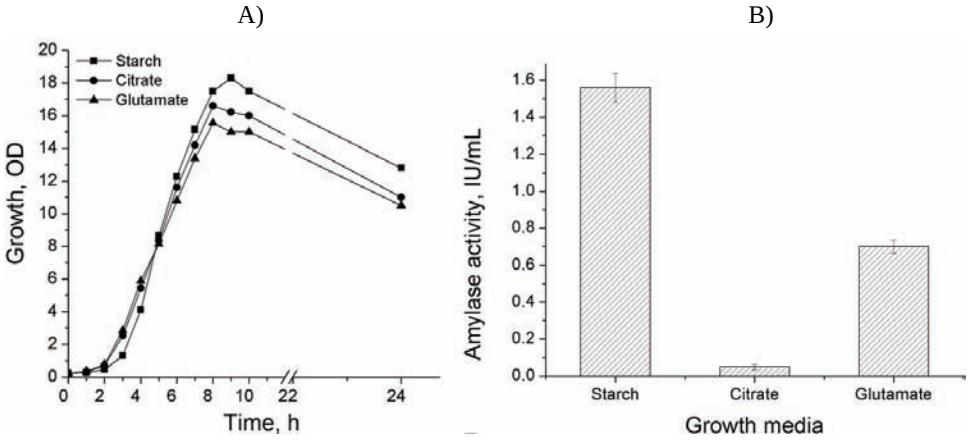

Fig. 2. A) Effect of different carbon sources in BM medium during submerged fermentation of *B. subtilis* IP 5832 at 37 °C in shaking flasks and B) extracellular α-amylase activity at the time of maximal production (8 h). Each data point represents the mean of three independent assays (the standard errors were less than 5 % of the means).

Experiments performed at different initial concentrations of starch showed that although the strain grew well with all the starch concentration used (Fig. 3A), 0.5 % starch was necessary for the maximum α-amylase production, inducing the secretion of 1.55 IU mL^{-1} of amylase after 8 h of cultivation (Fig. 3B). The best enzyme production by *B. licheniformis* CUMC 305 was also obtained with a starch concentration of less than 1 %.[20] Increasing the starch concentration in the medium beyond 0.5 % did not lead to an increase in the enzyme activity. At higher starch concentrations, the enzyme productivity was comparatively low; such a behaviour was also registered for soil isolates *Bacillus* sp.[15] This can be attributed to the high viscosity of the broth at such concentrations, which interferes with O_2 transfer leading to a limitation of dissolved O_2 for bacteria growth.[21]

The results of the time profiles for both α-amylase production and biomass of the *B. subtilis* IP 5832 strain grown in the growth medium in the fermenter are shown in Fig. 4. When the strain was cultivated in a laboratory fermenter, the α-amylase production peaked (2.5 U mL^{-1}) at 8 h. When the *B. subtilis* IP 5832 strain was grown in the laboratory fermenter, the amylase activity was 60 % higher than that obtained when the strain was grown in shake flasks. This was probably the result of the higher shaking speed, constant oxygen supply and constant adjustment of pH during the fermenter culture. As in the shake flasks experiments, the maximum α-amylase production in the fermenter occurred when

optical cell population reached its peak. Amylase production by this strain was found to be growth-associated as the maximum enzyme production was observed during the beginning of stationary phase, when the *OD* reached a plateau. Similar results were obtained for amylase from *Bacillus sp.* IMD 435[22] and amylase from *Bacillus* sp. YX-1.[23]

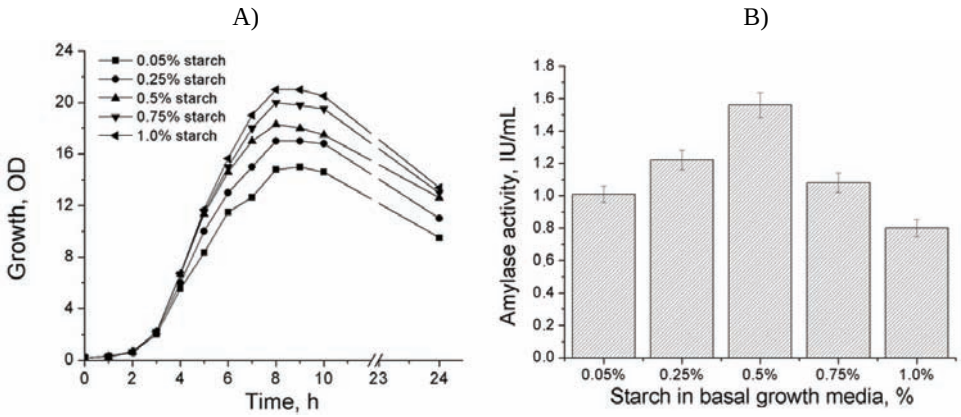

Fig. 3. A) Effect of different starch concentrations in BM medium during submerged fermentation of *B. subtilis* IP 5832 at 37 °C in shaking flasks and B) extracellular α-amylase activity at the time of maximal production (8 h). Each data point represents the mean of three independent assays (the standard errors were less than 5 % of the means).

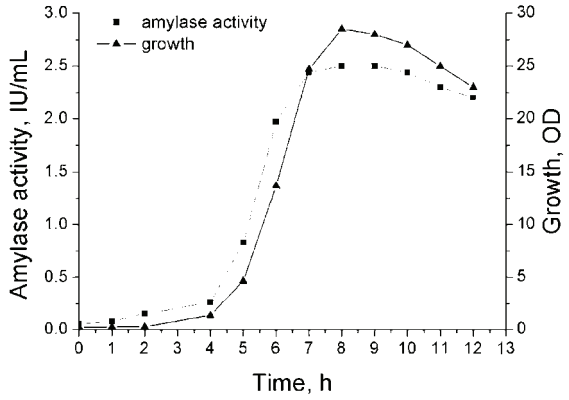

Figure 4. Pattern of growth and extracellular α-amylase production during submerged fermentation of *B. subtilis* IP 5832 in BM medium at 37 °C in a laboratory fermenter. Each data point represents the mean of three independent assays (the standard errors were less than 5 % of the means).

CONCLUSIONS

The optimal N and C sources for growing *B. subtilis* IP 5832 for α-amylase production were found to be 2 % peptone and 0.5 % starch. The maximum α-amylase (1.55 IU mL^{-1}) was produced during batch fermentation in shaking flask after 8 h of growth, while during batch fermentation in 2 L laboratory fermenter, 60 % higher activity (2.5 IU mL^{-1}) was obtained. The production of the enzyme

was directly related to the growth of the strain. Maximum enzyme activity was obtained at the beginning of the stationary growth phase. The proposed process can be considered as a first step in further exploration of possible employment of α-amylase from *B. subtilis* IP 5832 for starch hydrolysis.

Acknowledgements. This work was supported by the Ministry of Education and Science of the Republic of Serbia, project grant number 172048, and by the Spanish MICINN, project number CTQ2008-00578. N. B. acknowledges the Ministry of Education and Science of the Republic of Serbia for a postdoctoral grant. The UAB group constitutes the Research group 2009SGR281 and Biochemical Engineering Unit of the Reference Network in Biotechnology (XRB), Generalitat de Catalunya, Spain.

И З В О Д

ОПТИМИЗАЦИЈА РАСТА И ПРОДУКЦИЈЕ α-АМИЛАЗЕ *Bacillus subtilis* IP 5832 У ШАРЖНИМ КУЛТУРАМА У ЕРЛЕНМАЈЕРУ И ЛАБОРАТОРИЈСКОМ ФЕРМЕНТОРУ

НАТАША БОЖИЋ[1], JORDI RUIZ[2], JOSEP LÓPEZ-SANTÍN[2] и ЗОРАН ВУЈЧИЋ[3]

[1]*Институт за хемију, технологију и металургију – Центар за хемију, Универзитет у Београду, Студентски трг 12–16, Београд,* [2]*Departament d'Enginyeria Química, Escola d'Enginyeria, Unitat de Biocatàlisi Aplicada associada al IIQA (CSIC), Universitat Autònoma de Barcelona, Edifici Q, 08193-Bellaterra, Spain и* [3]*Хемијски факултет, Универзитет у Београду, Студентски трг 12–16, Београд*

Ћелијски раст и нивои α-амилазе након гајења *Bacillus subtilis IP* 5832 испитивани су у зависности од различитих извора угљеника и азота коришћених у подлози. На основу продуктивности амилазе након двадесетчетворочасовног гајења културе у ерленмајерима са мешањем показано је да је најбоља хранљива подлога она која садржи скроб и пептон. Када су глутамат или цитрат коришћени као извори угљеника продукција ензима је била значајно редукована. Експериментима у којима је варирана иницијална концентрација скроба показано је да је, иако сој добро расте на свим коришћеним концентрацијама, 0,5 % скроб неопходан за максималну продукцију ензима, индукујући секрецију 1,55 IU mL^{-1} амилазе након 8 сати гајења културе у ерленмајерима са мешањем. Током шаржне ферментације *B. subtilis IP* 5832 соја у лабораторијском ферментору од 2 L добијено је 60 % више активности ензима (2,5 IU mL^{-1}). Продукција ензима је била директно везана за раст микроорганизма. Максимална ензимска активност добијена је на почетку стационарне фазе раста.

(Примљено 25. октобра, ревидирано 27. децембра 2010)

REFERENCES

1. H. Pederson, J. Nielsen, *Appl. Microbiol. Biotechnol.* **53** (2000) 278
2. P. Nigam, D. Singh, *Enzyme Microb. Technol.* **17** (1995) 770
3. I. Haq, A. Hamad, I. Javed, M. A. Qadeer, *Bioresour. Technol.* **87** (2003) 57
4. I. Roy, M. N. Gupta, *Enzyme Microb. Technol.* **34** (2004) 26
5. R. A. K. Srivastava, J. N. Baruah, *Appl. Environ. Microbiol.* **52** (1986) 179
6. R. L. Bezbaruah, B. K. Gogoi, K. R. Pilla, *J. Basic Microbiol.* **34** (1994) 139
7. A. O. Ajayi, O. E. Fagade, *Afr. J. Biotechnol.* **5** (2006) 440
8. P. Bernfeld, in *Methods in Enzymology*, I. P. De Murray, Ed, Academic Press INC Deutcher, San Diego, CA, USA, 1955, p. 149

9. A. Pandey, P. Nigam, C. R. Soccol, V. T. Soccol, D. Singh, R. Mohan, *Biotechnol. Appl. Biochem.* **31** (2000) 135
10. P. V. Dharani Aiyer, *Afr. J. Biotechnol.* **3** (2004) 519
11. Z. Konsula, M. Liakopoulou-Kyriakides, *Process Biochem.* **39** (2004) 1745
12. L. L. Lin, M. R. Tsau, W. S. Chu, *Appl. Microbiol. Biotechnol.* **42** (1994) 51
13. R. K. Saxena, K. Dutt, L. Agarwal, P. Nayyar, *Bioresour. Technol.* **98** (2007) 260
14. R. Malhotra, S. M. Noorwez, T. Satayanarayana, *Lett. Appl. Microbiol.* **31** (2000) 378
15. E. de O. Santos, M. L. L. Martins, *Braz. Arch. Biol. Technol.* **48** (2003) 129
16. M. Asgher, M. Javaid Asad, S. U. Rahman, R. L. Legge, *J. Food Eng.* **79** (2007) 950
17. N. Goyal, J. K. Gupta, S. K. Soni, *Enzyme Microb. Technol.* **37** (2005) 723
18. T. E. El-Banna, A. A. Abd-Aziz, M. I. Abou-Dobara, R. I. Ibrahim, *Pak. J. Biol. Sci.* **10** (2007) 2039
19. E. Sarikaya, V. Gürgün, *Turk. J. Biol.* **24** (2000) 299
20. T. Krishnan, A. K. Chandra, *Appl. Environ. Microbiol.* **48** (1983) 430
21. R. Rukhaiyar, S. K. Srivastava, *World J. Microbiol. Biotechnol.* **10** (1995) 76
22. L. M. Hamilton, C. T. Kelly, W. M. Fogarty, *Process Biochem.* **35** (1999) 27
23. X. D. Liu, Y. Xu, *Bioresour. Technol.* **99** (2008) 4315.

Journal of the Serbian Chemical Society
JSCS-info@shd.org.rs • www.shd.org.rs/JSCS
J. Serb. Chem. Soc. *76* (7) 973–985 (2011)
JSCS–4176
UDC 547.972:544.032.6–31:615.27:544.4
Original scientific paper

Effects of continuous UV-irradiation on the antioxidant activities of quercetin and rutin in solution in the presence of lecithin as the protective target

DRAGAN CVETKOVIĆ[1], DEJAN MARKOVIĆ[1]*, DRAGANA CVETKOVIĆ[2] and BLAGA RADOVANOVIĆ[3]

[1]Faculty of Technology, 16000 Leskovac, [2]Nevena Color, d.o.o, 16000 Leskovac and [3]Faculty of Science, Department of Chemistry, 18000 Niš, Serbia

(Received 23 November 2010, revised 20 Januaty 2011)

Abstract: The stabilities and antioxidant action of two selected flavonoids, quercetin and rutin, dissolved in methanol and water, toward continuous UV--irradiation from three different sub-ranges (UV-A, UV-B and UV-C) were studied. The flavonoids underwent degradation (bleaching) following first-order kinetics. The bleaching rates were highly dependent on the energy input of the involved UV-photons. The antioxidant activities of the two flavonoids on UV-induced lecithin lipid peroxidation were studied by the thiobarbituric acid–malondialdehyde (TBA–MDA) test, and appeared to be also affected by the continuous UV irradiation. The energy input of the incident UV-photons again played a major governing role, but an impact of the flavonoids structures cannot be neglected.

Key words: flavonoids; UV-irradiation; antioxidant; kinetics.

INTRODUCTION

Sunlight reaching the Earth's surface contains an increasing fraction of its most energetic component, the UV-B fraction, due to the continuing damage of the ozone layer. Plants need sunlight to perform photosynthesis, but the enhanced level of UV-B radiation directly affects photosynthesis,[1] and the related processes, such as leaf morphology and the whole plant growth.[2–5] Both "light" and "dark" phase are affected; the light reaction itself[6,7] includes compositional changes in photosystems II[8] and I.[9] The changes mostly concern structural changes of the photosynthetic pigments,[10,11] especially chlorophyll,[6] but also of other components of the electron-transport chain.[12]

Naturally, plants have developed self-protective mechanisms against damaging UV-light. One of the major plant responses to enhanced UV-B radiation is an in-

* Corresponding author. E-mail: dejan_markovic57@yahoo.com
doi: 10.2298/JSC101123089C

creased synthesis of pigments, capable of UV-B absorption, flavonoids above all. Flavonoids are mainly located in plant leaves but also in the other organs.[13,14] They are excellent UV-absorbers (because of their chemical structure) and hence are plant-protective screen-savers,[15] *i.e.*, they are very effective preventive antioxidants, since they reduce the production of the reactive radical oxygen species (ROS) generated by UV-radiation. However, in the case of free radicals chain reactions, they are also reported to be effective chain-breaking antioxidants.[15–21]

Flavonoids are benzo-γ-pyrone derivatives consisting of phenolic and pyran rings and are classified according to the substitutions in the basic skeleton. Their structures and functions differ in the presence/absence of hydroxyl, methoxy, glycosidic and other groups attached to the A and B rings of the basic skeleton (Fig. 1). In nature, flavonoids exist primarily as 3-*O*-glycosides and polymers.[16] The most important structural elements of flavonoids are: an *o*-dihydroxy group in the B ring (catechol structure) as a radical target; a double bond between positions 2 and 3 of the C-ring conjugated with keto group in position 4, because of its capacity to delocalize the uncoupled electron of a flavonoid radical; C-3,C-5 and C-7 hydroxyl groups (of the C and A rings, respectively) as scavengers of free radicals.[15–20]

The screen-saver function of flavonoids has practical applications, too. As excellent UV-absorbers, flavonoids are used as UV (UV-A and UV-B) protection agents in some cosmetics and pharmaceutical preparations, based on heterogeneous oil–water systems. While the general protective function of flavonoids in the formulations remains unquestionable, the whole picture covering the interactions of these formulations with UV-light, which includes not only flavonoids but also lipids, is less well known. Obviously, lipids undergo oxidation through free radical chain reactions, finishing with the formation of diene-type compounds at the very end, lipid peroxides; the whole process is known as lipid peroxidation.[22,23] Hence, the antioxidant function of flavonoids – toward lipids as the protection target – might be estimated through control of the lipid peroxidation process, partly through absorption of UV-radiation (as the peroxidation initiating agent), and partly through scavenging of the UV-created radical species, including lipid radicals and lipid-peroxy-radicals.[16–18,24]

The main objective of this study was to investigate the interaction of two flavonoids, rutin (flavonol glycoside) and quercetin (flavonol) with prolonged, continuous UV-radiation, in solution, in the absence and in the presence of soybean lecithin (a mixture of lipoidal compounds). The first goal was to obtain basic spectral and kinetic information concerning the stability of the flavonoids against UV-radiation in the absence of lecithin, which is also a measure of the ability of the flavonoids to prevent UV-initiated lecithin (lipid) peroxidation (when lipids are present). However, since prevention (through UV-absorption) is only partial and free radicals are certainly UV-generated in the system, the second goal, in

the presence of lecithin, was to examine the second type of flavonoid antioxidant ability, *i.e.*, to act as chain-breaking antioxidants. This type of approach was employed in previous studies, but with different antioxidants, selected carotenoids.[25,26] The same type of test, the thiobarbituric acid–malondialdehyde (TBA–MDA) test[26] was used to measure the amount of lipid peroxidation and to estimate its control by the flavonoids employed in this work.

EXPERIMENTAL

Samples preparations

Quercetin and rutin standards (Merck) were dissolved in methanol (quercetin and rutin) and in water (rutin), at a concentration of 8×10^{-5} M.

UV–Vis spectroscopy

The UV–Vis spectra of rutin and quercetin in different solvents were recorded on a Varian Cary-100 spectrophotometer. All spectra, before and after irradiation with UV-light, were recorded in the range 200 to 500 nm.

UV-treatment

The irradiation of pigments in different solvents was performed in a cylindrical photochemical reactor "Rayonnet", with 14 symmetrically placed lamps, with emission maxima in three different UV sub-ranges: 254 (UV-C), 300 (UV-B) and 350 nm (UV-A). The samples were irradiated in quartz cuvettes (1 cm×1 cm×4.5 cm) placed on a rotating circular holder. Quercetin was irradiated in methanol, while rutin was irradiated in methanol and water. The concentration of the flavonoids in both solvents was 8×10^{-5} M.

TBA–MDA test

Lecithin peroxidation, as well as its inhibition in the presence of flavonoids, was measured by the TBA–MDA test.[27,28] This method is based on the reaction of malondialdehyde (MDA – a secondary product of lipid peroxidation) with thiobarbituric acid (TBA), whereby a red-coloured complex with a maximum absorption at 532 nm is obtained. The reaction mixture contained 2.2×10^{-3} M aqueous solution of lecithins and 7×10^{-5} M methanolic solution of a flavonoid, in a 10:1 (v/v) ratio. Lecithin peroxidation was initiated by continuous UV-irradiation during increasing times. Two cm^3 of aqueous trichloroacetic acid (5.5 %), and 2.5 cm^3 of Tris-buffer (pH 7.4), followed by 2 cm^3 of thiobarbituric acid (4.2×10^{-2} M in 5×10^{-2} M NaOH) were added in the reaction mixture immediately after irradiation. The mixture was incubated for 10 min at 37 °C in the dark and then centrifuged for 10 min at 4000 rpm. The Vis spectrum of the TBA–MDA complex was subsequently recorded from 400 to 800 nm. The absorbance of the complex in the supernatant was read at 532 nm and used to calculate the percentage inhibition of lecithin peroxidation using the following equation:

$$\text{Inhibition of lecithin peroxidation}\,(\%) = (A_C - A_S)\times\frac{100}{(A_C - A_B)} \quad (1)$$

where A_C – absorbance of the control (aqueous solution of pure lecithin) which was UV-irradiated and treated with TBA solution, A_S – absorbance of the sample (lecithin/flavonoids mixture) which was UV-irradiated and treated with TBA solution and A_B – absorbance of the blank (aqueous solution of pure lecithin which is not UV-irradiated but treated with TBA solution, thereby monitoring the MDA level in the lecithin before UV-irradiation).

RESULTS

The absorption spectra of flavonoids consist of two distinctive bands in a broad range of 240–400 nm. Band I, covering the range 300–380 nm, is attributed to the B-ring (with A_{max} around 350–370 nm), while band II, covering the range of 240–280 nm (with A_{max} around 260–270 nm) is attributed to the A–C benzoyl system; a weak band with an absorption maximum around 300 nm was also detected; it is attributed to the C-ring only (Figs. 1, 2A, 3A and 4A).

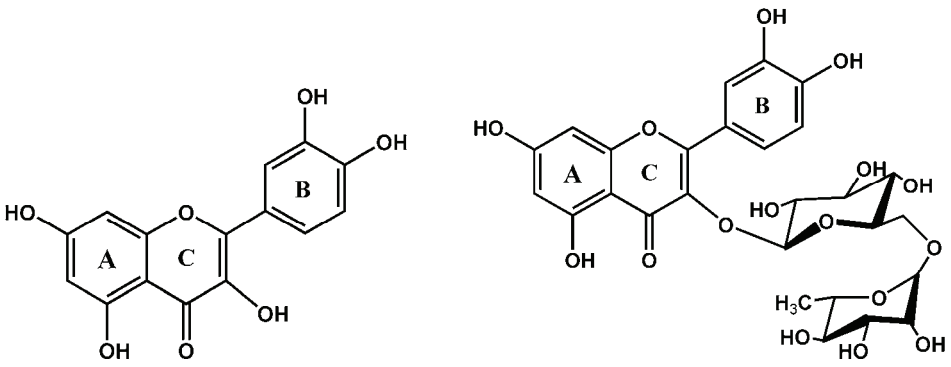

(A) (B)

Fig. 1. Structure of A) quercetin and B) rutin.

The changes in the absorption spectra of rutin exposed to UV-C radiation in methanol are shown in Fig. 2A. The maximum absorbance of rutin (A_{max}= 350 nm) decreased proportionally with the length of the irradiation time (t_{irr}). A kinetic log plot, log A_{max}(350 nm) = $f(t_{irr})$, is shown in Fig. 2B. The plot shows a good linear fitting, with R values of about 0.99. The bleaching kinetics seems to obey a first-order law. Rutin showed a very similar response during irradiation with UV-B and UV-A light (not shown).

The changes in the absorption spectra of rutin exposed to UV-B radiation in water are shown in Fig. 3A. The maximum absorbance of rutin (A_{max} = 350 nm) decreased proportionally with the irradiation time (t_{irr}). A kinetic log plot, log A_{max}(350 nm) = $f(t_{irr})$, is shown in Fig. 3B. The plots show a good linearity, with R values of about 0.99. The bleaching kinetics seems to obey a first-order law again. Rutin expressed very similar responses during irradiation with UV-C and UV-A light in water (not shown).

The changes in the absorption spectra of quercetin exposed to UV-B radiation in methanol are shown in Fig. 4A. The maxima of the two absorption bands of quercetin (A_{max} = 370 nm and 250 nm) decrease proportionally with the irradiation time. The corresponding kinetic log plot, log A_{max}(370 nm) = $f(t_{irr})$, is shown in Fig. 4B. The plot shows a good linear fit, with R values of about 0.98. The bleaching kinetics seems to obey a first-order law. On the other hand and

contrary to the behaviour of rutin irradiated in a methanolic solution, a slow but continuous rise in the absorbance of quercetin at 290 nm was detected with increasing irradiation time; the log A_{max}(290 nm) = $f(t_{irr})$ dependence also corresponded to 1st order kinetics. Quercetin exhibited very similar behaviour during irradiation with UV-C and UV-A light in methanol (not shown).

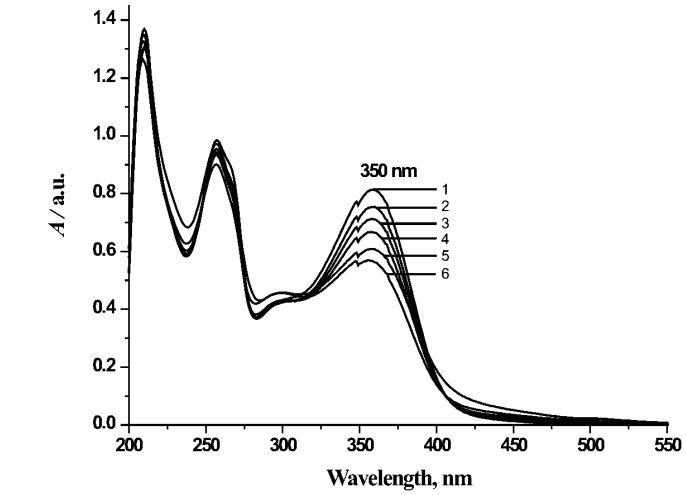

(A)

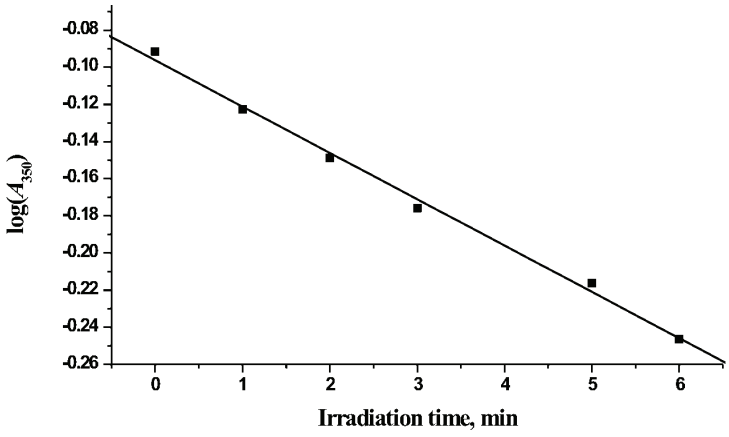

(B)

Fig. 2. Rutin in methanol irradiated with UV-C light. A) The changes in the absorption spectra of rutin exposed to UV-C radiation in methanol for 1 – 0; 2 – 1; 3 – 2; 4 – 3; 5 – 5; 6 – 6 min. B) The corresponding kinetic log plot obtained by following the A_{max} values at 350 nm (band I), as a function of the irradiation period (t_{irr}), log A_{max}(350 nm) = $f(t_{irr})$. The concentration of rutin was 8.5×10^{-5} M.

The time dynamics of the production of lipid peroxides in the lecithin lipoidal mixture because of UV-irradiation in the absence (control) and in presence of quercetin and rutin (sample) are shown in Fig. 5. The amount of peroxidation was estimated *via* the TBA–MDA test, by measuring the absorbance of the formed TBA–MDA complex at 532 nm.

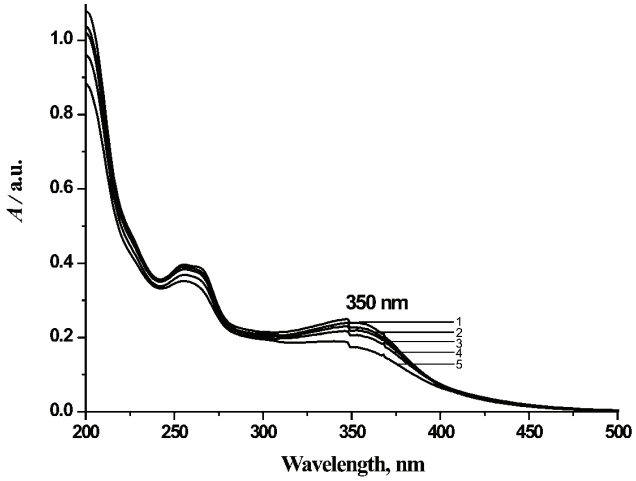

(A)

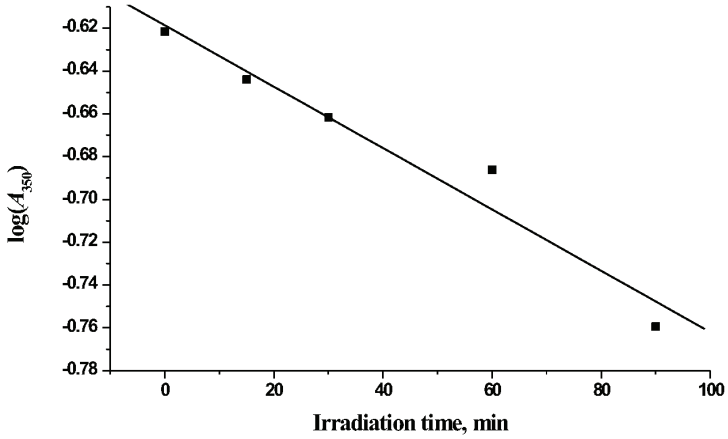

(B)

Fig. 3. Rutin in water irradiated with UV-B light. A) The changes in the absorption spectra of rutin exposed to UV-B radiation in water for 1 – 0; 2 – 15; 3 – 30; 4 – 60; 5 – 90 min. B) The corresponding kinetic log plot obtained by following the A_{max} values at 350 nm (band I), as a function of the irradiation period (t_{irr}), log A_{max}(350 nm) = $f(t_{irr})$. The concentration of rutin was 8.5×10^{-5} M.

The kinetics of change in the percent inhibition of UV-induced lipid peroxidation, by quercetin and rutin in aqueous solutions containing the two flavonoids

(7×10^{-5} M) and soybean lecithin lipoidal mixture (2×10^{-3} M) are shown in Fig. 6. The inhibition was calculated from Eq. (1).

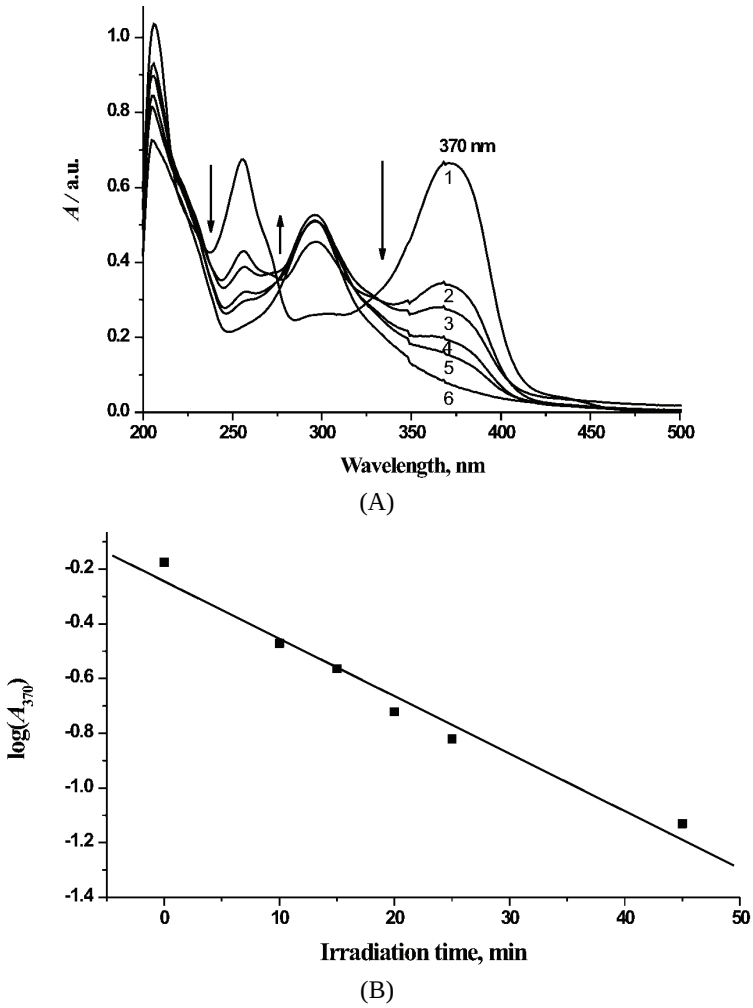

Fig. 4. Quercetin in methanol irradiated with UV-B light. A) The changes in the absorption spectra of quercetin exposed to UV-B radiation in methanol for 1 – 0; 2 – 10; 3 – 15; 4 – 20; 5 – 25; 6 – 45 min. B) The corresponding kinetic log plot obtained by following the A_{max} values at 370 nm (band I), as a function of the irradiation period (t_{irr}), $\log A_{max}(370\text{ nm}) = f(t_{irr})$. The concentration of quercetin was 8.5×10^{-5} M.

The calculated slopes (k_1) ($y_1 = k_1x + n$; y_1 – log (absorbance of rutin and quercetin in different solvents at 350 and 370 nm, respectively); x – UV-irradiation time) are presented in Table I. Such a presentation provides comparison of the corresponding slopes (obtained from the plots shown at Figs. 2B, 3B and 4B),

i.e., rates of the degradation (bleaching) of flavonoids during UV-irradiation of three different UV sub-ranges: 254 (UV-C), 300 (UV-B) and 350 nm (UV-A).

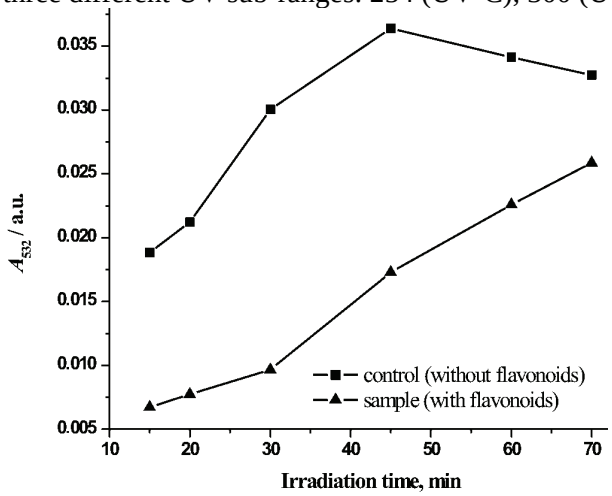

(A)

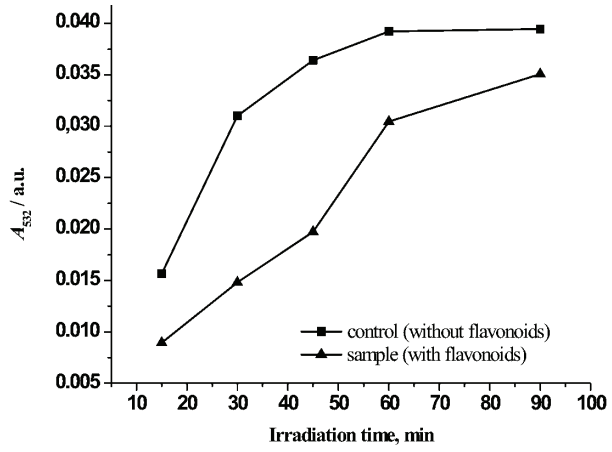

(B)

Fig. 5. Time dynamics of lipid peroxides production because of UV-A irradiation in the absence (control) and in the presence of A) quercetin and B) rutin (sample) in a lecithin lipoidal mixture, which was kept at the same concentration in both cases. The amount of peroxidation was estimated by TBA–MDA test, by measuring absorbance of the corresponding complex at 532 nm.

The calculated slopes represent the changes in the antioxidant activities of quercetin and rutin, followed by the TBA–MDA test (explained in the Experimental), toward the lecithin lipoidal mixture as the protected target, as a result of continuous UV-irradiation from three UV sub-ranges, expressed as the changes in the inhibition of UV-induced lecithin (lipid) peroxidation (by the two flavonoids), and are given in Table II. The slopes (k_2) were calculated from the plot: log (% inhibition of lipid peroxidation) = $f(t_{irr})$; the inhibition was calculated using the formula given in the Experimental.

DISCUSSION

As it was stated in the Introduction, antioxidant action of flavonoids in the presence of a "protective target" (lecithin lipids in this study) may be potentially expressed in *i*) a preventive and/or *ii*) chain-breaking manner; the former action does not exclude the latter one, moreover both actions are undoubtedly related. *i.e.*, the more expressed are the preventative effects of flavonoids (through UV--absorption), the less are their chain-breaking actions necessary.

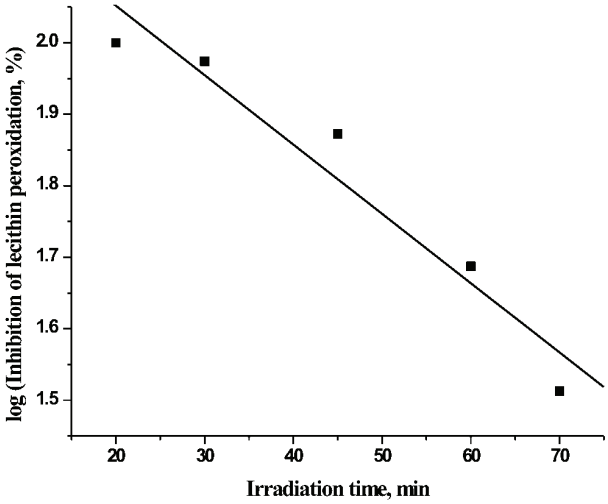

(A)

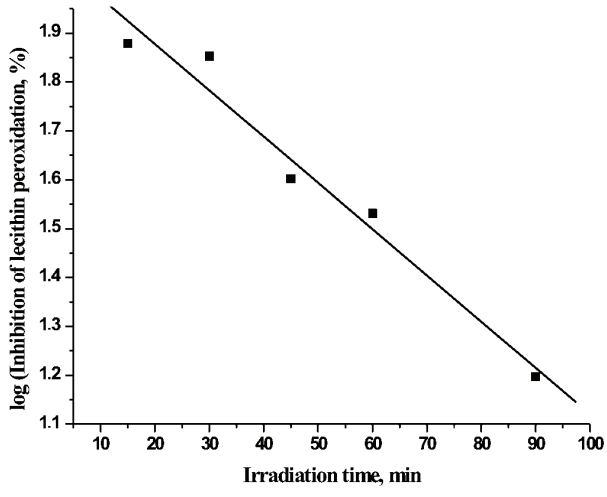

(B)

Fig. 6. Kinetics of change in the percentage (%) inhibition of UV--A-induced lipid peroxidation by quercetin (A) and rutin (B), in aqueous solutions containing the two flavonoids (7×10^{-5} M) and a soybean lecithin lipoidal mixture (2×10^{-3} M). The inhibition was calculated as described in the Experimental.

Flavonoids stability in the absence of lecithin: a measure of preventive antioxidant action

Both flavonoids expressed clear sensitivity to the action of UV radiation from all three UV-ranges. They underwent substantial bleaching as measured through the proportional decrease in the maximal absorbance of Band I as a function of radiation duration (t_{irr}), *i.e.*, log A_{max}(350 or 370 nm) = $f(t_{irr})$ (Figs. 2–4). These dependences are expressed as linear plots (Figs. 2–4), indicating first order kinetics of the degradation of the flavonoids. This conclusion does not question the possible presence of other species, mostly radical ROS, in the irradiated system (as a result of UV-irradiation), as well as their potential role in the mechanism of flavonoid degradation.[17,24]

TABLE I. Kinetics of rutin and quercetin degradation (bleaching) in methanol and water, during UV-irradiation in three different UV sub-ranges: 254 (UV-C), 300 (UV-B) and 350 nm (UV-A). The absorbances of rutin and quercetin were taken from the corresponding absorption spectra (Figs. 2–4) at 350 and 370 nm, respectively

Solvent	k_1 / min^{-1} (R)		
	Wavelength, nm		
	254 (UV-C)	300 (UV-B)	350 (UV-A)
	Rutin		
Methanol	–0.0250 (–0.998)	–0.00173 (–0.917)	–0.00016 (–0.923)
Water	–0.0514 (–0.990)	–0.00143 (–0.977)	0.00170 (0.996)
	Quercetin		
Methanol	–0.111 (–0.985)	–0.0210 (–0.986)	–0.00312 (–0.995)

TABLE II. Kinetics of the change in the percentage (%) of inhibition of (UV)-induced lipid peroxidation, by quercetin and rutin, in water solution containing two flavonoids (7×10^{-5} M) and a soybean lecithin lipoidal mixture (2×10^{-3} M), during UV-irradiation in three different UV sub-ranges: 254 (UV-C), 300 (UV-B) and 350 nm (UV-A). The change was followed by the TBA–MDA test

Wavelength, nm	k_2 / min^{-1} (R)	
	Quercetin	Rutin
254 (UV-C)	–0.170 (–0.944)	–0.28680 (–0.999)
300 (UV-B)	–0.0414 (–0.917)	–0.06880 (–0.970)
350 (UV-A)	–0.00970 (–0.969)	–0.00946 (–0.984)

Evidently, flavonoids bleaching are highly dependent on the energy input of the UV radiation; in both cases, a switch from the UV-A to the UV-B lamp and from the UV-B to the UV-C lamp led to a corresponding increase in the related bleaching rate constants by an order of magnitude (Table I). This behaviour was observed in the other studies related to continuous UV-irradiation.[29] Even the mutual relationship of the bleaching rate constants for the two flavonoids ($k_{bleach.,querc.}/k_{bleach.,rutin}$) is UV-energy dependent: from 4.4 (UV-A) over 12.1

(UV-B) to 19.4 (UV-C) in favour of quercetin, which appears to be less UV-resistant, compared to rutin in the same solvent (methanol). It is evident that the substituent at position 3 in the C-ring affects this difference as it was proposed the OH-group at this position makes quercetin more vulnerable to UV-action, compared to the glycoside residue in the case of rutin.[30]

In addition, a clear increase in the absorbance of quercetin was detected in the range between 280 and 320 nm, with a maximum around 290 nm, implying the formation of a UV-irradiation product. However, this was not of relevance for this work.

Flavonoids suppression of lecithin peroxidation

An estimation of flavonoids suppression of lipid peroxidation and its change because of UV-irradiation was realised in an indirect manner. Direct measurements of possible flavonoids scavenging of UV-created lipid ($L^{\bullet}$) and lipoperoxy ($LOO^{\bullet}$) radical species in investigated aqueous system (chain-breaking antioxidant action) was not possible because the required techniques were not available. Instead, the TBA–MDA test (which indirectly measures the amount of lipid peroxidation)[31,32] was employed in the presence and in the absence of the two flavonoids and the difference was attributed to the antioxidant activities of the flavonoids, not only through the chain-breaking action but also through direct UV-absorption.

The patterns of the peroxidation of the studied lecithin in the absence (control) and in the presence of the flavonoids (sample) are shown in Fig. 5; both plots were obtained with UV-A irradiation to be more comparable. As can be seen, the control pattern expresses a typical curve shape, beginning with a relatively sharp rise, reflecting the fast proliferation of the lipid peroxidation chain in the initial period of UV-irradiation, and finishing at some plateau level. In the latter case, for longer periods of UV-irradiation, equilibrium between the UV-induced production of peroxides and their simultaneous degradation exists. It is well known that (lipid) peroxides themselves are very unstable species, prone to self-degradation.[33] The sample patterns in the presence of both quercetin and rutin are obviously different (Fig. 5). Even in the initial phase, the flavonoids significantly reduce the amount of peroxidation, and continue to do so in an almost in linear manner until the end of the UV-irradiation process, when the plateau level (reflecting the production/degradation equilibrium of the peroxides) had already been established. Similar responses were obtained with UV-B and UV-C irradiation.

Thus, both quercetin and rutin retained their antioxidant behaviour under continuous UV-irradiation regime. However, it is questionable whether the "quantity" of their antioxidant activities remained at the same level, or changed under the employed UV-irradiation regime. Ioku and coworkers[34] found that

quercetin expressed a higher peroxyl radical-scavenging activity against methyl linoleate in solution (as the protective target) compared to its glucosides, similar to rutin, when peroxidation was initiated by a thermal 2,2'-azobis(2,4-dimethyl-valeronitrile (AMVN) initiator. Figure 6 explains what happens when UV-initiation was employed. The plots show a linear decreasing change in the flavonoid inhibition of lecithin peroxidation with increasing duration of UV-irradiations; in other words, the flavonoids antioxidant capacities are reduced under a continuous UV-irradiation regime. As can be seen from Table II, the quantity of change is directly proportional to the energy of incident photons. In the case of quercetin, the (antioxidation activity) attenuation factor (on switching from UV-A to UV-B, and from UV-B to UV-C) is about 4; in the case of rutin, the attenuation (diminution) factor for the UV-A/UV-B switch is about 7, and for UV-B/UV-C switch about 4, the same as for quercetin. Bearing in mind the previously cited greater stability of rutin, compared to quercetin, under a similar UV-irradiation regime when lecithin was absent, this could seem somewhat surprising. It evidently suggests that the higher resistance of rutin towards UV-irradiation (compared to quercetin) plays only a partial role in the protection of its antioxidant activity under the same UV-irradiation regime; the other, probably more significant factor might be related to the free radical species created in the system because of prolonged UV-irradiation, and the involved mechanisms.

ИЗВОД

ЕФЕКТИ КОНТИНУАЛНОГ УЛТРАЉУБИЧАСТОГ ОЗРАЧИВАЊА НА АНТОКСИДАТИВНУ АКТИВНОСТ КВЕРЦЕТИНА И РУТИНА У РАСТВОРУ У ПРИСУСТВУ ЛЕЦИТИНА КАО ЗАШТИТНЕ МЕТЕ

ДРАГАН ЦВЕТКОВИЋ[1], ДЕЈАН МАРКОВИЋ[1], ДРАГАНА ЦВЕТКОВИЋ[2] и БЛАГА РАДОВАНОВИЋ[3]

[1]Технолошки факултет, 16 000 Лесковац, [2]Невена колор, д.о.о, 16 000 Лесковац и [3]Природно–математички факултет, Одсек за хемију, 18 000 Ниш

У овом раду је проучавана стабилност и антиоксидативна активност два изабрана флавоноида, кверцетина и рутина, растворена у метанолу и води, према дејству контунуалног ултраљубичастог (UV) озрачивања из три различита под-опсега, UV-A, UV-B и UV-C. Флавоноиди подлежу разградњи пратећи кинетику првог реда. Константе брзине деградације (bleaching-a) су веома зависне од енергије UV-фотона. Антиоксидативна активност два флавоноида у односу на UV-индуковану липидну пероксидацију лецитина проучавана је TBA–MDA тестом, и нађено је да на њу такође утиче режим UV континуалног озрачивања. Енергија UV-фотона и овде игра главну улогу, али се ни утицај флавоноидних структура не може занемарити.

(Примљено 23. новембра 2010, ревидирано 20. јануара 2011)

REFERENCES

1. A. H. Teramura, L. H. Ziska, In *Photosynthesis and the Environment*, Kluwer Academic Publishers, Dordrecht, 1996, p. 436

2. C. L. Bailaré, A. L. Scopel, A. E. Stapleton, M. J. Yanovsky, *Plant Physiol*. **112** (1996) 161
3. C. E. Lovelock, B. F. Clough, I. E. Woodrow, *Planta* **188** (1992) 143
4. V. G. Kakani, K. R. Reddy, D. Zhao, A. R. Mohammed, *Ann. Bot.* **91** (2003) 817
5. M. A. Schumaker, J. H. Bassman, R. Robberecht, G. K. Radamaker, *Tree Physiol*. **17** (1997) 617
6. A. Strid, J. R. Porra, *Plant Cell Physiol.* **33** (1992) 1015
7. G. Deckmyn, C. Martens, I. Impens, *Plant Cell Environ.* **17** (1994) 295
8. R. Barbato, A. Frizzo, G. Friso, F. Rigoni, G. M. Giacometti, *Europ. J. Biochem.* **227** (1995) 723
9. J. F. Bornman, A. H. Teramura, *Environmental UV photobiology*, Plenum Press, New York, USA, 1993, p. 427
10. I. Panagopoulos, J. F. Bornman, L. O. Bjorn *Physiol. Plant.* **84** (1992) 140
11. E. M. Middleton, A. H. Teramura, *Photochem. Photobiol*. **60** (1994) 38
12. A. Melis, A. J. Nemson, M. A. Harrison, *Biochim. Biophys. Acta* **1100** (1992) 312
13. A. Karioti, C. K. Kitsaki, S. Zygouraki, M. Ziobora, S. Djeddi, H. Skaltsa, G. Liakopoulos, *Flora* **203** (2008) 602
14. L. Tao, Z. T. Wang, E. Y. Zhu, Y. H. Lu, D. Z. Wei, *S. Afr. J. Bot*. **72** (2006) 163
15. E. M. Middleton, A. H. Teramura, *Plant Physiol*. **103** (1993) 741
16. K. E. Heim, A. R. Tagliaferro, D. J. Bobilya, *J. Nutr. Biochem*. **13** (2002) 572
17. W. Bors, W. Heller, C. Michel, M. Saran, *Methods Enzymol*. **186** (1990) 343
18. D. Amić, D. Davidović-Amić, D. Bešlo, N. Trinajstić, *Croat. Chem. Acta* **76** (2003) 55
19. D. P. Makris, J. T. Rossiter, *Food Chem.* **77** (2002) 177
20. S. Erkoc, F. Erkoc, N. Keskin, *J. Mol. Struct.: THEOCHEM* **631** (2003) 141
21. F. Nessa, Z. Ismail, N. Mohamed, M. Haris, *Food Chem*. (2004) 1
22. J. Aikens, T. Dix, *Arch. Biochem. Biophys.* **305** (1993) 516
23. A. Girotti, *J. Photochem. Photobiol. B* **63** (2001) 103
24. W. Bors, C. Michel, M. Saran, *Methods Enzymol*. **234** (1994) 41
25. D. Cvetković, D. Marković, *J. Serb. Chem. Soc.* **72** (2007) 235
26. D. Cvetković, D. Marković, *Radiat. Phys. Chem.* **77** (2008) 34
27. C. Choi, S. Kim, S. Hwang, B. Choi, H. Ahn, M. Lee, S. Park, S. Kim, *Plant Sci.* **163** (2002) 1161
28. J. Fernandez, J. Perez-Alvarez, J. Fernandez-Lopez, *Food Chem.* **59** (1997) 345
29. S. Tommasini, M. L. Calabro, P. Donato, D. Raneri, G. Guglielmo, P. Ficarra, R. Ficarra, *J. Pharm. Biomed. Anal*. **35** (2004) 389
30. G. Smith, S. J. Thomsen, K. R. Markham, C. Andary, D. Cardon, *J. Photochem. Photobiol. A* **136** (2000) 87
31. A. Saija, M. Scalese, M. Lanza, D. Marzullo, F. Bonina, F. Castelli, *Free Radic. Biol. Med*. **19** (1995) 481
32. Q. Cai, R. O. Rahn, R. Zhang, *Cancer Lett*. **119** (1997) 99
33. W. A. Girotti, *J. Free Radic. Biol. Med.* **1** (1985) 87
34. K. Ioku, T. Tsushida, Y. Takei, N. Nakatani, J. Terao, *Biochim. Biophys. Acta* **1234** (1995) 99.

Journal of the Serbian Chemical Society
JSCS-info@shd.org.rs • www.shd.org.rs/JSCS
J. Serb. Chem. Soc. 76 (7) 987–994 (2011)
JSCS–4177
UDC 582.293.378+634.22:543.613.3
Original scientific paper

Volatile constituents of selected Parmeliaceae lichens

IGOR Ž. STOJANOVIĆ[1], NIKO S. RADULOVIĆ[2#], TATJANA LJ. MITROVIĆ[3], SLAVIŠA M. STAMENKOVIĆ[3] and GORDANA S. STOJANOVIĆ[2*]

[1]Department of Pharmacy, Faculty of Medicine, University of Niš, Bul. Z. Đinđića 81, 18000 Niš, [2]Department of Chemistry, Faculty of Science and Mathematics, University of Niš, Višegradska 33, 18000 Niš and [3]Department of Biology and Ecology, Faculty of Science and Mathematics, University of Niš, Višegradska 33, 18000 Niš, Serbia

(Received 4 October, revised 27 December 2010)

Abstract: The acetone soluble fraction of the methanol extracts of Parmeliaceae lichens: *Hypogymnia physodes*, *Evernia prunastri* and *Parmelia sulcata*, growing on the same host tree (*Prunus domestica*) and at the same locality was analyzed for the first time by GC and GC–MS. The major identified components were olivetol (33.5 % of the *H. physodes* extract), atraric acid (30.1 and 30.3 % of the *E. prunastri* and *P. sulcata* extracts, respectively), orcinol (25.0 % of the *E. prunastri* extract), vitamin E (24.7 % of the *P. sulcata* extract) and olivetonide (15.7 % of the *H. physodes* extract). Even though all the identified compounds are known, a number of them were found for the first time in the examined lichens, *i.e*., orcinol monomethyl ether (*H. physodes*), orcinol, atranol, lichesterol, ergosterol (*H. physodes* and *P. sulcata*), methyl haematommate, atraric acid, olivetol, vitamin E (*H. physodes* and *P. sulcata*) and *β*-sitosterol (*P. sulcata*).

Keywords: *Hypogymnia physodes*; *Evernia prunastri*; *Parmelia sulcata*; volatile constituents.

INTRODUCTION

Lichens are probably the earliest colonizers of terrestrial habitats on Earth, with fossil records tracing back to 400–600 million years ago.[1,2] These fossils indicate that fungi developed symbiotic partnerships with photoautotrophs before the evolution of vascular plants. There are about 300 genera and 18000 species of presently recognized lichens. They produce more than 800 unique secondary metabolites as adaptations for growing in harsh living conditions. Most of the secondary metabolites present in lichens are produced through the polyketide pathway and consist mainly of monocyclic phenols, bicyclic phenols joined by an

* Corresponding author. E-mail: stgocaus@yahoo.com; gocast@pmf.ni.ac.rs
# Serbian Chemical Society member.
doi: 10.2298/JSC101004087S

ester bond (depsides), both ester and ether bonds (depsidones) or a furan heterocycle (dibenzofurans and usnic acid), anthraquinones, xanthones, chromones and secondary aliphatic acids and esters.[3]

The production of secondary metabolites is costly to the organisms in terms of nutrient and energy; hence, one would expect that the plethora of metabolites produced by lichens would have biological significance to the organisms. Some of the possible biological functions of lichen metabolites, as summarized by Huneck and Yoshimura,[4] are:

– Antibiotic activities – provide protection against microorganisms.

– Photoprotective activities – aromatic substances that absorb UV light to protect photobionts from intensive irradiation.

– Promote symbiotic equilibrium by affecting the cell wall permeability of photobionts.

– Chelating agents – capture and supply of important minerals from the substrate.

– Antifeedant/antiherbivory activities – protect the lichens from insect and animal feedings.

To date, high-pressure liquid chromatography (HPLC) methods have been used most frequently for the analysis of the secondary metabolites in lichens.[5,6] Gupta *et al*.[5] developed an HPLC method with photodiode array detection for the determination of methyl β-orcinolcarboxylate and ethyl haematommate in the thalii of various lichen species.

Identification of atranorin, chloratranorin, atranol, chloratranol and esters of haematommic acid by HPLC–MS using negative ion atmospheric pressure chemical ionisation in oakmoss absolute was reported by Hiserdodt *et al*.[6] HPLC methods, however, need standards for compound identification or isolation of extract constituents and their structure elucidation. The economic factor of very expensive HPLC grade solvents and long analysis time should not be neglected. In addition, the volatile part of the extracts might represent a minor proportion of the constituents and consequently identification by HPLC could be difficult or even impossible. On the other hand, good software (such as Amdis[7]) for searching various MS libraries (Adams[8], Wiley[9], and Massfinder[10]) enables constituent identification by GC–MS for many known compounds without isolation and standards.

Direct GC–MS analysis of a solvent extract is not straightforward because of the non-volatile residue, which remains undetected and stuck in the chromatographic system. However, GC–MS gave good results with mono-aromatic compounds in an oak moss absolute fraction,[11] identification and quantification of atraric acid,[12] and the fatty acids of the genus *Collema* lichens.[13]

Only HPLC fingerprints of various lichen species[5] have been exploited to date, whereas, to the best of our knowledge, there have been no attempts at

creating a database of GC–MS profiles of lichen volatiles. Herein for the first time, the composition of the volatiles from the acetone soluble fractions of the methanol extracts of the lichen species: *Hypogymnia physodes*, *Evernia prunastri* and *Parmelia sulcata*, growing on the same host tree, collected at the same time and locality, are reported. The presented results might help in the enlightenment of relationships between lichens and their host and indicate the possibilities of GC–MS for the analyses of secondary metabolites in lichens.

EXPERIMENTAL

Lichen material

Lichens species: *Hypogymnia physodes* (L.) Nyl., (syn: *Parmelia duplicata* var. *Douglasicola* Gyelnik, *Parmelia physodes* (L.) Ach., *Parmelia oregana* Gyelnik; common names: monk's-hood lichen, hooded tube lichen, puffed lichen), *Evernia prunastri* (L.) Ach. (common name: oakmoss), and *Parmelia sulcata* Taylor (common name: shield lichen) growing on a *Prunus domestica* tree were collected on the locality: Serbia, Niš, Suva Planina (meaning "dry mountain" in Serbian, Bojanine vode, altitude of 860 m above sea level, coordinates 43° 10' N, 22° 10' E in April 2009). The lichen material was air-dried for 10 days and stored at ambient temperature (25±2 °C) without exposure to direct sunlight. Voucher specimens were deposited in the Herbarium collection at the Department of Biology and Ecology, Faculty of Science and Mathematics, University of Niš under the acquisition numbers: 17 (*H. physodes*), 18 (*E. prunastri*), and 20 (*P. sulcata*). Taxonomical identifications were performed by Dr. Slaviša Stamenković, Department of Biology and Ecology, Faculty of Science and Mathematics, University of Niš.

Extraction

Powdered, air-dried lichen material (10 g) was extracted with methanol (250 mL) in the dark at room temperature for 24 h. The methanol was evaporated under reduced pressure. The extract yields were 14.4 % (*H. physodes*), 11.5 % (*E. prunastri*) and 11.0 % (*P. sulcata*). The dry residues were then extracted with acetone (3 x 20 mL). The acetone was evaporated under reduced pressure. The percentages of the acetone-soluble fractions calculated based on the dry methanol extract were: 53.9 % (*H. physodes*), 57.6 % (*E. prunastri*) and 32.1 % (*P. sulcata*).

GC–MS and GC analyses

The GC–MS analyses were realised using a Hewlett-Packard 6890N gas chromatograph equipped with a fused silica capillary column DB-5MS (5 % phenylmethylsiloxane, 30 m×0.25 mm, film thickness 0.25 μm, Agilent Technologies, USA) and coupled to a 5975B mass selective detector from the same company. The injector and interface were operated at 250 and 380 °C, respectively. The oven temperature was raised from 70–290 °C at a heating rate of 5 °C min^{-1} and then held isothermally for 10 min. Helium at a flow rate of 1.0 mL min^{-1} was used as the carrier gas. The samples, 1 μL of the acetone solutions (1:100), were injected in a pulsed split mode (the flow was 1.5 mL min^{-1} for the first 0.5 min and then set to 1.0 mL min^{-1} throughout the remainder of the analysis; split ratio 40:1). The MS conditions were as follows: ionization voltage of 70 eV, acquisition mass range 35–500 and scan time 0.32 s. The extract constituents were identified based on their linear retention indices (relative to C12––C33 alkanes on the DB-5MS column) and by the application of the AMDIS software (automated Mass Spectral Deconvolution and Identification System, Ver. 2.1, DTRA/NIST, 2002).

The GC (FID) analyses were performed under the same experimental conditions using the same column as described for the GC–MS. The relative proportions of the constituents were percentages from the GC peak areas without any corrections.

RESULTS AND DISCUSSION

Qualitative composition and relative abundances of the volatiles of acetone fractions are presented in Table I. Structures of main aromatic constituents are shown in Table II and in Fig. 1.

TABLE I. Volatiles (%) of the acetone soluble fraction of the methanol extract of the examined Parmeliaceae lichens

Compound	*RI*[a]	*H. physodes*	*E. prunastri*	*P. sulcata*
3-Methoxy-5-methylphenol (*syn.* orcinol monomethyl ether)	1317	t[b]	5.7	–[b]
5-Methylbenzene-1,3-diol (*syn.* orcinol)	1369	0.6[b]	25.0	t[b]
3-Chloro-2,6-dihydroxy-4-methylbenzaldehyde (*syn.* chloroatranol)	1494	0.5[b]	–	–
2,6-Dihydroxy-4-methylbenzaldehyde (*syn.* atranol)	1546	5.1[b]	2.1	5.2[b]
Methyl 2-hydroxy-4-methoxy-6-methylbenzoate (*syn.* sparassol)	1580	–	1.6	–
Methyl 2,4-dihydroxy-6-methylbenzoate (*syn.* methyl orsellinate)	1661	–	10.2	–
Methyl 3-formyl-2,4-dihydroxy-6-methylbenzoate (*syn.* methyl haematommate)	1669	1.5[b]	3.4	1.9[b]
Methyl 2,4-dihydroxy-3,6-dimethylbenzoate (*syn.* methyl *β*-orcinolcarboxylate; atraric acid)	1703	17.2[b]	30.1	30.3[b]
2,4-Dihydroxy-6-methylbenzoic acid (*syn.* orsellinic acid)	1745	–	1.1	–
5-Pentylbenzene-1,3-diol (*syn.* 5-pentylresorcinol; olivetol)	1755	33.5[b]	–	1.6[b]
Hexadecanoic acid (*syn.* palmitic acid)	1958	0.9	t	2.1
(9*Z*,12*Z*)-9,12-octadecadienoic acid (*syn.* linoleic acid)	2128	0.6	0.9	2.1
(9*Z*,12*Z*,15*Z*)-9,12,15- Octadecatrienoic acid (*syn.* *α*-linolenic acid)	2134	–	–	3.3
(9*Z*)-9-Octadecenoic acid (*syn.* oleic acid)	2141	3.2	t	3.5
Octadecanoic acid (*syn.* stearic acid)	2159	0.9	t	0.7
6,8-Dihydroxy-3-pentylisochromen-1-one (*syn.* olivetonide)	2290	15.7	–	–
2,4-Dihydroxy-6-(2-oxoheptyl)benzoic acid (*syn.* olivetonic acid)	2337	7.7	–	–
2,6-Diacetyl-3,7,9-trihydroxy-8,9*b*-dimethyl-9b*H*-dibenzofuran-1-one (*syn.* usnic acid)	2706	–	11.4	–
Nonacosane	2900	–	–	2.4
α-Tocopherol (*syn.* vitamin E)	3112	0.6[b]	–	24.7[b]
Ergosta-5,8,22-trien-3*β*-ol (*syn.* lichesterol)	3147	1.3[b]	t	1.8[b]

TABLE I. Continued

Compound	*RI*[a]	*H. physodes*	*E. prunastri*	*P. sulcata*
Ergosta-5,7,22-trien-3*β*-ol (*syn.* ergosterol)	3177	2.1[b]	t	4.5[b]
Stigmast-5-en-3*β*-ol (*syn. β*-sitosterol)	3297	–	–	10.6[b]
Total		91.4	91.5	91.4

[a]Experimental retention indices; [b]found for the first time in the lichen taxon, t: trace amount (<0.05 %), –: not detected

TABLE II. Structures of some of the compounds identified in the examined lichen extracts

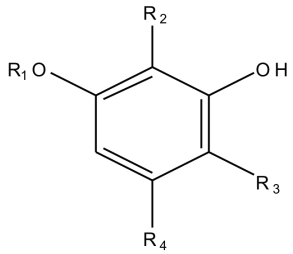

Compound	R_1	R_2	R_3	R_4
Orcinol monomethyl ether	CH_3	H	H	CH_3
Orcinol	H	H	H	CH_3
Chloroatranol	H	CHO	Cl	CH_3
Atranol	H	CHO	H	CH_3
Sparassol	CH_3	H	$COOCH_3$	CH_3
Methyl orsellinate	H	H	$COOCH_3$	CH_3
Methyl haematommate	H	CHO	$COOCH_3$	CH_3
Atraric acid	H	CH_3	$COOCH_3$	CH_3
Orsellinic acid	H	H	COOH	CH_3
Olivetol	H	H	H	C_5H_{11}

All the obtained chromatograms of the examined extracts showed only a few prominent peaks corresponding to components present in significant amounts (*i.e.*, more than 10 %): *E. prunastri* 4 and *H. physodes* and *P. sulcata* both 3 %.

Orcinol and atraric acid were the major components of the *E. prunastri* extract, detected in approximately equal quantities and comprising together 55.1 %. Orcinol derivatives with the aldehyde group in the vicinity of two phenolic groups, atranol and methyl haematommate, were also present but in smaller quantities, as well as orcinol monomethyl ether. Among coupled phenolic compounds, only the dibenzofuran derivative usnic acid was identified. It seems possible that the volatility of other dibenzofurans, depsides and depsidones, was not sufficient for GC analysis.

Alongside atraric acid, that was present in all the investigated samples in considerable amounts, the *H. physodes* extract was composed of olivetol (33.5 %), olivetonide (15.7 %) and olivetonic acid (7.7 %).

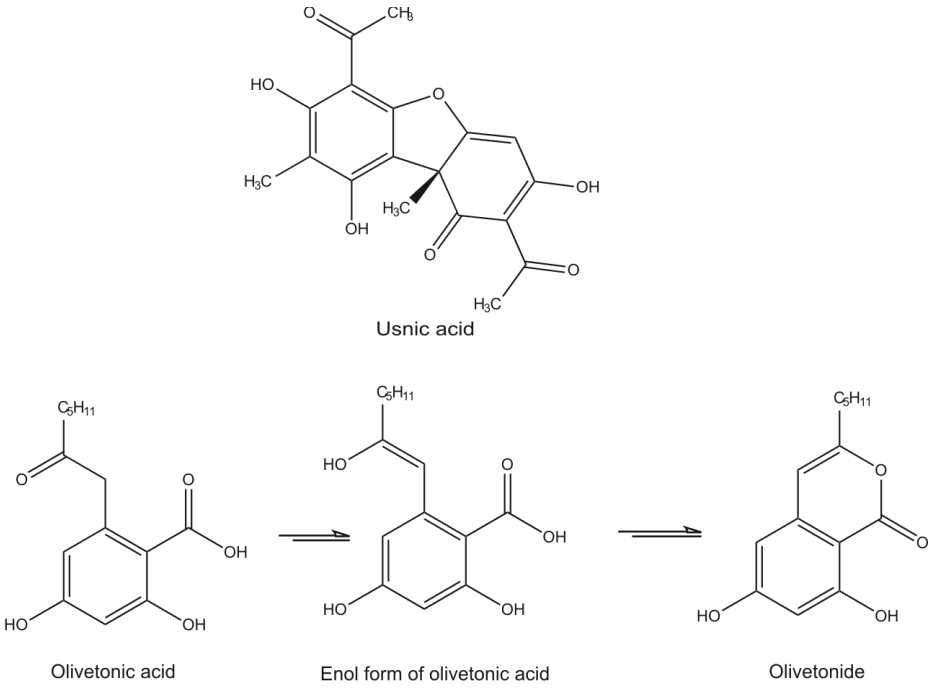

Fig. 1. Structures of usnic acid, olivetonic acid, its enol form and the lactone olivetonide.

The *P. sulcata* extract differed from the others in that it contained a high content of vitamin E (24.7 %) and three sterols comprising together 16.9 %. The methyl ester of *β*-orinolcarboxylic acid (atraric acid) was the most abundant mono-aromatic compound, followed by atranol.

Previously published results showed that *E. prunastri* extracts are characterized by the presence of evernic acid, evernin and usnic acid[14] while physodic, isophysodic, physodalic and 3-hydroxyphysodic acids dominated the *H. physodes* extracts.[15] Atranorin, usnic and salazinic acid[16] were detected in *P. sulcata* extracts.

The observed mono-aryl compounds in the lichen extracts could be both considered as authentic lichen metabolites but also as possible products of hydrolysis, transesterification and decarboxylation of depsides during the extraction and analysis processes.[17]

Hydrolysis of both evernin and atranorin produces methyl *β*-orcinolcarboxylate. Haematommic acid is also a hydrolytic product of atranorin and its decarboxylation yields atranol. Additionally, methyl *β*-orcinolcarboxylate hydrolysis of evernin leads also to 4-*O*-methylorsellinic acid, which upon decarboxylation gives orcinol monomethyl ether as the product that was identified in the *E. prunastri* and *H. physodes* extracts. The product of olivetoric acid hydrolysis is olivetonic acid, enol form of which in turn can be lactonized to olivetonide,

which was previously identified in an extract of treemoss (*Pseudoevernia furfuracea*) growing on cedar trees.[14] Olivetol was also found as one of *P. furfuracea* constituents.[18]

It is believed that the sterols detected in lichen extracts are true lichen metabolites but these could also have migrated from the host tree to the lichen.[14] In the present work, β-sitosterol was not detected in the *E. prunastri* and *H. physodes* extracts, while it was the third most abundant component (10.6 %) in the *P. sulcata* extract. Lichesterol and ergosterol were found in all examined extracts but in different quantities. The obtained results suggested that if sterols do migrate to the lichen from the host tree, the migration is dependent on both the nature of sterols and the lichen species.

The high contents of 5-alkyl resorcinols (orcinol and olivetol) in the examined extracts indicate that the related carboxylic acids (orsellinic and olivetonic acid) readily decarboxylate, contrary to methyl β-orcinolcarboxylate, which is stable under the above-specified experimental condition. Namely, β-orcinol (2,5--dimethylresorcinol) was not detected in any of the samples examined in this study.

CONCLUSIONS

The GC–MS profiles of the acetone-soluble fraction of the methanol extracts of Parmeliaceae lichens: *H. physodes*, *E. prunastri* and *P. sulcata*, growing on the same host tree (*Prunus domestica*) and at the same locality are relatively simple with a few dominant components. Olivetol (33.5 %), atraric acid (17.2 %) and olivetonide (15.7 %), were the major components of the *H. physodes* extract. Atraric acid constituted around one third of the *E. prunastri* and *P. sulcata* extracts. An additional characteristic of the *E. prunastri* extract was the high content of orcinol (25.0 %). The *P. sulcata* extract contained 24.7 % vitamin E. Even though all the identified compounds are known, a number of them were evidenced for the first time in the examined lichens: orcinol monomethyl ether (*H. physodes*), orcinol, atranol, lichesterol, ergosterol (*H. physodes*, *F. caperata* and *P. sulcata*), methyl haematommate, atraric acid, olivetol, vitamin E (*H. physodes* and *P. sulcata*) and β-sitosterol (*F. caperata* and *P. sulcata*).

Bearing in mind that all the investigated lichen species grew under the same conditions (host tree and locality) and were harvested at the same time, it could be concluded that the production of secondary metabolites of the lichens was not affected by the host tree or environmental factors and that observed differences in the extract compositions were genetically predetermined.

The obtained GC–MS profiles of the studied lichen volatiles could be considered as a useful complementary tool to HPLC–MS analysis for the differentiation of lichen specimens due to the availability and straightforwardness of the cheaper GC–MS analyses compared to HPLC–MS.

Acknowledgment. This work was funded by the Ministry of Education and Science of the Republic of Serbia (Project No. 172047).

И З В О Д

ИСПАРЉИВИ САСТОЈЦИ ОДАБРАНИХ PARMELIACEAE ЛИШАЈЕВА

ИГОР Ж. СТОЈАНОВИЋ[1], НИКО С. РАДУЛОВИЋ[2], ТАТЈАНА Љ. МИТРОВИЋ[3], СЛАВИША М. СТАМЕНКОВИЋ[3] и ГОРДАНА С. СТОЈАНОВИЋ[2]

[1]*Одсек Фармација, Медицински факултет, Универзитет у Нишу, Бул. др Зорана Ђинђића 81, 18000 Ниш,* [2]*Одсек за хемију, Природно-математички факултет, Универзитет у Нишу, Вишеградска 33, 18000 Ниш и* [3]*Одсек за биологију и екологију, Природно-математички факултет, Универзитет у Нишу, Вишеградска 33, 18000 Ниш*

Ацетонска фракција метанолних екстраката Parmeliaceae лишајева: *Hypogymnia physodes*, *Evernia prunastri* и *Parmelia sulcata*, сакупљених са истог супстрата (*Prunus domestica*) и локалитета, анализирана је методама гасне хроматографије и гасне хроматографије са масеним детектором (GC и GC–MS) по први пут. Главне идентификоване компоненте екстраката су: оливетол (33,5 %, *H. physodes*), атрарна киселина (30,1 и 30,3 %, *E. prunastri* и *P. sulcata*, редом), орцинол (25,0 %, *E. prunastri*), витамин E (24,7 % *P. sulcata*) и оливетонид (15,7 % *H. physodes*). Све идентификоване компоненте су познате, али су неке од њих по први пут идентификоване у испитиваним лишајевима: орцинол-монометил-етар (*H. physodes*), орцинол, атранол, личестерол, ергостерол (*H. physodes* и *P. sulcata*), метил-хематомат, атрарна киселина, оливетол, витамин E (*H. physodes* и *P. sulcata*) и *β*-ситостерол (*P. sulcata*).

(Примљено 4. октобра, ревидирано 27. децембра 2010)

REFERENCES

1. T. N. Taylor, H. Hass, W. Remy, H. Kerp, *Nature* **5** (1995) 244
2. X. Yuan, S. Xiao, T. N. Taylor, *Science* **308** (2005) 1017
3. A. Karagoz, N. Dogruoz, Z. Zeybek, A. Aslan, *J. Med. Plants Res*. **3** (2009) 1034
4. S. Huneck, I. Yoshimura, *Identification of Lichen Substances*, Springer, Berlin, 1996
5. V. K. Gupta, M. P. Arokar, D. Saikia, A. Pal, A. Fatima, *Pharm. Biol.* **45** (2007) 200
6. R. D. Hiserodt, D. F. H. Swijter, C. J. Mussinan, *J. Chromatogr. A* **888** (2000) 103
7. *Automated Mass Spectral Deconvolution and Identification System*, Ver. 2.1, DTRA/ /NIST, 2002
8. R. P. Adams, *Identification of Essential Oil Components by Gas Chromatography/Mass Spectrometry*, 4th ed., Allured Publishing Corporation, Carol Stream, IL, USA, 2007
9. F. W. McLafferty, D. B. Stauffer, *Wiley Registry of Mass Spectral Data*, 6th electronic ed. with NIST02, Wiley, New York, USA, 2004
10. D. H. Hochmut, W. A. Koning, D. Joulan, *Massfinder 2.3: Software and Data Bank*, Hamburg, Germany, 2003
11. G. Bernard, E. Gimenez-Arnau, S. Chandra Rastogi, S. Heydorn, J. Duus Johansen, T. Menne, A. Goossens, K. Andersen, J.-P. Lepoittevin, *Arch. Dermatol. Res.* **295** (2003) 229
12. G. Bourgeois, C. Suire, N. Vivas, *Analysis* **27** (1999) 281
13. M. Temina, D. Levitsky, V. M. Dembitsky, *Rec. Nat. Prod.* **4** (2010) 79
14. D. Joulain, R. Tabacchi, *Flavour Fragr. J.* **24** (2009) 105
15. U. Arup, S. Ekman, L. Lindblom, J. Mattsson, *Lichenologist* **25** (1993) 61
16. D. Cansaran Duman, S. Aras, O. Atakol, *J. Appl. Biol. Sci.* **2** (2008) 41
17. F. J. T. Marante, A. G. Castellano, F. E. Rosas, J. Q. Aguiar, J. B. Barrera, *J. Chem. Ecol.* **29** (2003) 2049
18. S. Kirmizigul, O. Koz, N. Boke, *Chem. Nat. Compd*. **43** (2007) 462.

Journal of the Serbian Chemical Society
JSCS-info@shd.org.rs • www.shd.org.rs/JSCS
J. Serb. Chem. Soc. *76* (7) 995–1001 (2011)
JSCS–4178
UDC 546.924+547.313.2+547.466.4+547.213–32:548.7
Original scientific paper

Stereospecific ligands and their complexes. VI. The crystal structure of (*S*,*S*)-ethylenediamine-*N*,*N*'-di-2-propanoic acid hydrochloride, (*S*,*S*)-H_2eddp·HCl≠

VERICA V. GLODJOVIĆ[1], GORDANA P. RADIĆ[1], SNEŽANA M. STANIĆ[2], FRANK W. HEINEMANN[3] and SREĆKO R. TRIFUNOVIĆ[1]*

[1]*Department of Chemistry, Faculty of Science, University of Kragujevac, Radoja Domanovića 12, 34000 Kragujevac,* [2]*Department of Biology, Faculty of Science, University of Kragujevac, Radoja Domanovića 12, 34000 Kragujevac, Serbia and* [3]*Department of Chemistry and Pharmacy, Inorganic Chemistry, Egerlandstrasse 1, D-91058 Erlangen, Germany*

(Received 25 October, revised 23 December 2010)

Abstract: (*S*,*S*)-Ethylenediamine-*N*,*N*'-di-2-propanoic acid hydrochloride, (*S*,*S*)-H_2eddp·HCl, was prepared and its crystal structure determined. The compound was characterized by infrared and ^{1}H- and ^{13}C-NMR spectroscopy. It forms *P*1 in the space group of a triclinic crystal system with a = 5.3902(2) Å, b = 5.8967(2) Å, c = 10.3319(2) Å, α = 99.625(2)°, β = 91.645(2)°, γ = = 109.995(2)° and Z = 1.

Keywords: (*S*,*S*)-ethylenediamine-*N*,*N*'-di-2-propanoate ligand; X-ray crystal structure, ^{1}H-NMR, ^{13}C-NMR spectroscopy.

INTRODUCTION

The discovery of the anticancer activity of cisplatin led investigators to synthesize a number of platinum(II/IV) complexes that could potentially be less toxic to healthy tissues[1–3] and overcome the resistance of some tumors to this type of drug.[4,5] Although platinum-based drugs have high nephrotoxicity and neurotoxicity, cisplatin, carbopatin and oxaliplatin are in clinical use worldwide.[6]

According to these investigations, attention was mainly focused on the preparation, characterization and biological activity of metal complexes with stereospecific edda-type ligands (edda = ethylenediamine-*N*,*N*'-diacetato ion), such as the ethylenediamine-*N*,*N*'-di-(*S*,*S*)-2-propanoate ion and its derivatives.[7–10]

* Corresponding author. E-mail: srecko@kg.ac.rs
doi: 10.2298/JSC101025088G
≠ For Part V see G. P. Vasić, V. V. Glodjović, I. D. Radojević, O. D. Stefanović, Lj. R. Čomić, V. M. Djinović, S. R. Trifunović, *Inorg. Chim. Acta* **363** (2010) 3606.

The preparation of (*S*,*S*)-ethylenediamine-*N*,*N*'-di-2-propanoic acid was published earlier, without spectral characterization.[11] In the present study, the ligand was characterized by infrared, and ^{1}H- and ^{13}C-NMR spectroscopy. In addition, this paper reports single crystal X-ray structure determination of (*S*,*S*)--ethylenediamine-*N*,*N*'-di-2-propanoic acid hydrochloride, crystallized from an HCl–water solution (pH 1.0).

EXPERIMENTAL

Chemistry

All reagents were of grade purity. (*S*,*S*)-Ethylenediamine-*N*,*N*'-di-2-propanoic acid, ((*S*,*S*)-H_2eddp), was prepared using a previously described procedure.[11] On leaving an HCl––water solution of (*S*,*S*)-H_2eddp (pH 1.0) to stand at room temperature for several days, (*S*,*S*)--ethylenediamine-*N*,*N*'-di-2-propanoic acid hydrochloride, (*S*,*S*)-H_2eddp·HCl, crystallized in a form suitable for X-ray crystal structure determination.

Crystal structure determination

A colorless block-shaped single crystal of (*S*,*S*)-H_2eddp·HCl was sealed into a glass capillary and used for the measurement of precise cell constants and intensity data collection. The data were collected at room temperature on a Bruker-Nonius KappaCCD using Mo*K*α radiation (λ = 0.71073 Å, graphite monochromator). The diffraction intensities were corrected for Lorentz and polarization effects. The absorption effects were corrected on a semi-empirical basis using multiple scans (SADABS).[12] The structure was solved by direct methods and refined by full-matrix least-squares calculations against F^2.[13] All non-hydrogen atoms were refined with anisotropic displacement parameters. The position of all hydrogen atoms were derived from a different Fourier synthesis and all hydrogen atoms were refined with individual isotropic displacement parameters. The details of the crystal data, data collection and structure refinement are summarized in Table I.

TABLE I. Crystal data, data collection and structure refinement details for (*S*,*S*)-H_2eddp·HCl

Formula	$C_8H_{17}ClN_2O_4$
Formula weight	240.69
Crystal system	Triclinic
Space group	*P*1
a / Å	5.3902(2)
b / Å	5.8967(2)
c / Å	10.3319(2)
α / °	99.625(2)
β / °	91.645(2)
γ / °	109.995(2)
V / Å^3	302.94(2)
Z	1
Density (calcd.)×10^{-3}, kg m^{-3}	1.319
Abs. coefficient, mm^{-1}	0.314
F(000)	128
No. of collected reflections	8159
No. of independent reflections	2941 (*R*(int) = 0.0277)
No. of observed reflection ($I > 2\sigma(I)$)	2510

TABLE I. Continued

T_{min}, T_{max}	0.917, 1.000
Largest difference peak/hole, eÅ^{-3}	0.215–0.221
Goof (F^2)	1.024
$R1$, $wR2$ ($I>2\sigma(I)$)	0.0318, 0.0670
$R1$, $wR2$ (all data)	0.0438, 0.0704
Absolute structure parameter	0.00(4)

The infrared spectrum was recorded on a Perkin-Elmer FTIR 31725-X spectrophotometer using the KBr pellet technique. The ^{1}H- and ^{13}C-NMR spectra were recorded on Varian Gemini-200 NMR spectrometer using TMS in D_2O as internal reference at 22 °C using a 10 mM solution of the compound. Elemental analyses was realized on a Vario III CHNOS elemental analyzer, Elemental Analysensysteme, GmbH.

All the reagents were obtained commercially and used without further purification.

RESULTS AND DISCUSSION

*Spectroscopic properties of (*S,S*)-H$_2$eddp·HCl*

Yield: 11.3 %; Anal. Calcd. for $C_8H_{17}ClN_2O_4$: C, 39.92; H, 7.12; N, 11.64 %. Found: C, 39.70; H, 7.01; N, 11.50 %. IR (KBr, cm^{-1}): 3419, 3120, 2828, 1728, 1693, 1456, 1350, 1275, 1118, 922, 837, 790, 626. ^{1}H-NMR (200 MHz, D_2O, δ / ppm): 1.53 (6H, *d*, CH_3), 3.54 (4H, *t*, CH_2), 3.67 (2H, *q*, CH). ^{13}C--NMR (200 MHz, D_2O, δ / ppm): 17.4 (CH_3), 44.7 (CH_2), 60.1 (CH), 175.7 (COO^-).

The IR spectrum of the ligand showed specific absorption bands, *i.e.*, δ(C=O) at 1728 cm^{-1} (strong), typical absorption for a protonated acid, δ(C=O) at 1693 cm^{-1} (strong), typical absorption for a deprotonated acid, δ(C–O) 1275 cm^{-1} (medium) and δ(CH_3) at 2828 cm^{-1} (medium).

The NMR spectroscopic measurements gave proof for the constitution of the ligand. In the ^{1}H-NMR spectrum of (*S*,*S*)-H$_2$eddp·HCl, there are the expected signals of CH_2 protons between two diamine nitrogen atoms at 3.54 ppm as a triplet. The signal for the hydrogen atoms of the methyl groups is located at 1.53 ppm as a doublet. The signal for the hydrogen atoms of the CH groups is at 3.67 ppm as a quartet.

^{13}C-NMR spectrum of (*S*,*S*)-H$_2$eddp·HCl exhibits signals for the carbon atom of the COOH groups at 175.7 ppm. The signal of the carbon atom of the methyl groups is at 17.4 ppm. The carbon atoms of the CH_2 groups gave a signal at 44.7 ppm and of the CH groups a signal at 60.1 ppm.

*Description of the structure of (*S,S*)-H$_2$eddp·HCl*

Using the previously described procedure,[11] (*S*,*S*)-ethylenediamine-*N*,*N*'-di--2-propanoic acid, (*S*,*S*)-H$_2$eddp, was isolated as a double zwitter ion at pH 5, with two secondary nitrogen atoms and two carboxylic groups in its structure (Fig. 1). Acidification with aqueous HCl solution to pH 1 resulted in the proto-

nation of one carboxylic group of the (*S*,*S*)-H_2eddp molecule. This protonated hydrochloride form of (*S*,*S*)-H_2eddp yielded good quality crystals suitable for X-ray structure determination.

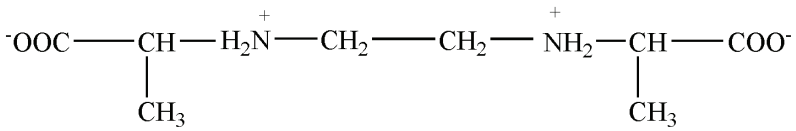

Fig. 1. Structure of (*S*,*S*)-H_2eddp as a zwitter ion.

The molecular structure of (*S*,*S*)-H_2eddp·HCl with the corresponding atomic numbering scheme is shown in Fig. 2. The unit cell packing of the (*S*,*S*)-H_2eddp·HCl molecule is given in Fig. 3, while selected bond distances and bond angles are listed in Table II.

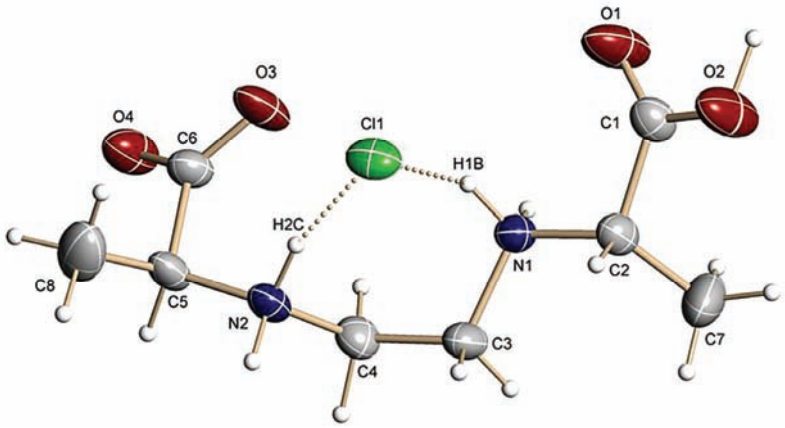

Fig. 2. Molecular structure of (*S*,*S*)-H_2eddp·HCl (50 % probability ellipsoids, H atoms displayed at arbitrary size), the dotted lines indicate the hydrogen bonds between the chloride anion and the (*S*,*S*)-eddp cation.

The structure of (*S*,*S*)-H_2eddp·HCl consists of the protonated (*S*,*S*)-H_2eddp·HCl molecule, as a (*S*,*S*)-H_3eddp$^+$ and a Cl^- counter ion. The difference between the O(1)–C(1) and O(2)–C(1) bond lengths (Table II) suggest the protonation of this carboxylic group, while the O(3)–C(6) and O(4)–C(6) bonds were of almost the same length, suggesting the deprotonated form of this carboxylic group. The elongation of the N(2)–H(2C) bond compared to the N(2)–H(2B) bond is due to the fact that H(2C) is incorporated in a hydrogen bond with Cl^- (Table III). All the other bond distances and angles are in their usual ranges.

The specific shape of the central diamine part of the (*S*,*S*)-H_2eddp·HCl molecule is a consequence of the strong intermolecular N(1)–H(1B)···Cl(1) and N(2)–H(2C)···Cl(1) hydrogen bonds. These N–H···Cl hydrogen bonds, strong inter-

molecular N–H···Cl and O–H···O hydrogen bonds as well as weaker C–H···Cl hydrogen bonds (Table III) determine the packing of the (*S*,*S*)-H_2eddp·HCl molecules in the crystal lattice. The parameters of the more unusual and weaker C–H···Cl hydrogen bonding interactions fall within the typical range observed for this type of hydrogen bond.[14]

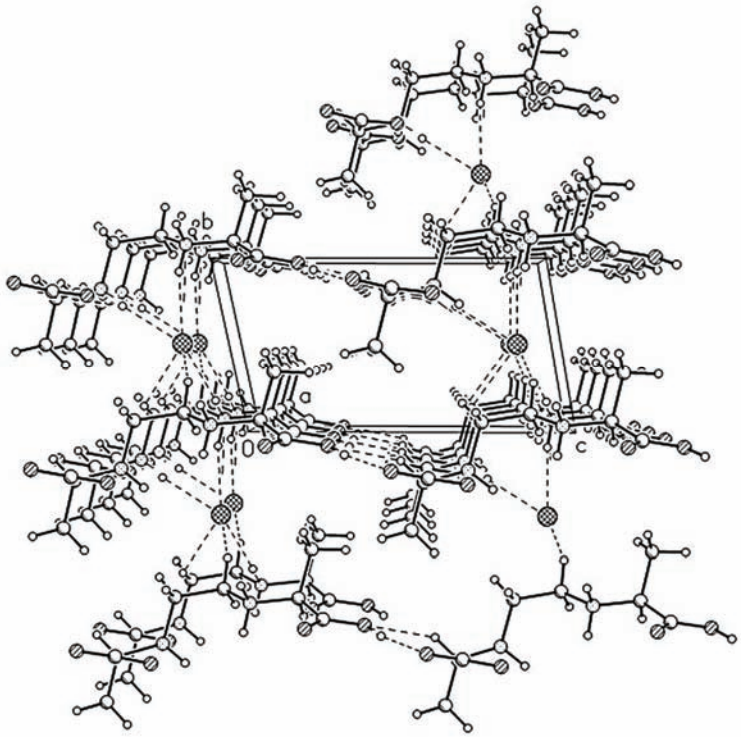

Fig. 3. Packing diagram of (*S*,*S*)-H_2eddp·HCl (view along the crystallographic *a*-axis); dotted lines indicate intramolecular hydrogen bonds.

TABLE II. Selected bond distances and angles for (*S*,*S*)-H_2eddp·HCl (estimated standard deviations (e.s.d.'s) in parentheses)

Bond	Value
Distance, Å	
O(1)–C(1)	1.196(2)
O(2)–C(1)	1.292(2)
O(3)–C(6)	1.244(2)
O(4)–C(6)	1.255(2)
N(1)–C(3)	1.491(2)
N(1)–C(2)	1.493(2)
N(2)–C(5)	1.494(2)
N(2)–C(4)	1.495(2)
C(1)–C(2)	1.519(3)

TABLE II. Continued

Bond	Value
Distance, Å	
C(2)–C(7)	1.527(3)
C(3)–C(4)	1.510(3)
C(5)–C(8)	1.511(3)
C(5)–C(6)	1.540(2)
N(1)–H(1A)	0.930(3)
N(1)–H(1B)	0.930(2)
N(2)–H(2B)	0.94(3)
N(2)–H(2C)	0.98(3)
Angle, °	
C(5)–N(2)–C(4)	113.72(15)
O(1)–C(1)–O(2)	126.11(18)
O(1)–C(1)–C(2)	122.76(16)
O(2)–C(1)–C(2)	111.13(15)
N(1)–C(2)–C(1)	107.63(13)
N(1)–C(2)–C(7)	111.68(17)
C(1)–C(2)–C(7)	111.28(17)
N(1)–C(3)–C(4)	112.56(15)
N(2)–C(4)–C(3)	112.39(16)
N(2)–C(5)–C(8)	108.85(17)
N(2)–C(5)–C(6)	109.53(14)
C(8)–C(5)–C(6)	109.89(18)
O(3)–C(6)–O(4)	125.48(16)
O(3)–C(6)–C(5)	117.41(16)
O(4)–C(6)–C(5)	117.04(15)
C(3)–N(1)–C(2)	113.01(13)

TABLE III. Hydrogen bonds found for (*S*,*S*)-H_2eddp·HCl (e.s.d.'s in parentheses); Symmetry transformations used to generate equivalent atoms: #1: *x*,*y*+1,*z*; #2: *x*+1,*y*,*z*; #3: *x*,*y*,*z*+1; #4: *x*+1,*y*+1,*z*

D–H···A	*d*(D–H) / Å	*d*(H···A) / Å	*d*(D···A) / Å	∠(DHA) / °
N(1)–H(1A)···Cl(1)#1	0.93(3)	2.25(3)	3.1254(15)	158(2)
N(1)–H(1B)···Cl(1)	0.93(2)	2.32(2)	3.0866(15)	138.8(17)
N(2)–H(2B)···O(3)#2	0.94(2)	1.80(2)	2.7239(19)	167(2)
N(2)–H(2C)···Cl(1)	0.98(3)	2.22(3)	3.1659(16)	160(2)
O(2)–H(2D)···O(4)#3	0.97(4)	1.61(4)	2.523(2)	153(4)
C(3)–H(3B)···Cl(1)#4	0.96(3)	2.62(2)	3.321(2)	130(2)
C(4)–H(4B)···Cl(1)#1	0.98(2)	2.88(2)	3.591(2)	130(2)

CONCLUSIONS

(*S*,*S*)-Ethylenediamine-*N*,*N*'-di-2-propanoic acid was unexpectedly crystallized in the form of the monohydrochloride. The crystal form and the crystal packing are determined by strong intermolecular N(1)–H(1B)···Cl(1) and N(2)––H(2C)···Cl(1), as well as by unusually weak C(3)–H(3B)···Cl(1)#4 and C(4)–

–H(4B)···Cl(1)#1 hydrogen bonds. The bond distances and bond angles are within their usual ranges.

Acknowledgement. The authors are grateful for the financial support to the Ministry of Science and Technological Development of the Republic of Serbia (Project No. 172016).

Supplementary data. Crystallographic data (excluding structure factors) for the structures reported in this paper have been deposited with the Cambridge Crystallographic Data Centre as a supplementary publication No. CCDC-795801. Copies of the data can be obtained free of charge on application to The Director, CCDC, 12 Union Road, Cambridge CB2 1EZ, UK (fax: int. code +44(1223)336-033, e-mail: deposit@ccdc.cam.ac.uk).

ИЗВОД

СТЕРЕОСПЕЦИФИЧНИ ЛИГАНДИ И ЊИХОВИ КОМПЛЕКСИ. VI. КРИСТАЛНА СТРУКТУРА (*S*,*S*)-ЕТИЛЕНДИАМИН-*N*,*N*'-ДИ-2-ПРОПАНСКА КИСЕЛИНА-ХИДРОХЛОРИДА, (*S*,*S*)-H_2eddp·HCl

ВЕРИЦА В. ГЛОЂОВИЋ[1], ГОРДАНА П. РАДИЋ[1], СНЕЖАНА СТАНИЋ[2], FRANK W. HEINEMANN[3] и СРЕЋКО Р. ТРИФУНОВИЋ[1]

[1]*Институт за хемију, Природно-математички факултет, Универзитет у Крагујевцу, Радоја Домановића 12, 34000 Крагујевац,* [2]*Институт за биологију, Природно-математички факултет, Универзитет у Крагујевцу, Радоја Домановића 12, 34000 Крагујевац и* [3]*Department of Chemistry and Pharmacy, Inorganic Chemistry, Egerlandstrasse 1, D-91058 Erlangen, Germany*

Синтетисан је тетрадентатни лиганд (*S*,*S*)-етилендиамин-*N*,*N*'-ди-2-пропанска киселина-хидрохлорид и испитивана је његова кристална структура. Наведени лиганд неочекивано кристалише као монохидрохлорид у просторној групи P1 триклиничног кристалног система са димензијама јединичне ћелије a = 5,3902(2) Å, b = 5,8967(2) Å, c = 10,3319(2) Å, α = = 99,625(2)°, β = 91,645(2)°, γ = 109,995(2)° и Z = 1.

(Примљено 25. октобра, ревидирано 23. децембра 2010)

REFERENCES

1. S. D. Schaefer, J. D. Post, L. G. Close, C. G. Wright, *Cancer* **56** (1985) 1934
2. M. P. Goren, R. K. Wright, M. E. Horowitz, *Cancer Chemother. Pharmacol.* **18** (1986) 69
3. D. S. Alberts, J. K. Noel, *Anticancer Drugs* **6** (1995) 369
4. M. Kartalou, J. M. Essigmann, *Mutat. Res.* **478** (2001) 23
5. M. A. Fuertes, M. Alonso, J. M. Pérez, *Chem. Rev*. **103** (2003) 645
6. M. A. Jakupec, M. Galanski, V. B. Arion, C. G. Hartinger, B. K. Keppler, *Dalton Trans*. (2008) 183
7. V. V. Glodjović, M. D. Joksović, S. R. Trifunović, *J. Serb. Chem. Soc.* **70** (2005) 1
8. V. V. Glodjović, S. R. Trifunović, *J. Serb. Chem. Soc.* **73** (2008) 541
9. V. V. Glodjović, F. W. Heinemann, S. R. Trifunović, *J. Chem. Crystallogr*. **38** (2008) 883
10. V. M. Djinović, V. V. Glodjović, G. P. Vasić, V. Trajković, O. Klisurić, S. Stanković, T. J. Sabo, S. R. Trifunović, *Polyhedron* **29** (2010) 1933
11. L. N. Schoenberg, D. W. Cooke, C. F. Liu, *Inorg. Chem.* **7** (1968) 2386
12. *Sadabs 2.06*, Bruker AXS, Inc., Madison WI, USA, 2002
13. *Shelxtl NT 6.12*, Bruker-AXS Inc., Madison, WI, USA, 2002
14. C. B. Aakeröy, T. A. Evans, K. R. Seddon, I. Palinko, *New J. Chem.* (1999) 145.

Journal of the Serbian Chemical Society
JSCS-info@shd.org.rs • www.shd.org.rs/JSCS
J. Serb. Chem. Soc. 76 (7) 1003–1014 (2011)
JSCS–4179
UDC 661.1.001.5:544.02:615.01
Original scientific paper

Estimation of the volume of distribution of some pharmacologically important compounds from their structural descriptors

MOHAMMAD H. FATEMI* and ZAHRA GHORBANNEZHAD

Chemometrics Laboratory, Faculty of Chemistry, University of Mazandaran, Babolsar, Iran

(Received 4 November 2010)

Abstract: Quantitative structure–activity relationship (QSAR) approaches were used to estimate the volume of distribution (V_d) using an artificial neural network (ANN). The data set consisted of the volume of distribution of 129 pharmacologically important compounds, *i.e.*, benzodiazepines, barbiturates, nonsteroidal anti-inflammatory drugs (NSAIDs), tricyclic anti-depressants and some antibiotics, such as betalactams, tetracyclines and quinolones. The descriptors, which were selected by stepwise variable selection methods, were: the Moriguchi octanol–water partition coefficient; the 3D-MoRSE-signal 30, weighted by atomic van der Waals volumes; the fragment-based polar surface area; the d COMMA2 value, weighted by atomic masses; the Geary autocorrelation, weighted by the atomic Sanderson electronegativities; the 3D-MoRSE – signal 02, weighted by atomic masses, and the Geary autocorrelation – lag 5, weighted by the atomic van der Waals volumes. These descriptors were used as inputs for developing multiple linear regressions (MLR) and artificial neural network models as linear and non-linear feature mapping techniques, respectively. The standard errors in the estimation of V_d by the MLR model were: 0.104, 0.103 and 0.076 and for the ANN model: 0.029, 0.087 and 0.082 for the training, internal and external validation test, respectively. The robustness of these models were also evaluated by the leave-5-out cross validation procedure, that gives the statistics Q^2 = 0.72 for the MLR model and Q^2 = 0.82 for the ANN model. Moreover, the results of the *Y*-randomization test revealed that there were no chance correlations among the data matrix. In conclusion, the results of this study indicate the applicability of the estimation of the V_d value of drugs from their structural molecular descriptors. Furthermore, the statistics of the developed models indicate the superiority of the ANN over the MLR model.

Keywords: quantitative structure–activity relationship; molecular descriptor; volume of distribution; artificial neural network.

* Corresponding author. E-mail: mhfatemi@umz.ac.ir
doi: 10.2298/JSC101104091F

INTRODUCTION

The volume of distribution (V_d) of a drug is a major pharmacokinetic property that determines the drug half life and affects the dosing regimen. This parameter is simply a proportionality constant which relates to the amount of drug in the body and/or compartment of the body to its plasma concentration and can represent a measure of the relative partitioning of drug between plasma (the central compartment) and the tissues.[1] The concentration of drug in the plasma or tissues depends on the amount of systemically absorbed drug and the volume in which the drug is distributed as well as the clearance (*Cl*). The clearance of a drug is the volume of plasma from which the drug is completely removed per unit time. The amount of eliminated drug depends on the concentration of the drug in the blood. The fraction of the drug in the body eliminated per unit time is showed by the elimination constant (k_{el}). The volume of distribution is calculated from these two parameters using the following equation:

$$V_d = Cl / k_{el} \quad (1)$$

The volume of distribution in humans is traditionally estimated from *in vivo* data from preclinical animals with appropriate scaling to man, which is a slow, labor intensive and costly process.[2] Moreover, low rates of throughput provide detailed and informative data at the expense of animal usage.[3] Therefore *in silico* estimation methods, such as quantitative structure–activity relationships (QSAR) can be used as an alternative to animal scaling to predict V_d.[4,5] A quantitative structure activity relationship model describes a mathematical relationship between a structural attribute (s) and the activity of a set of chemicals. The use of such mathematical relationships to predict the target property of interest for a variety of chemicals prior to or *in lieu* of expensive and labor-intensive experimental measurements has naturally been very enticing. The potential promise of using QSAR models for the screening of chemical databases or virtual libraries before their synthesis appears equally attractive to chemical manufacturers, pharmaceutical companies and government agencies, particularly in times of shrinking resources.[6] There are some reports concerning the prediction of the volume of distribution of chemicals.[7,8] For example, Hirono and coworkers studied the correlation of chemical structures with the volume of distribution of some aromatic, non-aromatic and hetero-aromatics medicines, to construct an expert system for predicting the pharmacokinetic properties of organic chemicals using fuzzy adaptive least-squares.[7] Artificial neural networks for the prediction of the human pharmacokinetic parameters of some drugs using a combination of physico-chemical properties and animal pharmacokinetic parameters were used by Ritschel *et al.*[9] Protein binding, partition coefficients, dissociation constants, total clearance (Cl_{tot}) and volume of distribution (V_d) in rat and dog species of 41 drugs were evaluated for the prediction of human total clearance and volume of

distribution by these researchers. Their results indicated that drugs with partition (log P) < 1.17 showed predictability of 63.41 % for Cl_{tot} and 48.78 % for V_d, while drugs with low protein binding (approximately 20 %) showed a predictability of 19.51 % for Cl_{tot} and 41.46 % for V_d. Comparison of these results with an *in vitro* estimation showed no bias in the prediction of either clearance (p < 0.2) or volume of distribution (p < 0.5). In another study, a quantitative structure–pharmacokinetic relationship model to predict some pharmacokinetic properties of a cephalosporins series was developed by J. V Turner *et al.*[10] Moreover, F. Lombardo and co-workers published some reports about the prediction of human volume of distribution values for neutral and basic drugs using physico–chemical measurements and protein binding data.[11] Finally, Ghafourian and co-workers reported a QSAR model for the prediction of V_d of some acidic and basic drugs using a universal 7-parameter MLR model.[4] In their model, the obtained correlation coefficient between the observed and predicted V_d values for the test set was R^2_{pred} = 0.699. They concluded that this QSAR model was able to predict the volume of distribution of drugs belonging to different chemical classes with a prediction error similar to that of other more complicated prediction methods, including the commonly practiced interspecies scaling. In the present work, this model was improved by using an ANN as a nonlinear feature mapping technique.

METHODOLOGY

Data set

The experimental values of distribution for 129 drugs were extracted from the literature,[4] and reported as log V_d, they are listed in Table I-S (Supplementary material). These drugs are benzodiazepines, barbiturates, NSAIDs, tricyclic anti-depressants and some antibiotics, such as betalactams, tetracyclines and quinolones. The distribution of the experimental log V_d values of data set is shown in Fig. 1.

The data set was randomly divided into training, internal and external test sets that had 103, 13 and 13 members, respectively. The training set was used to develop the model, the internal test set was used to prevent over training and the external test set was used to evaluate the predictive ability of the obtained model.

Descriptor generation and screening

One important step in obtaining a QSAR model is the numerical representation of the structural features of molecules (molecular descriptors). The molecular descriptors used to search for the best model of log V_d were calculated by the Dragon program[12] based on the minimum energy molecular geometries that were optimized by the Hyperchem package (version 7.0) (HyperChem 2002, release 7.0) based on the AM1 semi-empirical method.[13] After calculation of the molecular descriptors, those that were constant or near constant for all molecules were eliminated and pairs of variables with a correlation coefficient greater than 0.90 were classified as inter-correlated and one of each correlated pair was deleted. Then, the stepwise multiple linear regression variable subset selection method[14] was used for the selection of the most relevant descriptors from the pool of the remaining descriptors. These descriptors were used as inputs for the construction of the ANN and MLR models.

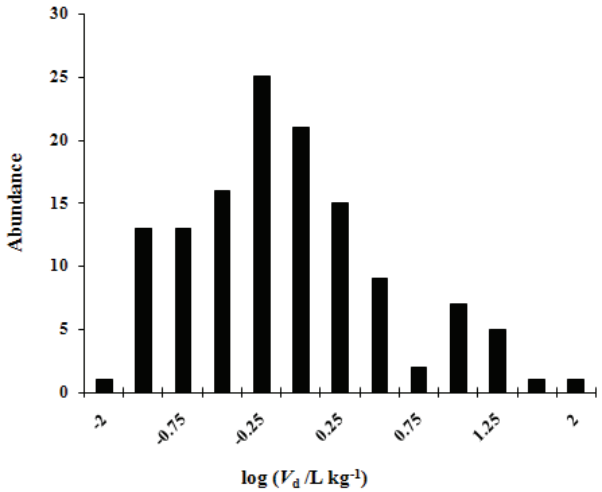

Fig. 1. The distribution of the experimental log V_d values.

Molecular diversity analysis

Diversity analysis was performed on the data set to ensure that the structures of the training or test sets can represent those of the whole ones.[15] A database of n compounds generated from m highly correlated chemical descriptors $\{x_j\}_{j=1}^{m}$ was considered. Each compound, X_i, is represented as a vector of:

$$X_i = (x_{i1}, x_{i2}, x_{i3}, \ldots, x_{im}) \quad \text{for} \quad i = 1,2,\mathrm{L},n \tag{2}$$

In the above equation, $x_{i,j}$ denotes the value of descriptor j of compound X_i. The collective database $\left(X = \{X_i\}_{i=1}^{N}\right)$ is represented by an $n \times m$ matrix (X) as follows:

$$X = (x_1, x_2, \mathrm{L}, X_N)^T = \begin{bmatrix} x_{11} & x_{12} & \cdots & x_{1\mathrm{m}} \\ x_{21} & x_{22} & \cdots & x_{2\mathrm{m}} \\ \vdots & \vdots & \ddots & \cdots \\ x_{\mathrm{m}1} & x_{\mathrm{m}2} & \cdots & x_{\mathrm{nm}} \end{bmatrix} \tag{3}$$

Here the superscript T denotes the vector/matrix transpose. A distance score for two different compounds X_i and X_j can be measured by the Euclidean distance norm d_{ij}, based on the compound descriptors:

$$d_{ij} = \|X_i - X_j\| = \sqrt{\sum_{k=1}^{m} (x_{ik} - x_{jk})^2} \tag{4}$$

The relative mean distances $(\bar{d}_i)$ of one sample to the remaining ones were computed as follow:

$$\bar{d}_i = \frac{\sum_{j=1}^{n} d_{ij}}{n-1} \qquad i = 1,2,\ldots,n \tag{5}$$

Then the relative mean distances were normalized within the interval (0,1). The values of the relative mean distances of samples *versus* the experimental log V_d are plotted in Fig. 2. The results of this test illustrate the good distribution of the test sets among the whole data set. The training set with a broad representation of the chemistry space was adequate to ensure models stability and the diversity of the test set can prove the predictive capability of the model.

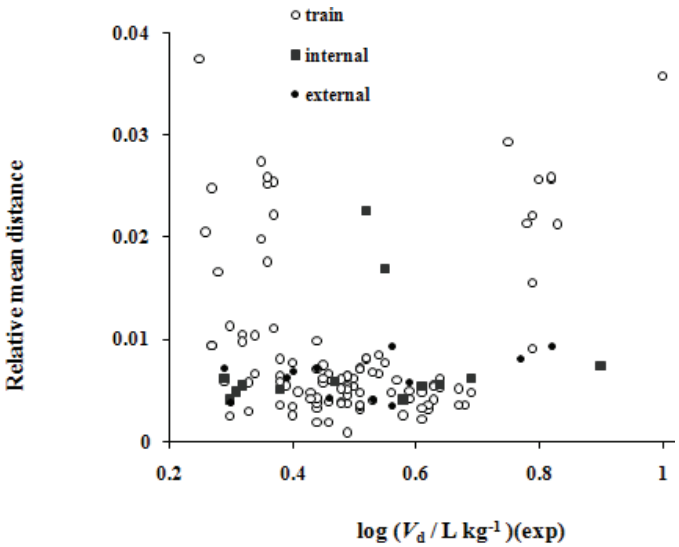

Fig. 2. The results of the diversity analysis (the relative mean distance was calculated from Eq. (5)).

Nonlinear modeling

In order to examine any non-linear relationships between selected molecular descriptors and the volume of distribution, an artificial neural network was used. A detailed description of theory behind artificial neural networks has been adequately described elsewhere.[16–19] In addition, some relevant principles of ANNs were reported in previous papers.[20–22] ANNs are parallel computational devices consisting of groups of highly inter-connected processing elements called neurons. Neurons in traditional neural networks are arranged in a series of layers. The first layer is termed the input layer; each neuron in this layer receives information from the exterior, corresponding to the independent variables (molecular descriptors). The last layer is the output layer, and its neurons handle the output from the network, which is log V_d in this study. The layers of neurons between the input and output layers are called hidden layers. The number of neurons in these layers is optimized during model development.[23] In the first step of developing an ANN model, the program of a feed-forward neural network, which was trained by a back-propagation algorithm, was written in Matlab (ver. 7.4.0). This network had seven nodes in the input layer and one node in the output layer. The initial weights were selected from a uniform distribution of numbers that ranged between –0.3 and 0.3. The initial bias values were set to be one. These values were optimized during the network training. The value of each input was divided into its mean value to bring them into the dynamic range of the sigmoid transfer function of an ANN. Before training, the network parameters were optimized. These parameters were: number of nodes in the hidden layer, weights and biases learning rates and the momentum. Then the optimized network was trained using a training set for adjustment of the values of the weights and biases.

RESULTS AND DISCUSSION

The descriptors which were selected by the stepwise variable selection method are: the Moriguchi octanol–water partition coefficient (*M*log *P*); the 3D-

-MoRSE – signal 30, weighted by atomic van der Waals volumes (Mor30v); the fragment-based polar surface area (PSA); the d COMMA2 value, weighted by atomic masses (DISPm); the Geary autocorrelation, weighted by the atomic Sanderson electronegativities (GATS2e); the 3D-MoRSE – signal 02, weighted by atomic masses (Mor02m) and the Geary autocorrelation – lag 5, weighted by atomic van der Waals volumes (GATS5v). These descriptors encode different aspects of the molecular structure and were applied to construct the MLR and ANN models. Detailed explanations about these descriptors can be found in the Handbook of Molecular Descriptors.[12] Table I represents the correlation between these descriptors. As can be seen from this table, there were no high correlations between these descriptors.

TABLE I. Correlation matrix between the selected descriptors

	*M*log *P*	Mor30v	PSA	DISPm	GATS2e	GATS5v	Mor02m
Mlog *P*	1	0.174	–0.558	0.25	0.232	0.222	–0.306
Mor30v		1	–0.216	0.026	0.264	0.131	0.182
PSA			1	–0.248	–0.387	–0.087	–0.145
DISPm				1	0.038	–0.039	–0.145
GATS2e					1	0.088	0.037
GATS5v						1	–0.123
Mor02m							1

In the case of the MLR models, good correlations with the experimental volume of distribution were selected based on the correlation coefficient (*R*), the Fisher criterion (*F*) and the standard error of regression (*SE*) of the models. The specifications of the selected MLR model are shown in Table II. The standard error (*SE*), average error (*AE*) and average absolute error (*AAE*) in the calculation of log V_d by this model for the training set are: *SE* = 0.420, *AE* = 0.003 and *AAE* = = 0.310; for internal test set, they are: *SE* = 0.430, *AE* = 0.066 *AAE* = 0.342 and for external test set, are: *SE* = 0.085, *AE* = 0.00, *AAE* = 0.082.

Moreover, an artificial neural network was applied to further examine any non-linear relations between selected molecular descriptors and the volume of distribution. Before training the network, the parameters of the number of nodes in the hidden layer, weights and biases learning rates and momentum values were optimized. The architecture and the specification of the optimized neural network are given in Table III. After optimization, the network was trained by using the training set for the adjustment of the values of the weights and biases. To maintain the predictive power of the network at a desirable level, training was stopped when the value of error for the internal test set started to increase. Since the test error is not a good estimate of the generation error, the prediction potential of the model was evaluated on a third set of data, named the external test set. Then the trained network was applied to calculate the values of V_d for the

internal and external test sets. The statistics of this model in the estimation of V_d were: *SE* = 0.119, *AE* = 0.00 and *AAE* = 0.082 for the training set; *SE* = 0.439, *AE* = 0.100 and *AAE* = 0.363 for the internal test set and *SE* = 0.078, *AE* = 0.005 and *AAE* = 0.060, for the external test set.

TABLE II. Specification of the MLR model

Descriptors	Notation	Coefficient	*SE*	*t*-value	*p*-value
Moriguchi octanol–water partition coefficient	*M*log *P*	0.298	0.072	4.131	0.000
3D-MoRSE- signal 30, weighted by atomic van der Waals volumes	*Mor30v*	–0.273	0.069	–3.982	0.000
Fragment-based polar surface area	PSA	–0.212	0.067	–3.161	0.002
d COMMA2 value, weighted by atomic masses	*DISPm*	0.154	0.057	2.718	0.008
Geary autocorrelation, weighted by atomic Sanderson electronegativities	GATS2e	0.260	0.067	3.884	0.000
Geary autocorrelation – lag 5, weighted by atomic van der Waals volumes	*GATS5v*	0.169	0.081	2.095	0.039
3D-MoRSE - signal 02, weighted by atomic masses	*Mor02m*	0.150	0.066	2.260	0.026
Constant	–	0.190	0.087	2.186	0.031

TABLE III. Architecture and specifications of the ANN model

Transfer function	Sigmoid
No. of hidden layer nodes	8
Weight learning rate	0.8
Bias learning rate	0.7
Momentum	0.2
No. of input layer nodes	7
No. of output layer nodes	1

In order to evaluate the robustness of the developed models, cross-validation was employed.[24] The obtained statistical parameters of the leave-5-out cross-validation test were: Q^2 = 0.72 for the MLR model and Q^2 = 0.82 for the ANN model. In addition, the *Y*-scrambling procedure was performed to investigate any chance correlations between V_d and selected molecular descriptors.[25] The obtained mean value of R^2 after a 30-time scrambling of the data set and modeling was 0.09, which indicates that there were no chance correlations in the data matrix.

Plots of the ANN calculated *versus* the experimental values of log V_d for the training, internal and external test sets are shown in Fig. 3, which represent good correlations between these parameter. In addition, the residuals of the calculated V_d values are plotted against their experimental values in Fig. 4. Random propagation of the residuals on both sides of the zero line indicates that no systematic error exists in the developed ANN model. In order to compute the relative importance of each input variable on the output of the neural network,[26] sensitivity

analysis was used. This test was performed based on the sequential removal of variables by zeroing the specific connection weights for an input variable in the first layer of the established ANN model. According to this method, the differences between the root-mean-square error (*RMSE*) of the complete prediction of the network and the *RMSE* obtained when the i^{th} variable was excluded from the trained network ($RMSE_i$) were calculated and are shown as $Rmdiff_i$ (Eq. (6)).

$$Rmdiff_i = RMSE_i - RMS \quad (6)$$

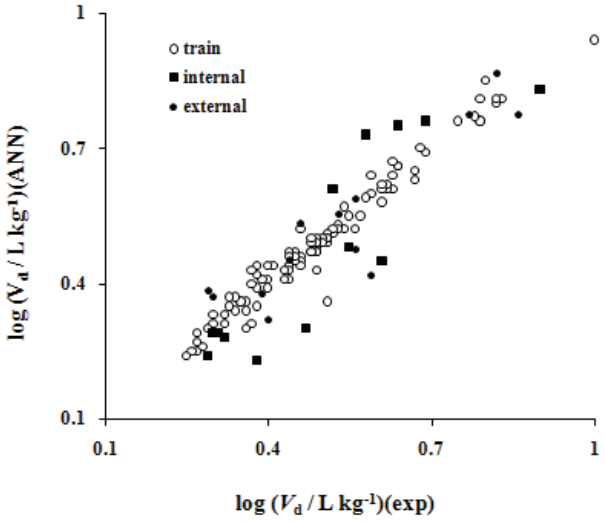

Fig. 3. The plot of the ANN calculated *versus* the experimental values of log V_d.

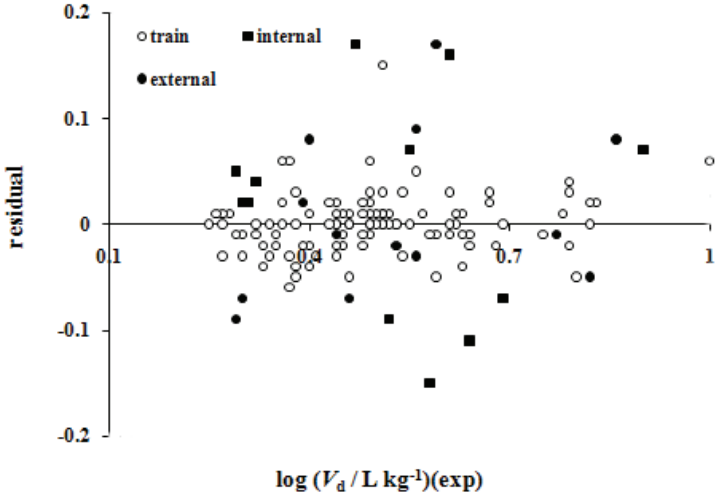

Fig. 4. The plot of the residuals (log $V_{d,ANN}$ – log $V_{d,exp}$) *versus* the experimental values of log V_d.

It is obvious that the most important variable is the one that leads to the highest value of $Rmdiff_i$. The values of $Rmdiff_i$ for the ANN model were calculated and are plotted in Fig. 5. As can be seen in this figure, the order of importance of the selected molecular descriptors was; *M*log *P* > *Mor30v* > GATS2e > *GATS5v* > PSA ≈ *DISPm*> *Mor02m*.

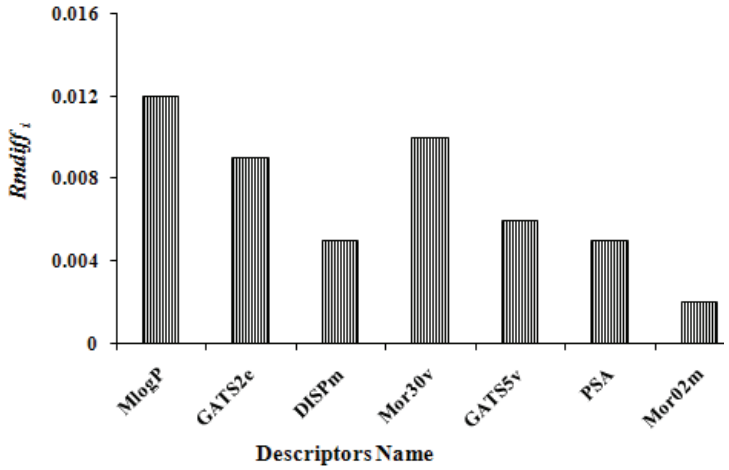

Fig. 5. The results of the sensitivity analysis ($Rmdiff_i$ was calculated from Eq. (6)).

According to this analysis, the most important descriptor in the model was *M*log *P*, which is a popular and traditional descriptor used in many QSAR models.[12] *M*log *P* describes the solute lipophilicity, which is one of the most important properties of any compound and indicates the ability of a solute to penetrate to lipid-rich zones from aqueous solutions. This is a very important feature of any drug that is administrated orally and is supposed to pass the gastrointestinal epithelium. Another variable is DISPm, which is a molecular geometry descriptor and was obtained using the Dragon software and describes the conformational features of the molecules. Low values of DISPm are expected for more rigid molecules that exhibit higher passivity due to the absence of long and flexible substituents and the presence of unsaturated bonds. The molecular polar surface area (PSA) encodes the sum of the surface belonging to polar atoms in a molecule; it is a descriptor that was affected on molecular transportation through membranes and therefore, allows an estimation of the apparent volume of distribution in the body. Another of the descriptors is the Geary autocorrelation-lag 2 weighted by atomic Sanderson electronegativities, which belongs to the GATSd family of 2D autocorrelation descriptors.[27,28] Generally, the 2D-autocorrelation descriptors explain how the values of certain functions, at intervals equal to the lag d, are correlated. In these descriptors, the lag is the topological distance and the atomic properties are the functions correlated. These descriptors can be ob-

tained by summing the products of certain properties of two atoms, which are located at a given topological distance or spatial lag. In general, they describe how the considered property is distributed along the topological structure. The value of GATS2e shows the dispersion of electronegative atoms at a topological distance equal to 2 bonds in a molecule and also the value of GATS5v shows the dispersion of volume atoms at a topological distance equal to 5 bonds in a molecule. The remaining descriptors are *Mor02m* and Mor30v. These descriptors are defined based on the idea of obtaining information from the 3D atomic coordinates by the transform used in electron diffraction studies for preparing theoretical scattering curves.[29] A generalized scattering function, called the molecular transform, can be used as the functional basis for deriving from a known molecular structure, the specific analytic relationship of both X-ray and electron diffraction. These descriptors can encode the mass-distribution around the center of a molecule. In general, the descriptors that appeared in these QSAR models can encode different electronic, steric and lipophilic aspects of the molecules, which can affect the volume of distribution of drugs.

The fold errors (*FE*) in the prediction for the obtained QSAR models were calculated from the following equation:

$$FE = \text{antilog}\,(|\log V_{d,obs} - \log V_{d,pred}|) \quad (7)$$

The calculated mean fold errors (*MFE*) for the training, internal and external test sets were 1.23, 2.5 and 1.92, respectively for the ANN model. In addition, as mentioned earlier, Ghafourian *et al*. used QSAR approaches on the same data set and obtained the statistics *MFE* = 2.11 and R^2 = 0.699 in a leave-32-out cross validation test for their best 7-parameter model (on elimination of 4 molecules as outlier). The results of the same test on the herein presented ANN model gives the statistics of *MFE* = 1.17 and R^2 = 0.850, without any elimination of outlier molecules. Comparisons between these results indicate the superiority of the present model over their model.

CONCLUSIONS

The results of this study indicate that it was possible to estimate the volume of distribution of drugs from their theoretically derived molecular descriptors. Since these descriptors encode electronic and topological features of molecules, it was concluded that lipophilicity and steric interactions affect the V_d of drugs. Moreover, the superiority of the ANN over the MLR model revealed that there are some nonlinear relationships between the volume of distribution and selected molecular descriptors.

SUPPLEMENTARY MATERIAL

Data set and the corresponding observed values as well as MLR and ANN calculated values of V_d are available electronically at http://www.shd.org.rs/JSCS/, or from the corresponding author on request.

ИЗВОД

ПРОЦЕНА ЗАПРЕМИНСКЕ РАСПОДЕЛЕ НЕКИХ ФАРМАКОЛОШКИ ВАЖНИХ ЈЕДИЊЕЊА НА ОСНОВУ ЊИХОВИХ СТРУКТУРНИХ ДЕСКРИПТОРА

MOHAMMAD H. FATEMI и ZAHRA GHORBANNEZHAD

Faculty of Chemistry, University of Mazandaran, Babolsar, Iran

Применом вештачких неуралних мрежа (ANN) нађене су квантитативне релације између структуре и активности (QSAR) за процену запреминске расподеле (V_d). Подаци се састоје из запреминске расподеле за 129 фармаколошки важних једињења: бензодиазепина, барбитурата, NSAID-а, трицикличних антидепресива и неких антибиотика, као што су бета--лактами, тетрациклини и хинолони. Дескриптори су Moriguchi-јев коефицијент расподеле октанол–вода, 3D-MoRSE сигнал, величина поларне површине засноване на фрагментима, вредности d COMMA2, Geary-јева аутокорелација, 3D-MoRSE сигнал 02, и др. Ови дескриптори су употребљени као улазни подаци за добијање мултилинеарних регресија (MLR) и за моделе вештачких неуралних мрежа. Стандардне грешке код процене V_d помоћу MLR модела су: 0,104; 0,103 и 0,076, док су за ANN моделе: 0,029; 0,087 и 0,082 за тренинг, интерни и екстерни валидациони тест. Робустност ових модела је такође процењена, што даје Q^2 = 0,72 за MLR модел и Q^2 = 0,82 за ANN модел. Статистичка анализа указује на то да је ANN модел бољи од MLR модела.

(Примљено 4. новембра 2010)

REFERENCES

1. F. Lombardo, R. S. Obach, Y. M. Shalaeva, F. Gao, *J. Med. Chem*. **45** (2002) 2867
2. D. A. Smith, H. Van de Waterbeemd, D. K. Walker, *Pharmacokinetics and metabolism in drug design*, Wiley-VCH, Weinheim, Germany, 2001, p. 123
3. S. H. Kim, W. B. Kim, M. G. Lee, *J. Chromatogr. B* **688** (1997) 95
4. T. Ghafourian, M. Barzegar-Jalali, S. Dastmalchi, T. Khavari, N. Hakimiha, A. Nokhodchi, *Int. J. Pharm.* **319** (2006) 82
5. T. Ghafourian, M. Barzegar-Jalali, N. Hakimiha, M. T. D. Cronin. *J. Pharm. Pharmacol*. **56** (2004) 339
6. L. Douali1, D. Villemin, A. Zyad, D. Cherqaoui1. *Mol. Divers.* **8** (2004) 1
7. S. Hironos, I. Nakagome, H. Hirano, F. Yoshii, I. Moriguchi, *Biol. Pharm. Bull*. **17** (1994) 686
8. V. Joseph, D. J. Turner, D. J Maddalena, S. A. Cutler, *J. Pharm. Sci.* **92**(2002) 552
9. W. A. Ritschel, R. Akileswaran, A. S. Hussain, *Methods Findings Exp. Clin. Pharmacol.* **17** (1995) 629
10. J. V. Turner, D. J. Maddalena, D. J. Cutler, K. S. Agatonovic. *J. Pharm. Sci.* **92** (2002) 552
11. F. Lombardo, R. S. Obach, Y. M. Shalaeva, F. Gao, *J. Med. Chem*. **47** (2004) 1242
12. R. Todeschini, V. Consonni, *Handbook of Molecular Descriptors*, Wiley-VCH, Weinheim, Germany, 2000
13. M. J. S Dewar, E. G. Zoebisch, E. F. Healy, J. J. P Stewart, *J. Am. Chem. Soc*. **107** (1985) 3898
14. D. L. Massart, B. G. M. Vandeginste, L. M. G. Buydens, S. Dejong, P. J. Lewi, J. Smeyers-Verbeke, *Handbook of Chemometrics and Qualimetrics*: *part A*, Elsevier, Amsterdam, The Netherlands, 1977

15. A. G. Maldonado, J. P. Doucet, M. Petitjean, B. T. Fan, *Mol. Divers.* **10** (2006) 39
16. J. Zupan, J. Gasteiger, *Neural Networks in Chemistry and Drug Design*, Wiley–VCH, Weinheim, Germany, 1999
17. N. K. Bose, P. Liang, *Neural Network, Fundamentals*, McGraw-Hill, New York, 1996
18. M. T. Beal, H. B. Hagan, M. Demuth, *Neural Network Design*, PWS, Boston, MA, USA, 1996
19. J. Zupan, J. Gasteiger, *Neural Networks for Chemists: an Introduction*, VCH, Weinheim, Germany, 1993
20. M. H. Fatemi, *J. Chromatogr. A* **1002** (2003) 221
21. M. H. Fatemi, *J. Chromatogr. A* **955** (2002) 273
22. M. Jalali-Heravi, M. H. Fatemi. *J. Chromatogr. A.* **915** (2001) 177
23. B. J. Wythoff, *Intell. Lab. Syst.* **18** (1993)115
24. D.W. Osten. *J. Chemom.* **2** (1988) 39
25. S. Wold, L. Eriksson, *Chemometrics methods in molecular design*, VCH, Weinheim, Germany, 1995.
26. M. H. Fatemi, M. Jalali-Heravi, E. Konuze, *Anal. Chim. Acta* **486** (2003) 101
27. S. Fu, C. A. Lucy, *Anal. Chem*. **70** (1998) 173
28. S. Fu, C. A. Lucy, *Analyst* **123** (1998) 1487
29. L.J. Soltzberg, C. L. Wilkins, *J. Am. Chem. Soc*. **99** (1997)439.

Journal of the Serbian Chemical Society
JSCS@tmf.bg.ac.rs • www.shd.org.rs/JSCS
J. Serb. Chem. Soc. 76 (7) S7–S10 (2011) *Supplementary material*

SUPPLEMENTARY MATERIAL TO

Estimation of the volume of distribution of some pharmacologically important compounds from their structural descriptors

MOHAMMAD H. FATEMI* and ZAHRA GHORBANNEZHAD

Chemometrics Laboratory, Faculty of Chemistry, University of Mazandaran, Babolsar, Iran

J. Serb. Chem. Soc. 76 (7) (2011) 1005–1016

TABLE I-S. Data set and the corresponding observed values as well as MLR and ANN calculated values of V_d (int and ext denote the internal and external test set, respectively)

No	Name	log $(V_d)_{EXP}$	log $(V_d)_{MLR}$	Deviation	log $(V_d)_{ANN}$	Deviation
1	Acetanilide	–0.797	–0.096	–0.701	–0.663	–0.134
2	Alprazolam	–0.064	0.333	–0.397	0.034	–0.098
3	Amitriptyline	1.025	1.362	–0. 337	1.079	–0.053
4	Amobarbital	0.021	–0.489	0.510	–0.027	0.048
5	Amoxicillin	–0.072	–0.578	0.506	–0.096	0.024
6	Amphetamine$_{int}$	0.592	0.520	0.072	1.038	–0.446
7	Ampicillin	–0.214	–0.448	0.235	–0.230	0.016
8	Bromazepam	0.053	0.269	–0.215	0.038	0.016
9	Bupivacaine	0.001	0.625	–0.624	–0.043	0.044
10	Bupropion	1.208	0.645	0.562	1.071	0.137
11	Butorphanol	0.697	0.297	0.400	0.564	0.133
12	Caffeine	–0.259	–0.153	–0.106	–0.327	0.068
13	Carbamazepine	0.078	–0.327	0.405	0.034	0.044
14	Carbenicillin	–0.603	–0.643	0.040	–0.525	–0.077
15	Cefazolin $_{ext}$	–0.769	–0.056	–0.713	–0.497	–0.272
16	Cephalexin	–0.469	–0.501	0.032	–0.582	0.113
17	Cephaloridine	–0.639	–0.201	–0.438	–0.623	–0.017
18	Cephalothin	–0.376	–0.355	–0.021	–0.432	0.056
19	Cephradine	–0.356	–0.327	–0.029	–0.218	–0.138
20	Chloral hydrate$_{ext}$	–0.222	–0.363	0.141	–0.161	–0.061
21	Chloramphenicol	–0.242	0.151	–0.393	–0.238	–0.004
22	Chlordiazepoxide	–0.445	0.171	–0.616	–0.238	–0.207
23	Chloroquine	2.050	0.982	1.068	1.816	0.234
24	Chlorphentermine	0.398	0.678	–0.280	0.609	–0.211
25	Chlortetracycline	0.207	–0.295	0.502	0.098	0.109
26	Clindamycin	0.001	–0.250	0.251	–0.007	0.008

* Corresponding author. E-mail: mhfatemi@umz.ac.ir

TABLE I-S. Continued

No	Name	log $(V_d)_{EXP}$	log $(V_d)_{MLR}$	Deviation	log $(V_d)_{ANN}$	Deviation
27	Clobazam	0.049	–0.096	0.145	0.005	0.044
28	Clomipramine	1.232	1.042	0.190	1.423	–0.191
29	Clonazepam	0.495	–0.100	0.595	0.467	0.028
30	Clorazepate	–0.036	–0.222	0.186	0.001	–0.037
31	Cloxacillin	–0.826	–0.299	–0.527	–0.789	–0.037
32	Cyclacillin	–0.396	–0.473	0.077	–0.238	–0.158
33	Demeclocycline$_{ext}$	0.252	0.265	–0.013	0.378	–0.126
34	Desipramine$_{ext}$	1.479	0.986	0.493	1.059	0.420
35	Diazepam$_{ext}$	0.284	0.135	0.149	–0.068	0.352
36	Dicloxacillin	–0.886	–0.493	–0.393	–0.935	0.048
37	Doxepine$_{ext}$	1.102	1.172	–0.070	1.059	0.044
38	Doxycycline$_{ext}$	–0.129	0.054	–0.183	0.163	–0.292
39	Ethambutol	0.126	0.058	0.068	0.127	–0.001
40	Ethclorvynol	0.398	0.508	–0.110	0.427	–0.029
41	Ethosuximide	–0.173	–0.558	0.384	–0.104	–0.069
42	Etidocaine	0.300	0.556	–0.256	0.240	0.060
43	Fentanyl 3.60e	0.556	0.188	0.368	0.714	–0.159
44	Flunitrazepam	0.600	–0.116	0.716	0.670	–0.070
45	Fluoxetine$_{int}$	1.649	0.738	0.911	1.362	0.287
46	Gentamycin	–0.554	–0.412	–0.142	–0.615	0.060
47	Glutethimide	0.495	–0.068	0.562	0.508	–0.013
48	Griseofulvin	0.240	0.175	0.064	0.228	0.012
49	Haloperidol	1.200	0.609	0.591	1.302	–0.102
50	Hetacillin	–0.396	–0.493	0.097	–0.331	–0.065
51	Ibuprofen	–1.000	–0.169	–0.831	–0.991	–0.008
52	Imipramine	1.216	10.156	0.060	1.071	0.145
53	Indomethacin	–0.024	0.192	–0.215	–0.007	–0.017
54	Isoniazid	–0.194	–0.250	0.056	–0.153	–0.041
55	Kanamycin$_{int}$	–0.720	–0.197	–0.523	–0.874	0.154
56	Ketamine	0.600	0.313	0.287	0.662	–0.061
57	Lidocaine$_{ext}$	0.151	0.309	–0.159	0.244	–0.094
58	Lincomycin	–0.481	–1.048	0.567	–0.380	–0.102
59	Lorazepam	0.078	–0.043	0.121	0.078	–0.001
60	Maprotiline$_{ext}$	1.321	0.860	0.461	1.516	–0.195
61	Meprobamate	–0.153	0.054	–0.207	–0.173	0.020
62	Meptazinol	0.738	0.544	0.194	0.819	–0.082
63	Methacycline	–0.011	–0.282	0.271	–0.092	0.081
64	Methadone	0.531	0.212	0.319	0.483	0.048
65	Methaqualone$_{int}$	0.778	0.933	–0.155	1.059	–0.280
66	Meticillin	–0.445	–0.509	0.064	–0.424	–0.021
67	Metoclopramide	0.479	0.094	0.384	0.467	0.012
68	Midazolam$_{int}$	0.114	0.439	–0.325	0.471	–0.357
69	Minocycline	–0.125	–0.072	–0.053	–0.124	0.000
70	Moclobemide	0.110	0.528	–0.418	0.127	–0.017
71	Morphine	0.458	0.439	0.020	0.341	0.117
72	Nafcillin	–0.538	–0.473	–0.065	–0.534	–0.004

TABLE I-S. Continued

No	Name	log $(V_d)_{EXP}$	log $(V_d)_{MLR}$	Deviation	log $(V_d)_{ANN}$	Deviation
73	Naloxone	0.479	0.678	–0.199	0.528	–0.049
74	Neomycin(a)	–2.000	–0.343	–1.657	–1.749	–0.251
75	Nitrazepam$_{int}$	0.349	–0.108	0.457	0.973	–0.624
76	Nitrofurantoin	–0.493	–0.258	–0.235	–0.254	–0.239
77	Nortriptyline	1.313	1.289	0.023	1.249	0.064
78	Oxacillin	–0.538	–0.242	–0.296	–0.785	0.247
79	Oxazepam	–0.003	0.155	–0.158	–0.254	0.251
80	Oxyphenbutazone	–0.959	–0.315	–0.644	–0.906	–0.053
81	Oxytetracycline	0.276	–0.080	0.356	0.090	0.186
82	Paracetamol	0.082	–0.096	0.178	–0.019	0.101
83	Paroxetine	1.366	0.629	0.736	1.281	0.084
84	PAS	–0.639	–0.339	–0.300	–0.505	–0.134
85	Penicillin G	–0.169	–0.566	0.397	–0.189	0.020
86	Penicillin V	–0.153	–0.659	0.506	–0.201	0.048
87	Pethidine	0.701	0.107	0.595	0.625	0.076
88	Phenacetin	0.118	0.269	–0.150	0.082	0.036
89	Phenazone	–0.003	–0.197	0.194	–0.080	0.076
90	Phencyclidine	0.778	0.256	0.522	0.791	–0.013
91	Phenethicillin K	–0.457	–0.469	0.012	–0.286	–0.171
92	Phenobarbital$_{int}$	–0.097	–0.380	0.283	–0.797	0.700
93	Phenylbutazone$_{ext}$	–0.826	–0.274	–0.551	–0.444	–0.381
94	Phenytoin	–0.222	0.143	–0.365	–0.153	–0.069
95	Prazepam	0.175	0.204	–0.029	0.297	–0.122
96	Primidone	–0.003	–0.068	0.064	–0.242	0.239
97	Propofol	0.543	0.220	0.323	0.601	–0.057
98	Protriptyline	1.167	1.127	0.040	1.111	0.056
99	Pyrimethamine	0.341	0.236	0.105	0.390	–0.049
100	Quinine sulfate$_{int}$	0.211	0.297	–0.086	–0.068	0.279
101	Rolietracycline	–0.238	–0.367	0.129	–0.323	0.085
102	Salicylamide$_{int}$	–0.826	–0.380	–0.446	–1.012	0.186
103	Sertraline	1.301	0.828	0.473	1.298	0.003
104	Spectinomycin	–0.923	–0.112	–0.810	–0.971	0.048
105	Sulbenicillin	–0.700	–0.598	–0.102	–0.671	–0.029
106	Sulfadiazine	–0.036	–0.420	0.384	–0.100	0.064
107	Sulfadimethoxine$_{ext}$	–0.388	–0.286	–0.102	–0.704	0.316
108	Sulfadoxine	–0.923	–0.440	–0.482	–0.813	–0.110
109	Sulfaethidole$_{int}$	–0.745	–0.517	–0.227	–0.817	0.073
110	Sulfamerazine$_{ext}$	–0.408	–0.367	–0.041	–0.469	0.060
111	Sulfameter	–0.587	–0.238	–0.349	–0.550	–0.037
112	Sulfamethazine	–0.214	–0.339	0.125	–0.234	0.020
113	Sulfamethizole$_{int}$	–0.457	0.123	–0.580	–1.080	0.623
114	Sulfamethopyrazine	–0.659	–0.359	–0.300	–0.590	–0.069
115	Sulfamethoxazole	–0.659	–0.254	–0.405	–0.505	–0.154
116	Sulfamethoxypyridazine	–0.720	–0.845	0.125	–0.732	0.012
117	Sulfinpyrazone	–1.000	0.293	–1.293	–1.016	0.016
118	Sulfisomidine	–0.493	–0.307	–0.187	–0.752	0.259

TABLE I-S. Continued

No	Name	log $(V_d)_{EXP}$	log $(V_d)_{MLR}$	Deviation	log $(V_d)_{ANN}$	Deviation
119	Sulfisoxazole$_{int}$	–0.769	–0.436	–0.332	–0.833	0.065
120	Sulfisoxazole acetyl	0.074	–0.222	0.295	–0.534	0.607
121	Temazepam	–0.007	0.192	–0.199	–0.112	0.105
122	Tetracycline	0.147	0.017	0.129	0.167	–0.021
123	Theobromine	–0.125	–0.120	–0.005	0.090	–0.215
124	Tinidazole	–0.408	–0.323	–0.085	–0.335	–0.073
125	Tramadol$_{int}$	0.479	0.406	0.072	–0.169	0.648
126	Triazolam	0.041	0.394	–0.353	0.038	0.004
127	Trimethoprim$_{ext}$	0.381	0.204	0.178	–0.303	0.684
128	Valproic acid	–0.769	–1.020	0.251	–0.744	–0.025
129	Viloxazine	0.001	0.159	–0.158	0.026	–0.025

Journal of the Serbian Chemical Society
JSCS-info@shd.org.rs • www.shd.org.rs/JSCS
J. Serb. Chem. Soc. 76 (7) 1015–1026 (2011)
JSCS–4180
UDC 544.421.032.4:546.32'82+
547.461.2:543.57
Original scientific paper

Thermal decomposition of potassium titanium oxalate

KARUVANTHODI MURALEEDHARAN* and LABEEB PASHA

Department of Chemistry, University of Calicut, Kerala, 673 635, India

(Received 15 June, revised 14 December 2010)

Abstract: The thermal decomposition of potassium titanium oxalate (PTO) was studied using non-isothermal thermogravimetry at different heating rates under a nitrogen atmosphere. The thermal decomposition of PTO proceeds mainly through five stages forming potassium titanate. The theoretical and experimental mass loss data are in good agreement for all stages of the thermal decomposition of PTO. The third thermal decomposition stage of PTO, the combined elimination of carbon monoxide and carbon dioxide, were subjected to kinetic analyses both by the method of model fitting and by the model free approach, which is based on the isoconversional principle. The model free analyses showed that the combined elimination of carbon monoxide and carbon dioxide and formation of final titanate in the thermal decomposition of PTO proceeds through a single step with an activation energy value of about 315 kJ mol^{-1}.

Keywords: potassium titanium oxalate; non-isothermal thermogravimetry; decomposition kinetics; model free methods.

INTRODUCTION

Metal oxalates have been the subject for a number of thermogravimetric studies, both from a practical and theoretical viewpoint.[1,2] Duval[3] summarized thermogravimetric (TG) data for the drying and ignition temperature of a large number of metal oxalates. Galwey *et al.*[4] identified and discussed studies on the thermal decomposition of silver oxalate. Studies on the thermal decomposition of cobalt oxalate,[5] and manganese(II) oxalate dihydrate and manganese(II) oxalate trihydrate[6] using TG, DTA and X-ray diffraction techniques were reported. Titanate based ceramics have found many applications in material science for different reasons.[7] Even though potassium titanium oxalate (PTO) has many chemical[8] and pharmaceutical[9,10] applications, no kinetic studies on its thermal decomposition have been reported in the literature.

* Corresponding author. E-mail: kmuralika@gmail.com
doi: 10.2298/JSC100615083M

PTO and similar types of compounds have attracted attention due to their technological importance, for instance as precursors of nanostructured titanates. This compound shows an overall decomposition of the type A → B + C, where A and B are solid phases and C is a gas or gases. Such reactions, typically resulting in highly reactive solid products, have attracted a great deal of research interest due to their theoretical and technical relevance.

The objective of this work was to investigate the thermal decomposition of PTO and to determine whether the third thermal decomposition stage, the combined elimination of carbon monoxide and carbon dioxide, occurs through a single stage and to determine the values of the kinetic parameters of this stage. The third thermal decomposition stage of PTO, corresponding to the combined elimination of carbon monoxide and carbon dioxide and the formation of the final titanate, is very important and industry requires measurements of the kinetic parameter for the accurate design of the installations and the treatment conditions, because augmentation of temperature or elongation of reaction time means more cost. The results of the kinetic investigations can also be applied to problems such as the useful lifetime of certain components, oxidative and thermal stability and quality control.[11]

Reaction kinetics by thermogravimetry

Solid-state kinetic data are of practical interest for a large and growing number of technologically important processes. The most common experimental technique employed to study kinetics of thermally activated reactions is thermogravimetry (TG), under the conditions of isothermal and/or non-isothermal conditions. Kinetic studies of the thermal decomposition of solids are one of the most important applications of thermal analysis. In non-isothermal TG, two methods, model fitting and model free analyses have been used for the evaluation of kinetic parameters. Model fitting methods were among the first and most popular methods for kinetic description, because they require only a single heating rate experiment to calculate the kinetic parameters. However, the popularity of these methods has been declining in favour of the isoconversional method of model free approaches.[12–14]

All kinetic methods assume that the isothermal rate of conversion, $\mathrm{d}\alpha/\mathrm{d}t$, is a linear function of the temperature dependent rate constant, $k(T)$, and a temperature independent function of conversion, $f(\alpha)$, which depends on the mechanism of the reaction, that is:

$$\mathrm{d}\alpha/\mathrm{d}t = k(T)f(\alpha) \quad (1)$$

The temperature dependent function $k(T)$ is of the Arrhenius type, can be considered as the rate constant, k, and is obtained from:

$$\mathrm{d}\alpha/f(\alpha) = A/\beta \mathrm{e}^{-E/RT}\mathrm{d}T \quad (2)$$

which upon integration and taking logarithms yields:

$$\ln g(\alpha) = \ln (AE/\beta R) + \ln p(x) \quad (3)$$

where $p(x) = \int_x^\infty (\exp(-x)/x^2)dx$ and $x = E/RT$.

This is the basic form of equation used for analysis of non-isothermal data. This equation can be readily applied once the form of the function $p(x)$ is established.

For kinetic analyses, the main task is to obtain the solution of the above temperature integral. Several methods are available under different approaches, *viz*., integral, differential and approximation, for the evaluation of the temperature integral. However, most of the approximation methods neglect the low temperature end of the temperature integral. It has been reported that two-dimensional quantities significantly influence the approximation methods[15] and the solution of the temperature integral is achieved by numerical integration with respect to a dimensionless activation energy variable.[16]

The model fitting method

The function, $p(x)$ given in Eq. (3) is usually expressed as $p(x) = (\exp(-x)/x^2)$ $Q(x)$, where $Q(x)$ is a rational function that depends on the approximation considered. By considering the gross simplification, $Q(x) = 1$, Eq. (3) becomes:

$$\ln (g(\alpha)/T^2) = \ln (AR/\beta) - E/(RT) \quad (4)$$

Therefore, the most probable kinetic function and the corresponding kinetic parameters, namely the activation energy, are determined by plotting $\ln (g(\alpha)/T^2)$ versus $1/T$. Thus, a plot of $\ln (g(\alpha)/T^2)$ *vs*. $1/T$ must be a straight line for the correct mechanism and non-linear for an incorrect mechanism. Hence, by calculating the value of $\ln (g(\alpha)/T^2)$ using the non-isothermal TG trace for the various rate processes mentioned in Table I and plotting them *vs*. $1/T$, the most probable mechanism corresponding to the linear plot can be determined.

The model free methods

Measuring the evolution of the overall physical properties of a system by thermal methods of analysis provides information on the macroscopic kinetics. Macroscopic kinetics is inherently complex because they include information about multiple steps that are occurring simultaneously. Unscrambling complex kinetics presents a serious challenge that can only be met by kinetic methods that provide means of detecting and treating multi-step processes. Isoconversional methods, based on multiple heating programmes, are the most popular methods that can meet this challenge.[17]

As part of the ICTAC Kinetics Project, M.E. Brown *et al*.[18] performed kinetic analysis of isothermal and non-isothermal data sets provided on a hypothetical simulated process as well as on some actual experimental results for the

thermal decompositions of ammonium perchlorate and calcium carbonate. They applied a variety of computational methods and found that isoconversional and multi-heating rate methods were particularly successful in correctly describing the multi-step kinetics used in the simulated data.

Isoconversional kinetics rest upon evaluating the dependence of the effective activation energy on conversion or temperature and using this dependence for making kinetic predictions and for exploring the mechanism of thermal processes. These methods are based on the single step kinetic equation, Eq. (2), of non-isothermal decomposition and are the quickest way to derive kinetic parameters for complex reactions involving multiple processes.[19] According to the isoconversional principle, at a constant extent of conversion, the reaction rate is a function only of temperature so that:

$$\mathrm{d}(\ln(\mathrm{d}\alpha/\mathrm{d}t))_\alpha/\mathrm{d}T^{-1} = E_\alpha/RT \quad (5)$$

the subscript α designates the value related to a given value of conversion.

The values of the activation energy can be calculated by different methods based on the isoconversional principle. The isoconversional method suggested by Flynn–Wall–Ozawa[20] uses the approximation of the integral equation, which leads to a simple linear equation for the evaluation of activation energy. This method assumes that the conversion function does not change with alteration of the heating rate for all values of α, *i.e.*, measurement of the temperature corresponding to fixed values of α at different heating rate is required. Considering the Doyle approximation of $p(x)$, *i.e.*, $\ln p(x) = -5.3305 - 1.052\ E/(RT)$, Eq. (2) becomes:

$$\ln\beta = \ln(AE/R) - \ln g(\alpha) - 5.3305 - 1.052\ E/(RT) \quad (6)$$

Therefore, when plotting $\ln\beta$ *versus* $1/T$, a straight line with slope $-1.052E/R$ was obtained.

If the values of activation energy (E) determined for various values of α, are almost constant, then certainly the reaction involves only a single step. On the contrary, a change in E with increasing degree of conversion is an indication of a complex reaction mechanism that invalidates the separation of variables involved in the Ozawa, Flynn and Wall analysis.[21] These complications are serious, especially in the case where the total reaction involves competitive reaction mechanisms.[22]

Model free kinetics rests on evaluating the E_α dependence.[23] This dependence is adequate for both theoretical and practical purposes of kinetic predictions. Normally, model free kinetics are not concern with evaluating A and $g(\alpha)$ or $f(\alpha)$ because they are not needed for performing kinetic predictions. In addition, these values are hardly suitable for theoretical interpretation because of the strong ambiguity associated with them. However, these values can be determined within the frameworks of model free kinetics.

EXPERIMENTAL

Materials and instrumentation

AnalaR grade potassium titanium oxalate (PTO) from Merck was recrystalized, dried, the particle size fixed in the range; 90–125 μm mesh and kept in a vacuum desiccator. The thermogravimetric analyses of PTO were performed on a T. A. thermal analyzer, model TGA Q50 V20.2 build 27 in an atmosphere of flowing nitrogen (flow rate 40–60 ml min^{-1}), sample mass: 10 mg, sample pan: alumina, at four different heating rates, *viz*, 5, 10, 15 and 20 K min^{-1}. Duplicate TG runs were performed under similar conditions and the data was found to overlap with each other, indicating satisfactory reproducibility.

Kinetic analyses of the TG data

The non-isothermal thermogravimetric data of PTO were fitted to all the models given in Table I and the kinetic parameters were evaluated for the model which gave the best linear weighted least squares fit. The kinetic data were also evaluated using the isoconversional (model-free) method.

TABLE I. The different reaction models applied to describe the reaction kinetics

SI No.	Reaction model	f(α)	g(α)
1	Power law	$4\alpha^{3/4}$	$\alpha^{1/4}$
2	Power law	$3\alpha^{2/3}$	$\alpha^{1/3}$
3	Power law	$2\alpha^{1/2}$	$\alpha^{1/2}$
4	Power law	$⅔\alpha^{-1/2}$	$\alpha^{3/2}$
5	One-dimensional diffusion	$0.5\alpha^{-1}$	α^2
6	Mampel (first order)	$1-\alpha$	$-\ln(1-\alpha)$
7	Avrami–Erofeev	$4(1-\alpha)[-\ln(1-\alpha)]^{3/4}$	$[-\ln(1-\alpha)]^{1/4}$
8	Avrami–Erofeev	$3(1-\alpha)[-\ln(1-\alpha)]^{2/3}$	$[-\ln(1-\alpha)]^{1/3}$
9	Avrami–Erofeev	$2(1-\alpha)[-\ln(1-\alpha)]^{1/2}$	$[-\ln(1-\alpha)]^{1/2}$
10	Three-dimensional diffusion	$2(1-\alpha)^{2/3}[1-(1-\alpha)^{1/3}]^{-1}$	$[1-(1-\alpha)^{1/3}]^2$
11	Contracting sphere	$3(1-\alpha)^{2/3}$	$1-(1-\alpha)^{1/3}$
12	Contracting area (cylinder)	$2(1-\alpha)^{1/2}$	$1-(1-\alpha)^{1/2}$
13	Second order	$(1-\alpha)^2$	$(1-\alpha)^{-1}-1$

RESULTS AND DISCUSSION

Preview of earlier work on PTO

Broadbent *et al.*[24] reported the results of thermogravimetric and differential thermoanalytical studies on PTO and potassium aluminium oxalate under non-isothermal conditions in air, nitrogen and carbon dioxide atmospheres. They reported that the dehydration of PTO starts at 70 °C and proceeds in several stages until completion at 200 °C. They also observed that the thermal decomposition of PTO was rapid above 275 °C and potassium titanate was formed as the final product. It was shown that PTO is less stable than potassium oxalate.[25] Sairam Patra *et al.*[2] studied the thermal decomposition of anhydrous strontium titanyl oxalate (STO) and found that the thermal decomposition of STO proceeded through a series of complex reactions to form strontium metatitanate at high temperatures. They performed kinetic analysis of the α–*t* data, obtained by cooled gas pressure

measurement under vacuum, of oxalate decomposition in the temperature range 553–593 K and observed that the data fitted the Zhuravlev Equation over almost the entire α-range (0.05–0.92), indicating the occurrence of a diffusion-controlled, three-dimensional rate process, and reported an activation energy value of 164±10 kJ mol^{-1}.

Thermal decomposition pattern of PTO

The thermogravimetric curve for PTO at a heating rate of 10 K min^{-1} in a nitrogen atmosphere is shown in Fig. 1. Similar curves were obtained at all other heating rates (not shown). It was observed that PTO decomposed through five stages as per the scheme given below. The theoretical and experimental mass loss data are in good agreement for all stages of the thermal decomposition of PTO (Table II) as reported earlier.[26,27] Several authors[2,3,7,9] observed this type of phenomena in the decomposition of other titanyl oxalates, *e.g.*, barium titanium oxalate (BTO) and STO:

$$K_2TiO(C_2O_4)_2.2H_2O \rightarrow K_2TiO(C_2O_4)_2 + 2H_2O \quad \text{(up to 450 K)}$$

$$2K_2TiO(C_2O_4)_2 \rightarrow K_4Ti_2O_2(C_2O_4)_3CO_3 + CO \quad \text{(450–520 K)}$$

$$K_4Ti_2O_2(C_2O_4)_3CO_3 \rightarrow K_4Ti_2O_5CO_3.CO_2 + 2CO_2 + 3CO \quad \text{(520–720 K)}$$

$$K_4Ti_2O_5CO_3CO_2 \rightarrow K_4Ti_2O_5CO_3 + CO_2 \quad \text{(720–870 K)}$$

$$K_4Ti_2O_5CO_3 \rightarrow 2K_2TiO_3 + CO_2 \quad \text{(above 870 K)}$$

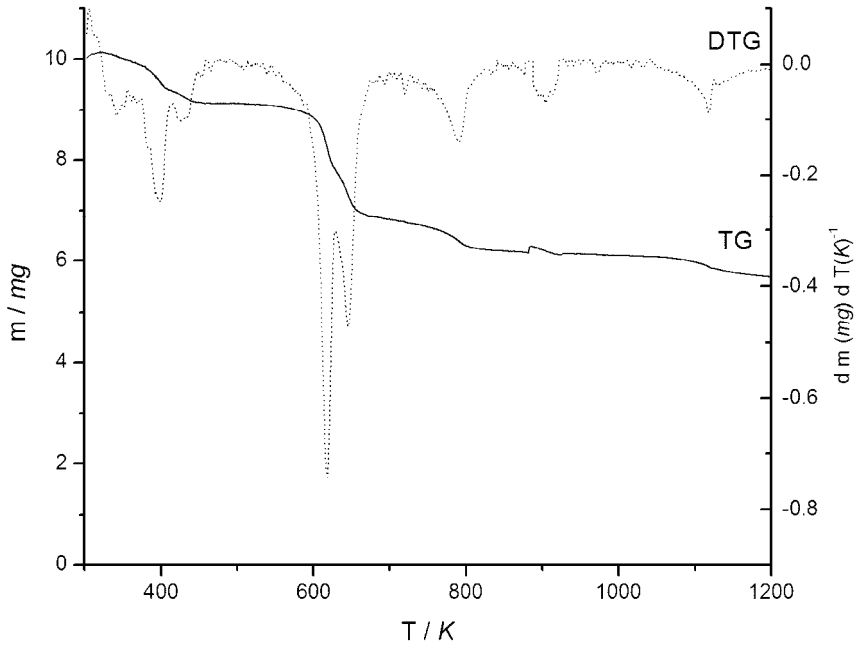

Fig. 1. TG and DTG curve for PTO at a heating rate of 10 K min^{-1}.

TABLE II. Theoretical and experimental mass loss data (%) for the thermal decomposition of PTO at different heating rates

Stage	Decomposition process	Theoretical mass loss %	Heating rate, K min^{-1}			
			5	10	15	20
I	Dehydration	10.17	10.02	10.06	10.11	10.14
II	Elimination of CO	3.95	3.99	3.85	3.91	3.92
III	Elimination of CO and CO_2	24.29	24.01	22.91	24.53	24.16
IV	Elimination of CO_2	6.21	6.12	6.18	6.05	6.25
V	Elimination of CO_2	6.21	6.32	6.22	6.11	6.04

Thermal decomposition and kinetics

It was observed that the thermal decomposition of PTO showed two stages corresponding to the elimination of carbon monoxide in the temperature range 450–490 K and carbon dioxide in the temperature range 690–870 K in addition to three steps corresponding to dehydration (ambient–410 K) and combined elimination of carbon monoxide and carbon dioxide (520–720 K) and the formation of the final titanate (870–1130 K). Elimination of the last molecule of CO_2 was accompanied by melting of potassium titanate (final product), onset around 823 K and a peak around 844 K. The further mass loss observed (Fig. 1) was due to vaporization of potassium titanate. Values of the onset and peak temperatures of the differential TG (DTG) for the different stages of thermal decomposition of PTO at a heating rate of 10 °C min^{-1} are given in Table III. Values of the onset and peak temperatures of the DTG for the third thermal decomposition stage of PTO at different heating rates are given in Table IV.

TABLE III. Onset and peak temperatures (K) of the DTG for different thermal decomposition stages of PTO (heating rate: 10 °C min^{-1})

Decomposition stage	Onset	Peak
I	376	397
II	416	435
III	603	618
IV	764	792
V	1106	1118

The energetic and kinetics of the third thermal decomposition stage, *viz.*, combined elimination of carbon monoxide and carbon dioxide, of PTO in the temperature range 520–720 K was studied and the typical α–T curve for this stage of decomposition (of PTO) is shown in Fig. 2. Similar curves were obtained for all other samples of PTO (not shown). The observed mass loss for this stage is in good agreement with the theoretical value in all cases.

The method of model fitting

The α–T data of the third thermal decomposition stage of PTO was subjected to weighted least squares analysis for all the reaction models given in Table I. All

the plots showed random data points and gave poor correlations. However, reaction models 4,7,8,9,12 and 13 gives comparatively better correlation (> –0.99) for the thermal decomposition of PTO at heating rates of 5, 10, 15 and 20 K min^{-1}. The values of activation energy and correlation coefficient obtained from least squares plots (for all reaction models) are given in Table V.

TABLE IV. Onset and peak temperatures (K) of DTG for the third thermal decomposition stage of PTO at different heating rates

Heating rate, °C min^{-1}	Onset	Peak
5	601	618
10	602	617
15	603	618
20	604	618

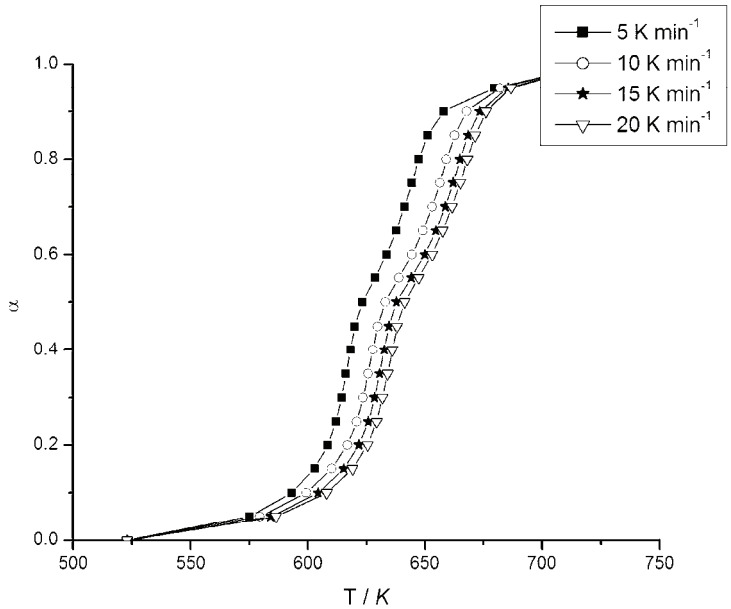

Fig. 2. α–T Plots for the third thermal decomposition stage of PTO at different heating rates.

Examination of Table V reveals that the activation energy values obtained for all models at different heating rates vary widely from 12.6 to 305.2 kJ mol^{-1}. Models which give higher correlations, *i.e.*, models 4, 7, 8, 9, 12 and 13, also showed a huge variation in the value of E (from 32.9 to 305.2 kJ mol^{-1}). However, reaction model 13 gave values of E in the range 298 to 305.2 kJ mol^{-1}. All other models give lower values, which is unacceptable because at this range of temperature a reaction with a low value of E is not feasible. On the other hand, the values of E obtained by using this model are closer to the values obtained from isoconversional methods (301–324 kJ mol^{-1}, Table VI).

TABLE V. Values of the activation energy (E / kJ mol^{-1}) and correlation coefficient (r) obtained for all reaction models at different heating rates

Reaction model	Heating rate, K min^{-1}							
	5		10		15		20	
	E	$-r$	E	$-r$	E	$-r$	E	$-r$
1	21.9	0.9734	20.8	0.9760	20.7	0.9737	21.2	0.9732
2	27.2	0.9772	25.8	0.9795	25.7	0.9774	26.3	0.977
3	35.5	0.9838	33.6	0.9853	33.5	0.9836	34.5	0.9834
4	50.3	0.9940	47.5	0.992	47.4	0.992	48.7	0.9927
5	48.3	0.9852	45.6	0.9817	45.5	0.9825	46.8	0.9835
6	111.1	0.9763	104.8	0.972	104.5	0.9725	107.5	0.9738
7	34.9	0.9924	33.0	0.9923	32.9	0.9911	33.8	0.9913
8	45.0	0.9936	42.6	0.9931	42.4	0.9921	43.6	0.9924
9	63.5	0.9936	60.0	0.9921	59.8	0.9916	61.5	0.9921
10	13.4	0.9376	12.6	0.931	12.6	0.9323	13.0	0.9343
11	27.5	0.989	26.0	0.9861	25.89	0.9862	26.6	0.9871
12	35.8	0.9927	33.8	0.9905	33.70	0.9904	34.6	0.9911
13	305.2	0.9986	298.4	0.9906	298.9	0.9916	301.9	0.9940

TABLE VI. Apparent activation energy (E) obtained for the third thermal decomposition stage of PTO from isoconversional method ($-r$ = 0.9999)

Conversion, %	E / kJ mol^{-1}
10	312.2
20	312.6
30	322.6
40	324.2
50	315.1
60	301.0
70	304.3
80	311.4
90	315.1

The model free approach

The value of the apparent activation energy was also estimated by the isoconversional method suggested by Ozawa, Flynn and Wall[20] for the thermal decomposition of PTO at different percentage conversions by fitting the plots of ln β *vs.* 1/T and the obtained values are given in Table IV. Plots of ln β *vs.* 1/T under the isoconversional method for the thermal decomposition of PTO at all percentages of conversions gave high values of the correlation coefficient (r = = –0.9999) with activation energy values in the range 301–324 kJ mol^{-1}. Typical isoconversional plots for the thermal decomposition of PTO are given in Fig. 3. The plot of activation energy against conversion for the third thermal decomposition stage of PTO is shown in Fig. 4.

As the apparent activation energy values determined for the various values of α of the third thermal decomposition stage of PTO are almost constant, one

can infer that the combined elimination of carbon monoxide and carbon dioxide occurred through a single step.

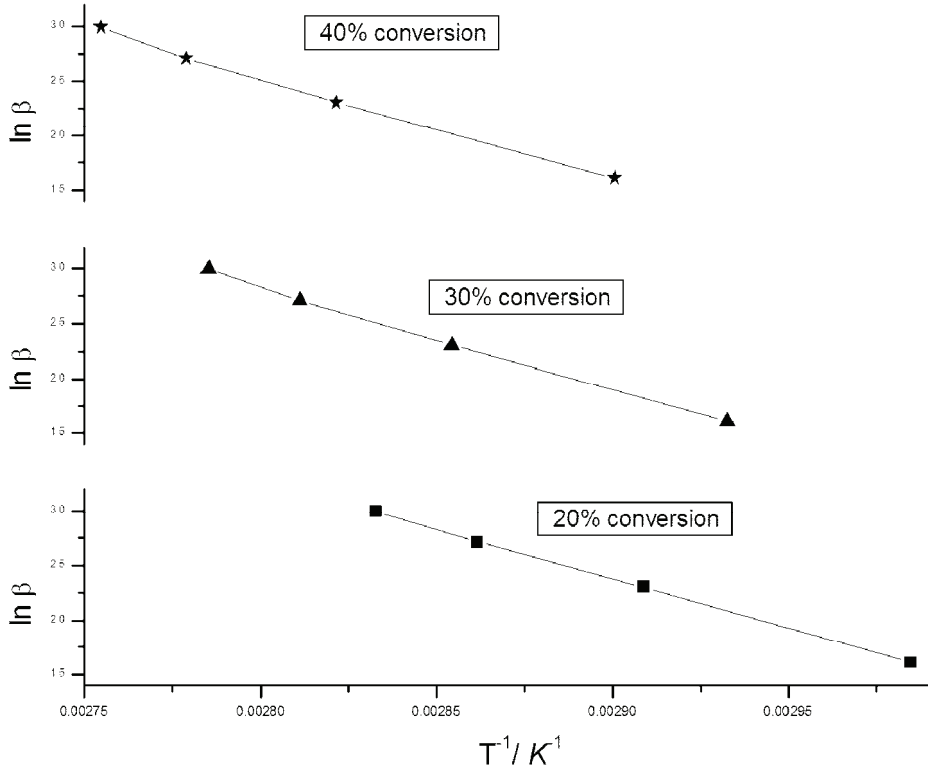

Fig. 3. Typical isoconversional plots for the third thermal decomposition stage of PTO.

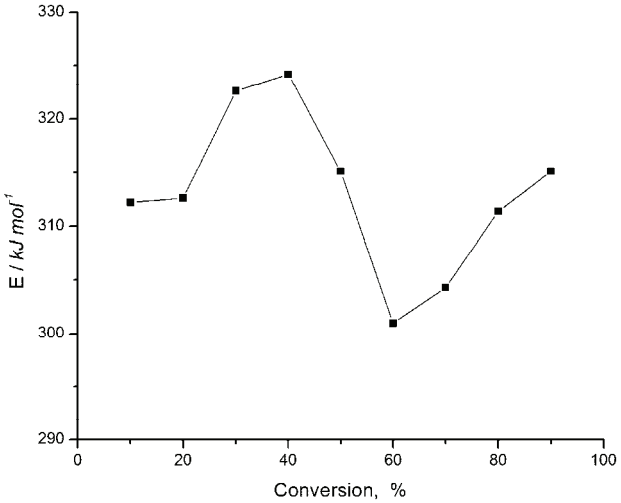

Fig. 4. Plot of activation energy against conversion.

CONCLUSIONS

The kinetic results on the third thermal decomposition stage of PTO showed that the conventional non-isothermal model fitting method gave poor correlations. On the other hand, the correlation was very high for the model free kinetic methods and the value of activation energy showed only negligible variation for different conversions. Reasonably constant values for the apparent activation energy (312±12 kJ mol^{-1}) were obtained over the whole conversion range (10–90 %) for the third thermal decomposition stage by using the isoconversional method. This indicates that the third thermal decomposition stage of PTO, the combined elimination of carbon monoxide and carbon dioxide, proceeds through a single step.

ИЗВОД

ТЕРМИЧКА РАЗГРАДЊА КАЛИЈУМ-ТИТАН-ОКСАЛАТА

KARUVANTHODI MURALEEDHARAN и LABEEB PASHA

Department of Chemistry, University of Calicut, Kerala, 673 635, India

Термичка разградња калијум-титан-оксалата испитивана је неизотермалном термогравиметријом у атмосфери азота при различитим брзинама грејања. Термичка разградња калијум-титан-оксалата одвија се кроз пет ступњева у којима се формира калијум-титанат. Теоријски и експериментални губитак масе су у добром слагању за свих пет ступњева. Трећи ступањ термичке разградње, комбинација елиминације угљен-моноксида и угљен-диоксида, био је предмет кинетичке анализе засноване на два модела – модел фитовања и изоконверзиони модел анализе. Елиминација угљен-моноксида и угљен-диоксида, и стварање титаната при разлагању калијум-титан-оксалата, може се описати јединственим ступњем са укупном енергијом активације која износи 315 kJ mol^{-1}.

(Примљено 15. јуна, ревидирано 14. децембра 2010)

REFERENCES

1. H. S. Gopalakrishnamurhty, M. Subba Rao, T. R. Narayanan Kutty, *J. Inorg. Nucl. Chem.* **7** (1975) 1875
2. B. Sairam Patra, S. Otta, S. D. Battamisra, *Thermochim. Acta* **441** (2006) 84
3. 3. C. Duval, *Inorganic thermogravimetric analysis*, 2nd ed., Elsevier, Amsterdam, The Netherlands, 1963
4. A. K. Galwey, M. E. Brown, *J. Thermal Anal. Cal.* **90** (2007) 9
5. S. Majumdar, I. G. Sharma, A. C. Bidaye, A. K. Suri, *Thermochim. Acta* **473** (2008) 45
6. B. Donkova, D. Mehandjiev, *Thermochim. Acta* **421** (2004) 141
7. V. Ischenko, E. Pippel, R. Köferstein, H. P. Abicht, J. Woltersdorf, *Solid State Sci*. **9** (2007) 21
8. H. S. Gopalakrishnamurhty, M. Subba Rao, T. R. Narayanan Kutty, *J. Inorg. Nucl. Chem.* **37** (1975) 891
9. V. Kuntic, N. Pejic, S. Misic, V. Vukojevic, Z. Vujic, D. Malesev, *J. Serb. Chem. Soc*. **70** (2005) 753
10. N. Pejic, V. Kuntic, D. Malesev, *Pharmazie* **56** (2001) 216

11. K. Celis, I. Van Driessche, R. Mouton, G. Vanhoyland, S. Hoste, *Meas. Sci. Rev.* **1** (2001) 177
12. S. Vyazovkin, C. A. Wight, *Annu. Rev. Phys. Chem.* **48** (1997) 125
13. A. Khawam, D. R. Flanagan, *Thermochim. Acta* **429** (2005) 93
14. A. Khawam, D. R. Flanagan, *J. Phys. Chem. B* **109** (2005) 10073
15. J. Cai, R. Liu, *Solid State Sci.* **10** (2008) 659
16. R.C. Everson, H.W.J.P. Neomagus, N. Delani, *Fuel* **85** (2006) 418
17. *Handbook of thermal analysis and calorimetry, Vol. 5: Recent advances, techniques and applications*, M. E. Brown, P. K. Gallagher, Eds., Elsevier, Amsterdam, The Netherlands 2008
18. M. E. Brown, M. Maciejewski, S. Vyazovkin, R. Nomen, J. Sempere, A. Burnham, J. Opfermann, R. Strey, H. L. Anderson, A. Kemmler, R. Keuleers, J. Janssens, H. O. Desseyn, C.-R. Li, T. B. Tang, B. Roduit, J. Malek, T. Mitsuhashi, *Thermochim. Acta* **355** (2000) 125
19. A. K. Burnham, L. N. Dinh, *J. Thermal Anal. Cal*. **89** (2007) 479
20. T. Ozawa, *Bull. Chem. Soc. Jpn.* **38** (1965) 881
21. T. Ozawa, *J. Thermal Anal.* **2** (1970) 301
22. K. Crissafis, K. M. Paraskevopoulos, D. N. Bikiaris, *Polym. Degrad. Stabil*. **91** (2006) 60
23. S. Vyazovkin, *J. Thermal Anal. Cal*. **83** (2006) 45
24. D. Broadbent, D. Dollimore, J. Dollimore, *Analyst* **94** (1969) 543
25. H. A. Papazian, P. J. Pizzolato, J. A. Patrick, *J. Amer. Cer. Soc.* **54** (1971) 250
26. P. Labeeb, *M. Phil. Thesis*, University of Calicut, India, 2007
27. P. Labeeb, K Muraleedharan, in *Proceedings of the sixteenth national symposium on thermal analysis (THERMANS2008)*, Indian Thermal Analysis Society, Mumbai, India, p. 226.

Journal of the Serbian Chemical Society
JSCS-info@shd.org.rs • www.shd.org.rs/JSCS
J. Serb. Chem. Soc. 76 (7) 1027–1035 (2011)
JSCS–4181
UDC 669.112.227/.228:620.193:669.14.018.8:621.791
Original scientific paper

Corrosion of an austenite and ferrite stainless steel weld

VLADANA N. RAJAKOVIĆ-OGNJANOVIĆ[1]* and BRANIMIR N. GRGUR[2]

[1]*Institute of Hydraulic and Environmental Engineering, Faculty of Civil Engineering, University of Belgrade, Bulevar kralja Aleksandra 73, 11 000 Belgrade and* [2]*Department of Physical Chemistry and Electrochemistry, Faculty of Technology and Metallurgy, University of Belgrade, Karnegijeva 4, 11 000 Belgrade, Serbia*

(Received 26 July, revised 25 December 2010)

Abstract: Dissimilar metal connections are prone to frequent failures. These failures are attributed to the difference in the mechanical properties across the weld, the coefficients of thermal expansion of the two types of steels and the resulting creep at the interface. For the weld analyzed in this research, it was shown that corrosion measurements can be used for a proper evaluation of the quality of weld material and for the prediction of whether or not the material, after the applied welding process, can be in service without failures. It was found that the corrosion of the weld analyzed in this research resulted from the simultaneous activity of different types of corrosion. In this study, electrochemical techniques including polarization and metallographic analysis were used to analyze the corrosion of a weld material of ferrite and austenitic stainless steels. Based on surface, chemical and electrochemical analyses, it was concluded that corrosion occurrence was the result of the simultaneous activity of contact corrosion (ferrite and austenitic material conjuction), stress corrosion (originating from deformed ferrite structure) and inter-granular corrosion (due to chromium carbide precipitation). The value of corrosion potential of –0.53 V shows that this weld, after the thermal treatment, is not able to repassivate a protective oxide film.

Keywords: welding; corrosion; stainless steel.

INTRODUCTION

The welding of dissimilar metals is a very challenging task due to differences in physical, mechanical and metallurgical properties of the parent metals. In order to take full advantage of the properties of different metals, it is necessary to achieve reliable welds between them. The growing availability of new materials and the higher requirements being placed on materials creates a greater need for

* Corresponding author. E-mail: vladana@grf.bg.ac.rs
doi: 10.2298/JSC100726090R

joints and welds of dissimilar metals. When welding ferrite stainless steels, the problem of coarse grains in the weld zone and heat affected zone of fusion welds are encountered with the consequence of low toughness and ductility due to the absence of phase transformation during which grain refinement can occur.[1] When welding austenitic stainless steels, susceptibility to hot cracking in the weld metal and heat-affected zone is of major concern. This cracking occurs primarily due to low-melting liquid phases that allow boundaries to separate under thermal and shrinkage strains during weld solidification and cooling. Austenitic stainless steel welds exhibit some degree of susceptibility to localized corrosion, pitting and crevice corrosion, and in many cases, it is the limiting factor in stainless applications.[2–9] It is generally accepted that delta ferrite when present in small amounts in an austenite matrix is detrimental to pitting resistance as it provides favorable sites for pitting initiation in the weld metal. The corrosion problems commonly associated with welding of austenitic stainless steels are related to both precipitation effects and chemical segregation. The microstructure of the solidified fusion zone of a weld is always subject to segregation during solidification. There are some differences in segregation for different solidification modes of the weld metal. Welding of ferritic to austenitic stainless steels is considered to be a major problem due to difference in coefficient of thermal expansion, which may lead to crack formation at the interface, formation of hard zone close to the weld interface, relatively soft regions adjacent to the hard zone; large hardness difference between the hard and the soft zones and expected differences in microstructure may lead to failures in service. Solid state welding is a possible solution to these problems.[3] For the weld material analyzed in this research, it was shown that detailed microstructural examination and electrochemical and corrosion measurements can be used for the proper evaluation of the quality of the weld material and for the prediction of whether or not the material after the applied welding process could be in service without failures.

EXPERIMENTAL

Materials and welding processes

The nominal chemical compositions of the stainless steel (STS) samples with ferrite and austenite structure used for the welding process are given in Table I.

TABLE I. Nominal chemical composition of used stainless steel materials in mass %

STS Structure	Cr	C	Si	Mn	Ni
Ferrite (X6Cr17)	16.50	0.05	0.35	0.40	–
Austenite (X5CrNi18-10)	18.10	0.04–0.05	0.50	1.10–1.50	8.30–9.20

Welding of austenite and ferrite stainless steel was performed using cooled water and round Cu–Cr electrodes with a contact surface of constant diameter of 1 mm. Welding was performed by placing metal sheets (100 cm^2) in the sample holder. Before welding, the plates were clamped on each end to a heavy backing fixture to prevent deformation.

Characterization techniques

Chemical analysis. Chemical analysis of the materials was performed by the X-Ray fluorescent spectroscopy (XRF) technique using excitation sources of ^{109}Cd and ^{241}Am, according to a modified EPA 6200 method.[10] The quantitative chemical analysis of samples (dissolved in an acidic solution) was performed by atomic absorption spectroscopy (AAS). All results are shown as a mean value of three independent measurements, with a precision of ±0.01 %.

Optical examinations. Optical examination of samples was realized using a NIKON DIC microscope. The "Photoshop" computer program was used to analyzed the microstructure of the pure and welded materials. Before optical examination, the welded material was treated for 72 h in a 3 % solution of NaCl, with the addition of HCl (pH 4). All samples were prepared according to known metallographic procedures, which included mirror polishing and etching in hydrofluoric acid.

Electrochemical corrosion measurements. Electrochemical techniques were applied in order to define the corrosion behavior of all the investigated materials. A three-compartment glass cell was used. Surface area (A) of the working electrodes of pure austenite and ferrite stainless steel was 2 cm^2. Working electrodes of welded stainless steels near the weld (A = = 1 cm^2) was prepared by cutting the austenite and ferrite samples near the weld from the large size (100 cm^2) welded samples. The reference electrode was saturated calomel (SCE, all potentials are reffered to SCE), while the counter electrode was a platinum foil. A mild steel sample was used for comparison.[11,12] The experiments were performed in a 3 % solution of NaCl, with the addition of HCl, to adjust the pH to 4.00 at 25 °C. The corrosion current density was estimated from the intercept of the cathodic slope of the polarization curve with the corrosion potentials. For all electrochemical experiments a potentiostat/galvanostat PAR M273 was used.

RESULTS AND DISCUSSION

Chemical analysis

The XRF spectrum of the austenite and ferrite weld is shown in Fig. 1. XRF Spectrum of this material showed the presence of Cr, Fe, Ni and Mo. As can be seen, the amount of Fe was the highest, then Cr and Ni in small amounts, and finally traces of Mo and Cu in amounts typical for trace elements.

AAS Techniques and clasical gravimetric methods were used to determine the chemical compositions of the used stainless steels. The obtained results are given in Table II.

The results of the XRF and gravimetric analyses for the quantitative determination of the composition of the materials showed that the contents of Cr and Mn were lower than expected, as well as the content of Si in the ferrite sample. AAS Analysis indicated the presence of Ni (0.17 %) in the ferrite sample. The content of carbon and organic impurities according to the AAS measurements was high. The content of carbon was expected to be up to 0.05 %, but according to the chemical analysis it was much higher. Higher contents of carbon and organic impurities, as well as the lower chromium content, were probably the main reason for the appearance of corrosion, especially in ferrite material, resulting from chromium carbide precipitation during the welding.

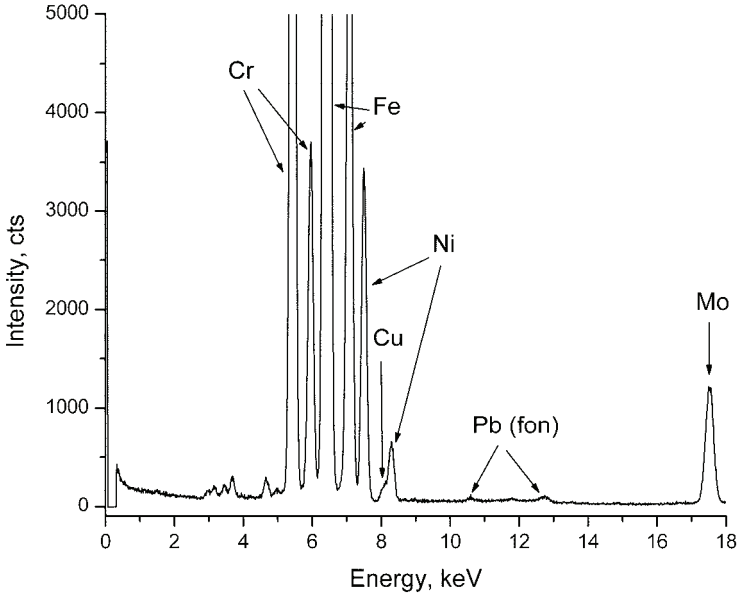

Fig. 1. XRF Spectrum of the austenite and ferrite weld.

TABLE II. Determined chemical composition of the used stainless steel materials in mass %

STS Structure	Cr	Si	Mn	Ni	C
Ferrite	15.5	<0.001	0.30	0.17	0.20–0.5
Austenite	17.8	0.40	1.10	8.00	0.20

Microstructural analysis

Microstructural analysis of ferrite stainless steel. The microstructure of analyzed ferrite stainless steel sample is shown in Fig. 2. The microstructure is not homogenous at the intersection, as shown in the microphotographs of Fig. 3a. The structure consists of ferrite seeds and carbide particles. More than half of the analyzed intersection consists of ferrite seeds, which are polygonal, uniform in size, and have a small-seeded structure, as shown in Fig. 2a. The carbide particles, as shown in Fig. 2b, have a small-seeded structure, globular shape, and were formed between the ferrite seeds.

Microstructural analysis of austenitic stainless steel. The microstructure of the analyzed austenitic stainless steel sample is shown in Fig. 3. The microphotograph at the intersection of this material shows its homogeneous structure, with rough seeds. The size of austenitic seeds is mostly uniform, as shown in Fig. 3a, but there are some very rough seeds, as shown in Fig. 3b.

Microstructural analysis of the weld. A microphotograph of the ferrite and austenite stainless steel weld is shown in Fig. 4. The ferrite material is in the upper part and the austenitic material is in the lower part of the image.

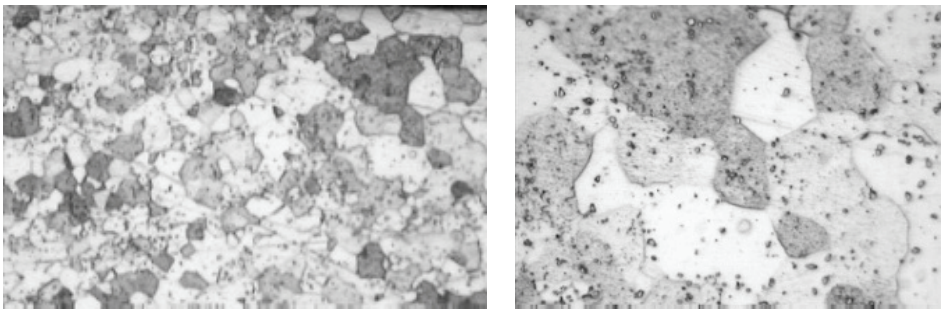

(a) (b)

Fig. 2. Microphotographs of the ferrite stainless steel sample. Magnification: a) 200×; b) 500×.

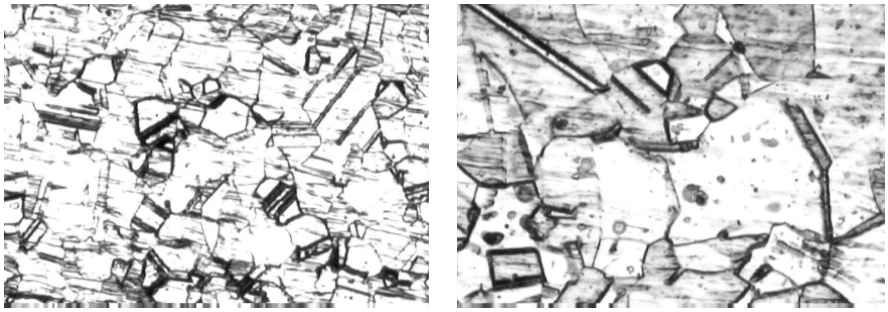

(a) (b)

Fig. 3. Microphotographs of the austenitic stainless steel sample. Magnification: a) 500×; b) 400×.

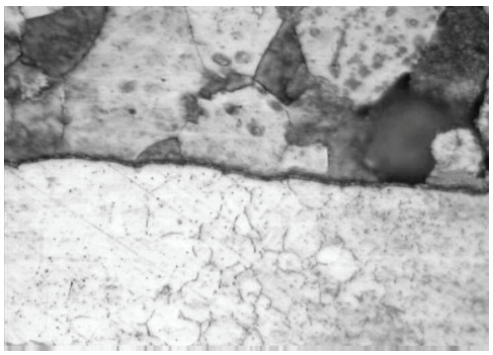

Fig. 4. Microphotograph of the weld sample. Magnification: 500×.

The micrographs of the ferrite part of the analyzed weld sample revealed the existence of inter-granular corrosion, as shown in Fig. 5. This could be connected with precipitation of chromium carbide during the thermal treatment.

When analyzing the microphotographs of the ferrite part near the weld, at a lower magnification, some indications of stress corrosion could be observed, as shown in Fig. 6a and 6b.

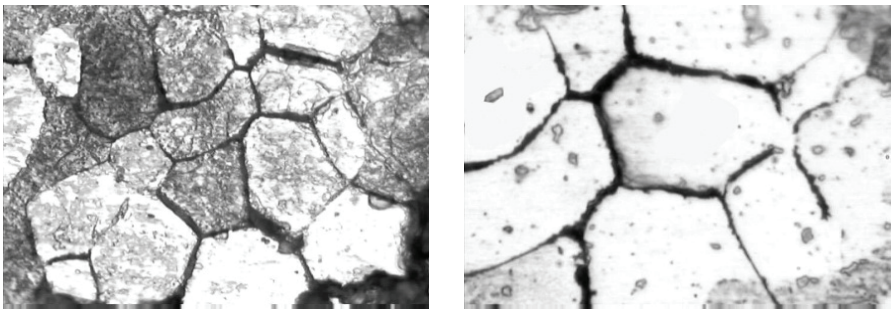

(a) (b)

Fig. 5. Microphotographs of the ferrite part near the weld. Magnification: a) 500×; b) 1000×.

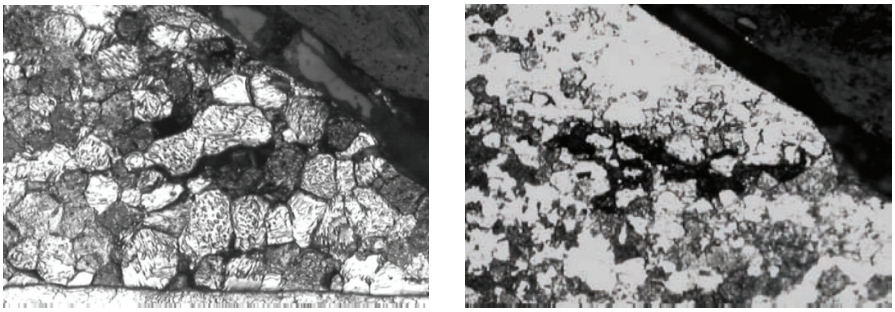

(a) (b)

Fig. 6. Microphotographs of ferrite part near the weld with indication of stress corrosion. Magnification: 200×.

Electrochemical measurements

Electrochemical properties of basic materials. The polarization experiments were performed in a solution simulating the aggressive solution in which the final product could be used.[13] The polarization curves of the ferrite and austenite materials are shown in Fig. 7, together with that of a mild steel sample, shown for comparison.

Both analyzed samples of stainless steel were practically in the passive state with corrosion potentials of approximately –0.2 V. The value obtained for the mild steel in the same solution was –0.53 V, which could be used for comparison. The estimated corrosion current density was 0.08 for austenite and 0.10 μA cm^{-2} the ferrite sample. In comparison, the corrosion current density for the mild steel was 20 μA cm^{-2}.[14]

Corrosion resistance properties of the welded material. The polarization curves for the ferrite and austenitic part of the weld sample are shown in Fig. 8. The austenitic part of the analyzed weld sample remained practically unchanged during welding, according to the metallographic analysis. Even the corrosion potential was unchanged, as presented in Fig. 8. This part has some structural

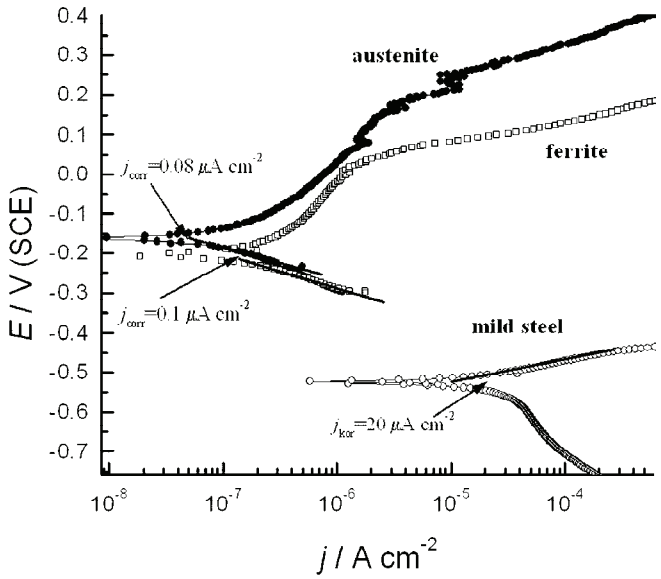

Fig. 7. Polarization curves of the analyzed materials before welding compared to mild steel in 3 % NaCl solution at pH 4.00.

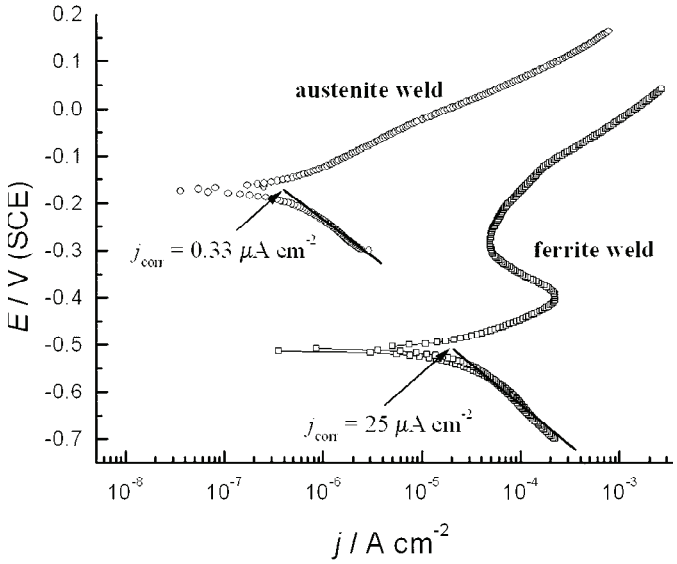

Fig. 8. Polarization curves of the austenitic and ferrite part of the weld sample in 3 % NaCl solution at pH 4.00.

changes which provoke an increase in the estimated corrosion current density. On the other hand, the characteristics of the ferrite material were changed significantly. The corrosion potential of –0.53 V implies that this material after thermal

treatment did not show the ability to repassivate a protective oxide film. The estimated corrosion current density was approximately 75 times higher. This implies that the basic ferrite material was degraded by uncontrolled thermal treatment during the welding process, with the formation of a deformed ferrite structure.[15,16]

CONCLUSIONS

Using the XRF and AAS analytical techniques, it was shown that austenite and ferrite stainless steel had a different chemical composition than the nominal composition. A smaller content of chromium and a higher content of carbon were found than declared. Both materials exhibited relatively good corrosion resistance before welding.

For the ferrite and austenite stainless steel weld analyzed in this study, it was shown that detailed a microstructural examination and electrochemical corrosion measurements could be used for a proper evaluation of the quality of the weld material. With a thorough analysis of the materials used for welds, a prediction of whether the material could be in service without failures can be made.

The weld analyzed in this research showed a tendency towards contact corrosion due to the inadequate welding processes. The corrosion was the result of stress corrosion (from deformation of the basic ferrite structure), and inter-granular corrosion (from carbide precipitation and applied welding method). When improved, the welding process could significantly prevent the appearance of corrosion.

Acknowledgements. The support of the Research Fund of Serbia is gratefully acknowledged.

ИЗВОД

КОРОЗИЈА ЗАВАРЕНОГ СПОЈА АУСТЕНИТНОГ И ФЕРИТНОГ НЕРЂАЈУЋЕГ ЧЕЛИКА

ВЛАДАНА Н. РАЈАКОВИЋ-ОГЊАНОВИЋ[1] и БРАНИМИР Н. ГРГУР[2]

[1]Институт за хидротехнику и водно–еколошко инжењерство, Грађевински факултет, Универзитет у Београду, Булевар краља Александра 73, 11 000 Београд и [2]Катедра за физичку хемију и електрохемију, Технолошко–металуршки факултет, Универзитет у Београду, Карнегијева 4, 11 000 Белоград

Спојеви различитих метала добијених заваривањем склони су пропадању углавном услед појаве различитих видова корозије. Физичко–хемијска, механичка својства, као и коефицијенти топлотног ширења различитих челика најчешћи су узрок пуцања материјала на завареним спојевима. Истраживања у овом раду су показала да се испитивање корозије материјала може користити за процену квалитета спојева заварених материјала. Различите аналитичке, металографске и електрохемијске технике и методе анализе су примењене за испитивање корозије завареног споја нерђајућих челика феритне и аустенитне структуре. Установљено је да до појаве корозије на завареном споју испитиваних материјала превасходно долази услед: контактне корозије, напонске корозије (која потиче од деформисане структуре ферита) и међукристалне корозије (последица излуживања хром-карбида) у феритном делу завареног споја.

(Примљено 26. јула, ревидирано 25. децембра 2010)

REFERENCES

1. I. Serre, J. B. Vogt, *Mater. Design* **30** (2009) 3776
2. Y. Cui, C. D. Lundin, *Mater. Design* **28** (2007) 324
3. V. V. Satyanarayana, G. R. Madhusudhan, T. Mohandasb, *J. Mater. Process. Technol.* **160** (2005) 128
4. A. Joseph, S. K. Rai, T. Jayakumar, N. Murugan, *Int. J. Press. Vessels Pip.* **82** (2005) 700
5. T. G. Gooch, *Weld. J.* **75** (1996) 135
6. B. T. Lu, Z. K. Chen, J. L. Luo, B. M. Patchett, Z. H. Xu, *Corrosion Eng. Sci. Tech.* **38** (2003) 69
7. Z. Fang, Y. Wu, R. Zhu, *Corrosion* **50** (1994) 873
8. D. Rodriguez-Marek, M. Pang, D. F. Bahr, *Metall. Mater. Trans. A* **34** (2003) 1291
9. B. T. Lu, Z. K. Chen, J. L. Luo, B. M. Patchett, Z. H. Xu, *Electrochim. Acta* **50** (2005) 1391
10. EPA 2600, *Method 6200: Field portable X-ray fluorescence spectrometry for the determination of elemental concentrations in soil and sediment*, 2007, http://www.epa.gov/osw/hazard/testmethods/sw846/pdfs/6200.pdf (not anymore accessible)
11. M. M. Popović, B. N. Grgur, V. B. Mišković-Stanković, *Prog. Org. Coat.* **52** (2005) 359
12. V. B. Mišković-Stanković, D. M. Dražić, Z. Kačarević-Popović, *Corrosion Sci*. **38** (1996) 1513
13. M. Kabasakaloglu, I. Kalyoncu, T. Kiyakt, *Appl. Surf. Sci.* **135** (1998) 188
14. ASTM International, *ASTM A 380-99: Standard Practice for Cleaning, Descaling, and Passivation of Stainless Steel Parts, Equipment and Systems*, 2001, http://www.astm.org/DATABASE.CART/HISTORICAL/A380-99E1.htm (accessed July 2011)
15. Hascalik, E. Unal, N. Ozdemir, *J. Mater. Sci.* **41** (2006) 3233
16. J. Wang, C. Li, H. Liu, H. Yang, B. Shen, S. Gao, S. Huang, *Mater. Charact.* **56** (2006) 73.

Journal of the Serbian Chemical Society
JSCS-info@shd.org.rs • www.shd.org.rs/JSCS
J. Serb. Chem. Soc. 76 (7) 1037–1047 (2011)
JSCS–4182
UDC 628.193:582.522+544.723+544.4
Original scientific paper

Biosorption of lead contaminated wastewater using cattails (*Typha angustifolia)* leaves: kinetic studies

YEN LING SHARAIN-LIEW, COLLIN G. JOSEPH* and SIEW-ENG HOW

Industrial Chemistry Programme, School of Science and Technology, University of Malaysia Sabah, Locked Bag No. 2073, 88999, Sabah, Malaysia

(Received 28 June, revised 27 September 2010)

Abstract: In this work, dried leaves of *Typha angustifolia* (TA), also known as the common cattail, were used as an adsorbent in kinetic studies of Pb(II) adsorption from synthetic aqueous solutions. Batch adsorption studies with dried TA leaves were conducted and they were able to adsorb Pb(II) from 100 mL of a 25 mg L^{-1} Pb(II) solution effectively with the optimized dosage of 0.6 g. Adsorption equilibrium was achieved within 8 h with an effective removal of 86.04 %. Adsorption kinetics was further evaluated using four kinetic models, *i.e.*, the pseudo-first order, pseudo-second order, intraparticle diffusion and Elovich model. Fitting of the data was performed based on linear regression analysis. The sorption kinetic data fitted best to the pseudo-second order model with an R^2 of 0.9979, followed closely by the Elovich model with an R^2 of 0.9952. The obtained results showed the adsorption of Pb(II) by TA leaves, which is an abundant biological material, is feasible, cheap and environmentally friendly.

Keywords: adsorption; lead; kinetics; *Typha angustifolia*.

INTRODUCTION

The presence of heavy metals, such as cadmium, chromium and lead, at toxic levels in rivers and streams near human habitats is a cause for concern. According to EPA National Primary Drinking Water Regulations, the maximum contaminant level (*MCL*) for cadmium is 0.005 mg L^{-1}, chromium 0.1 mg L^{-1} and lead 0.015 mg L^{-1}.[1] An overdose of chromium in the body causes infertility while lead results in delayed physical and mental development in children and infants. Mining, tannery, chemical, metallurgical and the electronic and electrical manufacturing industries, which are usually located near rivers and streams, are the main contributors to heavy metal poisoning.[2] Various water treatment methods have been applied to reduce the presence of these metals such as chemical

* Corresponding author. E-mail: collin@ums.edu.my
doi: 10.2298/JSC100628084L

precipitation, flocculation, membrane separation, ion exchange and adsorption.[3–5] However, these methods have limitations and are costly to operate. Precipitation for example produces a large amount of sludge that requires treatment. Membrane filtration and ion exchange, though being effective, require high maintenance. Therefore, an alternative solution needs to be employed. Agricultural and biological waste materials, such as saw dust,[6,7] acorn waste,[8] rice husk ash, [9] tree leaves,[10] cassava[11] and spent grain,[12] have been proven to be cheap and biodegradable adsorbents that provide good loading capacities towards a wide range of heavy metals, such as zinc, lead, cadmium, copper, chromium and nickel. In this work, dried leaves of the narrow leaf cattail plant, *Typha angustifolia* (TA), a common aquatic plant with no economic value in the tropics, was used as a biosorbent for lead removal from synthetic wastewater.

This aquatic perennial plant offers a large amount of biomass that can be used for such purposes. It has been commonly used in constructed wetlands as an effective alternative for the treatment of septic effluents in small villages due its biomass.[13,14] Furthermore, the plants play an important role in metal removal *via* filtration, adsorption and cation exchange through plant-induced chemical changes within the rhizome.[15] This species used in constructed wetlands was reported to achieve a removal of 100 % for copper and zinc and 96 % for nickel.[16] Lead concentrations were found to be 13 mg kg^{-1} in the root and 8 mg kg^{-1} in the leaves of cattail.[17] This proves that the root of aquatic plants generally has a higher uptake capacity of these heavy metals as compared to the leaf. The same trend was also reported by for chromium, nickel, copper and cadmium.[18] Dried cattail leaves demonstrated effectiveness in adsorbing reactive dyes in synthetic wastewater due to the intracellular space within the leaf.[19] Pre-treating cattail leaves with formaldehyde, sulfuric acid and sodium hydroxide was found to improve the removal of Astrazon red 6B and Basilen red M5B by approximately 98 %.[20] In this study, the biosorption kinetics involved in the removal of lead in synthetic wastewater using the dried leaves of TA were investigated.

EXPERIMENTAL

Biosorbent preparation

Mature TA leaves were harvested from a pond in the University Malaysia Sabah campus, Sabah, Malaysia. The leaves are thick, ribbon-like structures which have a D-shaped cross-section showing air channels. These leaves were washed with pipe water to remove dirt and sand before rinsing with distilled water. Then the leaves were placed flat on a clean table to dry before drying in a hot air convection oven (Protech) at 103 °C for 72 h. The dried leaves were then sliced to a thickness of 2 cm and kept in an airtight container.

Pb(II) ion solution

The stock solutions of Pb(II) were prepared by dissolving 1.599 g of $Pb(NO_3)_2$ in 1 L of deionized water with 5 % v/v of HNO_3. Both the $Pb(NO_3)_2$ and HNO_3 were of AR grade obtained from Systerm, Malaysia. The solution was then diluted with deionized water for the

adsorption studies. The natural pH of the solution, pH 5.5, was maintained throughout the experiment. This pH was chosen to simulate the pH of water bodies contaminated with industrial effluents. Fresh dilutions were made prior to each experiment.

Pb(II) metal analysis

The residual concentration of Pb(II) in the solution was determined using a flame atomic absorption spectrophotometer (Perkin Elmer 4100) in triplicate. Each adsorption experiment meanwhile was conducted in duplicate. Single factor analysis of variance (ANOVA, $\alpha = 0.05$) was used to analyze the data in order to ascertain the statistical differences between the expected values and the observed values.

Batch adsorption

Batch adsorption experiments were conducted in 250 mL Erlenmeyer flasks with 100 mL of a 25 mg L^{-1} Pb(II) solution and 0.6 g of dried TA leaves. The mixtures were shaken at room temperature on an orbital shaker (PROTECH) at 170 rpm. The biosorption kinetics involved was examined by varying the contact time of the sorbent (15–540 min). The solution pH was maintained at the natural pH of 5.5 throughout the experiments. The mixtures were then filtered using Advantech No. 9 filter paper and kept in stoppered plastic bottles. The final concentration of Pb(II) was then determined using FAAS. The percentage of removal and the amount of Pb(II) adsorbed onto a unit mass of TA was calculated according to Eqs. (1) and (2), respectively:

$$q = \frac{(c_0 - c_e)V}{m} \tag{1}$$

$$\% \text{ Removal} = \left(\frac{c_0 - c_e}{c_0}\right) \times 100 \tag{2}$$

where q is the amount of Pb(II) adsorbed per gram adsorbent, mg g^{-1}, c_0 is the initial Pb(II) concentration, mg L^{-1}, c_e is the concentration of Pb(II) at equilibrium with the solid phase, mg L^{-1}, V is the volume of the working solution used, L, and m is the mass of sorbent used, g.

Kinetic modeling

Kinetic models were used to determine the sorption mechanism of lead onto TA leaves and the rate controlling steps involved in the process. The kinetic models considered were the pseudo-first order equation, the pseudo-second order equation, the intraparticle diffusion equation and the Elovich equation. The fit of the data was evaluated based on the linear coefficient of determination, R^2 and the Chi-square test. The Chi-square test Equation is given by:

$$\chi_t^2 = \sum \frac{\left(q_{e,exp} - q_{e,calcd}\right)^2}{q_{e,calcd}} \tag{3}$$

where $q_{e,exp}$ is the experimental sorption capacity at equilibrium, mg g^{-1}, and $q_{e,calcd}$ is the calculated sorption capacity at equilibrium according to the respective kinetic model, mg g^{-1}.

Pseudo-first order equation. The pseudo-first order equation is generally expressed as:[7]

$$\frac{dq_t}{dt} = k_1(q_e - q_t) \tag{4}$$

where q_e and q_t are the sorption capacity at equilibrium and at time t, mg g^{-1}, respectively, and k_1 is the rate constant for pseudo-first order sorption, min^{-1}. This model considers the rate of

occupation of adsorption sites to be proportional to the number of unoccupied sites.[10] The integrated form of this equation is:

$$\ln (q_e - q_t) = \ln q_e - k_1 t \quad (5)$$

Pseudo-second order equation. This model is based on the assumption that the rate of sorption is proportional to the square of the number of unoccupied sites.[21] The kinetic rate Equation is expressed as:[7]

$$\frac{dq_t}{dt} = k_2 (q_e - q_t)^2 \quad (6)$$

Integrating Eq. (6) gives:

$$\frac{1}{q_e - q_t} = \frac{1}{q_e} + k_2 t \quad (7)$$

where q_e is the amount adsorbed at equilibrium, mg g^{-1}, while k_2 is the equilibrium rate constant for a pseudo-second order adsorption, g mg^{-1} min^{-1}. A linear graph can be plotted by linearizing Eq. (7) to give Eq. (8) as given below:

$$\frac{t}{q_t} = \frac{1}{k_2 q_e^2} + \frac{t}{q_e} \quad (8)$$

with $k_2 q_e^2 = h$, where h is the initial sorption rate, mg g^{-1} min^{-1}. This model is more likely to predict the behavior over the whole range of adsorption and is in agreement with chemisorptions being the rate controlling step.[12]

Intraparticle diffusion (IPD) equation. In this equation, a fractional approach to equilibrium is evaluated based on the function $(Dt/r^2)^{1/2}$, where r is the radius of an adsorbent particle and D is the effective diffusivity of the adsorbate within the particle. The initial rate is given by the linearized equation of the curve $q_t = f(t^{1/2})$:[7]

$$q_t = k_p t^{1/2} + C \quad (9)$$

where k_p is the IPD rate constant, mg g^{-1} $min^{-1/2}$, while C is the boundary layer thickness, mg g^{-1}. A plot of q_t *versus* $t^{1/2}$ will be linear if IPD is involved in the overall adsorption mechanism. If the line passes through the origin, *i.e.*, $q_t = k_p t^{1/2}$, IPD is the rate controlling step of the process.[22]

The Elovich Equation. The Elovich Equation is given below and is suitable for systems with heterogeneous adsorbing surfaces:[23]

$$\frac{dq_t}{dt} = \alpha \exp(-\beta q_t) \quad (10)$$

The linearized equation is given as:

$$q_t = \frac{1}{\beta} \ln(\alpha\beta) + \frac{1}{\beta} \ln t \quad (11)$$

where α is the initial sorption rate, mg g^{-1} min^{-1} and β is related to the extent of surface coverage and the activation energy of chemisorption, g mg^{-1}.

RESULTS AND DISCUSSION

Effect of adsorbent–adsorbate contact time

The duration of the batch experiments was varied from 15 to 540 min. The concentration of lead solution was 25 mg L^{-1}. Volume of the solution was 100 mL,

while the quantity sorbent was 0.6 g. The pH of the solution was the natural pH of 5.5. As shown in Fig. 1 (1a and 1b), lead exhibited a rapid adsorption during the first 15 min. The percentage removal during that period was 41.96 %. This was then followed by an ongoing slow adsorption until equilibrium was achieved at 480 min. By then, the percentage of removal achieved was 86 %. Therefore, 480 min was fixed as the optimum contact time to attain equilibrium. Thus, the

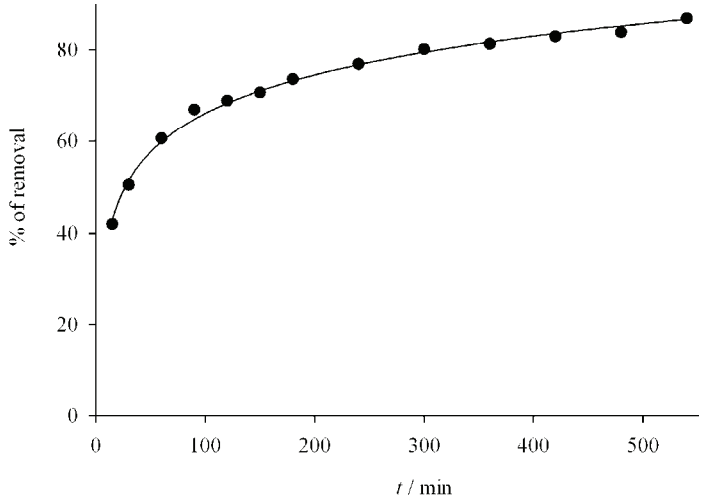

(a)

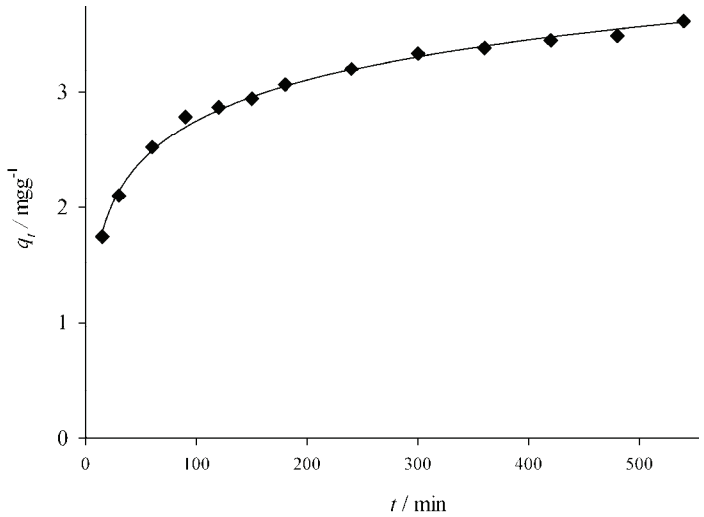

(b)

Fig. 1. a) Percentage removal of lead ions with respect to contact time. b) Amount of metal removed q_t, mg g^{-1} with respect to contact time. The lead concentration remained at 25mg L^{-1}, pH 5.5 with 0.6 g of TA leaves shaken at 170 rpm at room temperature.

experimental sorption capacity at equilibrium q_e, mg g^{-1} was determined to be 3.620 mg g^{-1}.

The adsorption of lead unto TA leaves occurred in two stages; an initial rapid uptake due to surface adsorption onto the TA leaves and a subsequent slow uptake due to diffusion of the lead ions onto the inner surface of the TA leaves. This was similar to the studies reported in the literature using different sorbents.[24–26]

The initial rapid uptake was due to the presence of vacant adsorption sites on the biomass. Sorption thus became less efficient as more adsorption sites were occupied by the metal ions, as shown in the slower stage.[10] This slow uptake is due to the diffusion of metal ions into the inner surfaces of the TA leaves due to repulsive forces between the ions on the leaf surfaces and the bulk phase.[6,9,27] The fast metal uptake by the sorbents is attributed to its highly porous and mesh-like structure that provides a large surface area for the sorption of lead onto the binding sites.[28]

Adsorption kinetics models

The study of the kinetics is important for evaluating the efficiency and mechanism of adsorption. In this study, four models were used, that is, the pseudo-first order, the pseudo-second order, the intraparticle diffusion and the Elovich Equation.

Pseudo-first order. The pseudo-first order kinetic model is commonly used for the adsorption of a solute onto an adsorbent. According to Eq. (5), a linear plot of ln ($q_e - q_t$) *versus t* would confirm the fit of the first order kinetic model. The linear plot is shown in Fig. 2a. Ideally, ln q_e should be equal to the intercept of the plot if the first order model were to be obeyed. In this work, the calculated q_e for the first order model deviated greatly from the experimental q_e value of 1.876 mg g^{-1}. Furthermore, this model gave the lowest correlation coefficient, R^2 using linear regression analysis as compared to the other models (Table I). According to Ho *et al*.,[29] the first-order model does not fit well for the whole range of contact times because the equilibrium sorption capacity, q_e, needs to be known, which is not the case as chemisorptions tends to become slow which causes the amount sorbed to remain significantly smaller than the equilibrium value. Thus, q_e, is usually obtained *via* trial and error. Therefore, the pseudo-first order model did not accurately represent of the adsorption kinetics in this study.

Pseudo-second order. The pseudo-second order model is given by Eq. (8), whereby a plot of t/q_t versus t should give a linear curve. This model is more likely to predict the behavior over the whole range of adsorption and it is in agreement with chemisorption being the rate limiting step.[30] The graphical interpretation of the data is shown in Fig. 2b, while the calculated q_e value, rate constant k_2 (g $mg^{-1}min^{-1}$), the initial sorption rate, h (mg g^{-1} min^{-1}), the correlation

coefficient, R^2 and Chi-square, χ^2, are given in Table I. The correlation coefficient for this model was the best among all the considered models with R^2 = = 0.9979, which shows that the second-order model fits well the data. The calculated χ^2 was also the lowest, further validating that this model best fits the experimental data. The calculated $q_{e\ calc}$ value of 3.719 mg g^{-1} agrees closely with the experimental $q_{e,exp}$ value. This shows that the adsorption of lead onto TA leaves is second-order in nature, *i.e.*, chemisorption is the rate-controlling step involving valence forces *via* the sharing and exchange of electrons between

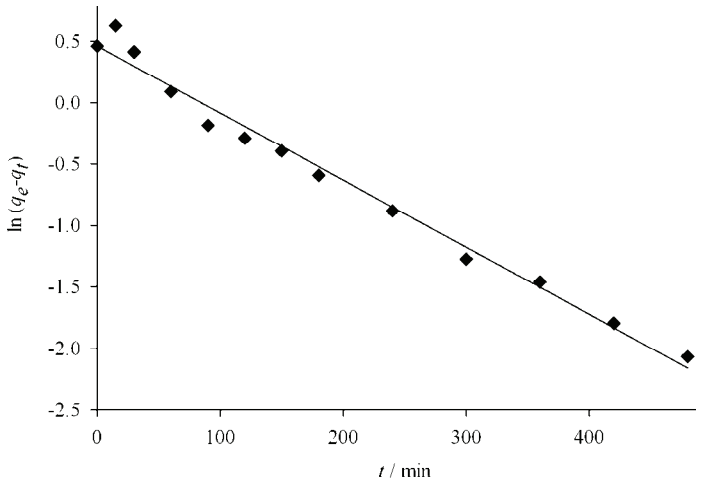

(a)

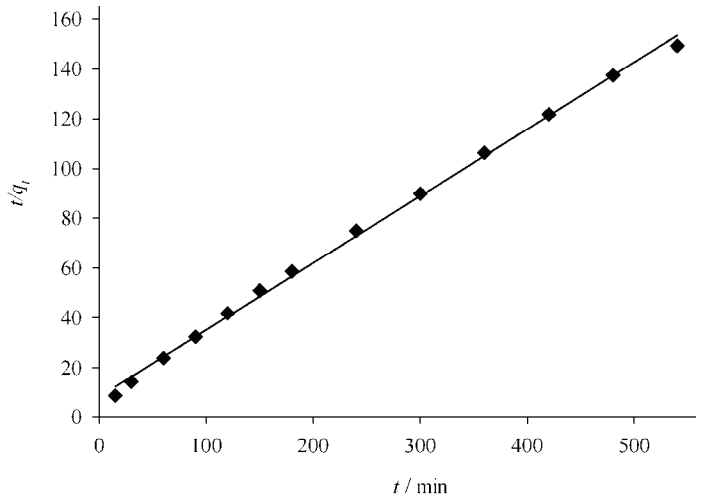

(b)

Fig. 2. a) Pseudo-first order kinetic plot for the adsorption of lead ions at room temperature. b) Pseudo-second order kinetic plot for the adsorption of lead ions at room temperature.

the lead and the TA leaves.[31,32] The obtained rate constant k_2 was 0.0087 g mg^{-1} min^{-1}.

TABLE I. Pseudo-first order, pseudo-second order, intraparticle diffusion and Elovich models for the adsorption of lead ions onto dried TA leaves at room temperature (experimental sorption capacity at equilibrium, $q_{e,exp}$ = 3.620 mg g^{-1})

Model	Parameter	Value for Pb(II)
Pseudo-first order	k_1 /min^{-1}	0.0048
	$q_{e,calcd}$ /mg g^{-1}	1.876
	R^2	0.9324
	χ^2	74.849
Pseudo-second order	k_2 / g mg^{-1}min^{-1}	0.0087
	h / mg g^{-1} min^{-1}	0.032
	$q_{e, calc}$ / mg g^{-1}	3.719
	R^2	0.9979
	χ^2	0.292
Elovich	α / mg g^{-1}min^{-1}	1.313
	B / g mg^{-1}	0.51
	R^2	0.9952
	χ^2	53.342

Intraparticle diffusion (IPD). Adsorption is a multiple step process which is controlled by either one or more steps, *e.g.*, film or external diffusion, pore diffusion, surface diffusion or a combination of more than one step. The IPD model investigates the possibility of diffusion contributing towards the adsorption of lead.

The intraparticle diffusion model is given by Eq. (9). A plot of q_t *versus* $t^{1/2}$ should be linear if IPD is involved in the overall adsorption mechanism and the intraparticle diffusion rate constant k_p, mg g^{-1} min$^{-1/2}$ can be calculated. If the plot of the graph were to pass through the origin, it is concluded that intraparticle diffusion is the rate controlling step.[26] For this work, the plot shown in Fig. 3 exhibits multi-linearity, indicating the adsorption process consisted of three steps as shown by the region k1, k2 and k3.[8,9,26,33] Table II shows the corresponding IPD rate constants, k_p, and the correlation coefficients, R^2, for the individual regions. A trend can be seen whereby $k_{p1}>k_{p2}>k_{p3}$, where k_{p1} is the rate constant for the first region depicting macropore diffusion, while k_{p2} depicts mesopore diffusion for region k2.[9] The rate constant k_{p3} for region k3 has the lowest rate constant as it is the final equilibrium stage where intraparticle diffusion starts to slow down due to the extremely low lead concentration left in the solution.[34] However, as the line does not pass through the origin, IPD is not the rate controlling step.[35] The intercept, C, shown for k1, indicating the boundary layer thickness, shows that rapid adsorption occurs within a very short time.[36]

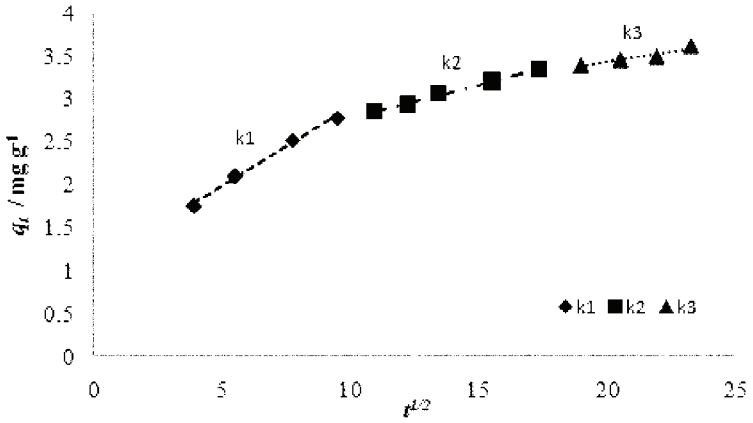

Fig. 3. Intraparticle diffusion kinetic plot for the adsorption of lead ions at room temperature exhibiting multi linearity in the regions k1, k2 and k3.

Table II. Kinetic parameters based on the intraparticle diffusion model exhibiting multi-linearity. Three regions of multi linearity were shown, *i.e.*, k1, k2 and k3

Region	k_p / mg g^{-1} min$^{-1/2}$	R^2
k1	0.1847	0.9946
k2	0.0754	0.9908
k3	0.0452	0.936

The Elovich Equation. The linearized Elovich Equation as shown by Eq. (10) was used to plot a graph of q_t *versus* ln t obtained by integrating Eq. (11) and applying the boundary conditions $q_t = 0$ and $t = 0$.[37] The Elovich Equation gave a high linear correlation, $R^2 = 0.9952$ as shown in Fig. 4. The values of α, the ini-

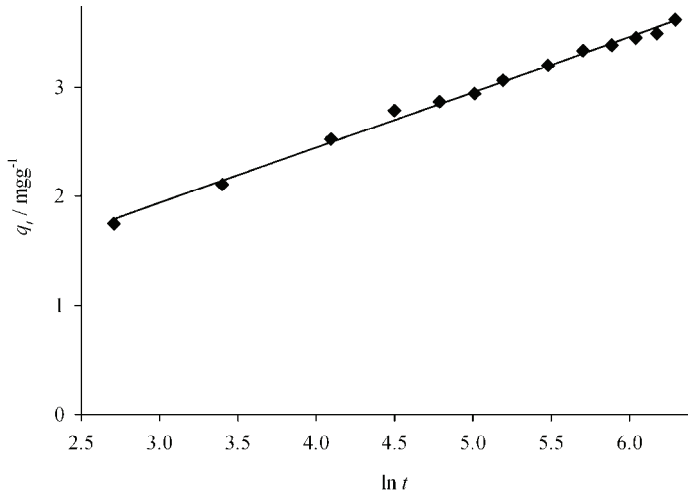

Fig. 4. Elovich kinetic plot for the adsorption of lead ions at room temperature.

tial sorption rate, mg $g^{-1}min^{-1}$ and β, the extent of surface coverage and activation energy of chemisorptions, g mg^{-1}, are given in Table I. This equation is commonly used to determine the kinetics of chemisorption of gases onto heterogeneous solids; thus, it is quite restricted as it only describes a limiting property ultimately reached by the kinetic curve.[38] This is obviously shown by the huge χ^2 value as compared to the other kinetic models (Table I). This proves that the Elovich Equation is not a suitable representation of the adsorption process, despite giving excellent linearity, as was also found by Chang *et al.*[39]

CONCLUSIONS

In this study, the biosorption of lead from contaminated synthetic wastewater using dried TA leaves was successfully performed. The adsorption kinetics, evaluated using pseudo-first order, pseudo-second order, intraparticle diffusion and Elovich models, proved that the pseudo-second order model describe the experimental data the best. This was further validated by the excellent linearity and lowest χ^2 value. Thus, chemisorption was determined as the rate controlling step for the adsorption process. Regarding the Elovich model, the high χ^2 value shows that the model does not fit well with the experimental data despite the excellent linearity. Therefore, the Elovich model was not suitable for describing the adsorption kinetics in this work.

Acknowledgements. This research was financially supported by the Centre of Research and Innovation, University Malaysia Sabah (Grant No. SMS0067-SG-2008), which is gratefully acknowledged.

И З В О Д

БИОСОРПЦИЈА ИЗ ОТПАДНЕ ВОДЕ ЗАГАЂЕНЕ ОЛОВОМ ПОМОЋУ ЛИСТОВА РОГОЗА (*Typha angustifolia*): КИНЕТИЧКА СТУДИЈА

SHARAIN LIEW YEN LING, COLLIN G. JOSEPH и HOW SIEW ENG

Industrial Chemistry Programme, School of Science and Technology, Universiti Malaysia Sabah, Locked Bag No. 2073, 88999, Sabah, Malaysia

У овом раду су коришћени осушени листови биљке *Typha angustifolia* (TA), познате и као рогоз, као адсорбент у кинетичкој студији адсорпције Pb(II) у синтетичким воденим растворима. Спроведена су испитивања шаржном адсорпцијом која су показала да је TA у стању да делотворно адсорбује Pb(II) оптимизованом дозом од 0,6 g. Адсорпциона равнотежа је постигнута у року од 8 часова са ефективним процентом уклањања од 86,04 %. Затим је одређена кинетика адсорпције помоћу кинетичких модела као што су псеудо-први ред, псеудо-други ред, интрачестична дифузија и Elovich модел. Апроксимација тачака је урађена на основу линеарне регресије. Подаци о кинетици сорпције најбоље су одговарали моделу псеудо-другог реда са R^2 од 0,9979 и само мало лошије Elovich моделу са R^2 од 0,9952. Из резултата се може закључити да је адсорпција Pb(II) помоћу TA, који је обилан биолошки материјал, изводљива и повољна за животну средину.

(Примљено 28. јуна, ревидирано 27. септембра 2010)

REFERENCES

1. http://www.epa.gov/safewater/contaminants/index.pdf, dated 8.9.2007
2. L. Sörme, R. Lagerkvist, *Sci. Total Environ*. **298** (2002) 131
3. T. A. Kurniawan, G. Y. S. Chan, W. Lo, S. Babel, *Chem. Eng. J.* **118** (2006) 83
4. V. Mavrov, T. Erwe, C. Blöcher, H. Chimiel, *Desalination* **157** (2003) 97
5. A. Dąbrowski, Z. Hubicki, P. Podkóscielny, E. Robens, *Chemosphere.* **56** (2004) 91
6. T. K. Naiya, P. Chowdhury, A. K. Bhattacharya, S. K. Das, *Chem. Eng. J.* **148** (2009) 68
7. M. Rafatullah, O. Sulaiman, R. Hashim, A. Ahmad, *J. Hazard. Mater*. **170** (2009) 969
8. A. Örnek, M. Özacar, İ. A. Şengil, *Biochem. Eng. J*. **37** (2007) 192
9. V. C. Srivastava, I. D. Mall, I. M. Mishra, *J. Hazard. Mater.* **134(B)** (2006) 257
10. M. R. Sangi, A. Shahmoradi, J. Zolgharnein, G. H. Azimi, M. Ghorbandoost, *J. Hazard. Mater.* **155** (2008) 513
11. A. A. Augustine, B. D. Orike, A. D. Edidiong, *Electro. J. Environ. Agric. Food Chem.* **6** (2007) 2221
12. Q. Li, L. Chai, Z. Yang, Q. Wang, *Appl. Surf. Sci.* **255** (2009) 4298
13. M. P. Ciria, M. L. Solano, P. Soriano, *Biosystems Eng.* **92** (2005) 535
14. J. Liu, Y. Dong, H. Yu, D. Wang, X. Jiakuan, *J. Hazard. Mater*. **147** (2007) 947
15. H. Deng, Z. H. Ye, M. H. Wong, *Environ. Pollut.* **132** (2004) 29
16. T. Manios, E. I. Stentiford, P. Millner, *Chemosphere* **53** (2003) 487
17. A. Sasmaz, E. Obek, H. Hasar, *Ecol. Eng.* **33** (2008) 278
18. D. Demirezen, A. Aksoy, *Chemosphere* **56** (2004) 685
19. S. Nilratnisakorn, P. Thiravetyan, W. Nakbanpote, *Sci. Total Environ*. **384** (2007) 67
20. D. Inthorn, S. Singtho, P. Thiravetyan, E. Khan, *Bioresour. Technol.* **94** (2004) 299
21. S. Schiewer, S. B. Patil, *Bioresour. Technol.* **99** (2008) 1896
22. X. Li, D. Liao, X. Xu, Q. Yang, G. Zeng, W. Zheng, L. Guo, *J. Hazard. Mater*. **159** (2008) 610
23. M. Özacar, İ. A. Şengil, *Process Biochem*. **40** (2005) 565
24. M. T. Uddin, M. A. Islam, S. Mahmud, M. Rukanuzzaman, *J. Hazard. Mater*. **164** (2009) 53
25. J. Zhang, Q. Shi, C. Zhang, J. Xu, B. Zhai, B. Zhang, *Bioresour. Technol*. **99** (2008) 8974
26. R. Han, J. Zhang, P. Han, Y. Wang, Z. Zhao, M. Tang, *Chem. Eng. J*. **145** (2009) 496
27. Y. Liu, X. Chang, Y. Guo, S. Meng, *J. Hazard. Mater*. **135(B)** (2006) 389
28. A. Saeed, M. W. Akhter, M. Iqbal, *Sep. Purif. Technol.* **45** (2005) 25
29. Y. S. Ho, G. McKay, *Trans. Inst. Chem. Eng.* **76(B)** (1998) 332
30. Y. S. Ho, G. McKay, *Resour. Conserv. Recycl*. **25** (1999) 171
31. Y. S. Ho, G. McKay, *Process Biochem.* **34** (1999) 451
32. F. Wu, R. Tseng, R. Juang, *Chem. Eng. J.* **151** (2009) 1
33. J. Choi, N. Choi, S. Lee, D. Kim, *J. Colloid Interface Sci.* **314** (2007) 367
34. F. Wu, R. Tseng, R. Juang, *J. Colloid Interface Sci*. **283** (2005) 49
35. W. S. W. Ngah, S. Fatinathan, *Chem. Eng. J.* **143** (2008) 62
36. F. Wu, R. Tseng, R. Juang, *Chem. Eng. J.* **153** (2009) 1
37. F. Wu, R. Tseng, R. Juang, *Chem. Eng. J.* **150** (2009) 366
38. Y. Ho, *J. Hazard. Mater*. **136(B)** (2006) 681
39. C. Chang, C. Chang, K. Chen, W. Tsai, J. Shie, Y. Chen, *J. Colloid Interface Sci*. **277** (2004) 29.

Journal of the Serbian Chemical Society
JSCS-info@shd.org.rs • www.shd.org.rs/JSCS
J. Serb. Chem. Soc. 76 (7) 1049–1055 (2011)
JSCS–4183
UDC 546.86'226+621.315.59:544.526.5:667.287.6
Short communication

SHORT COMMUNICATION

Photodegradation of Naphthol green B in the presence of semiconducting antimony trisulphide

RAKSHIT AMETA[1], PINKI BALA PUNJABI[2] and SURESH C. AMETA[2]*

[1]*Department of Pure & Applied Chemistry, University of Kota, Kota - 324010 (Rajasthan) and*
[2]*Department of Chemistry, M. L. Sukhadia University, Udaipur -313002 (Rajasthan) India*

(Received 25 April, revised 24 June 2010)

Abstract: Different methods of wastewater treatment are being used for the removal of dyes from their solution, but in most of the cases, either homogeneous catalysts or different adsorbents are used. These methods have their own merits and demerits. In the present work, antimony trisulphide was used as a heterogeneous catalyst. The effects of different parameters on the rate of the reaction were observed, such as pH, concentration of dye, amount of semiconductor and light intensity. A tentative mechanism is proposed in which the role of hydroxyl radical as an active oxidizing species is shown for degradation of Naphthol green B.

Keywords: semiconductor; photocatalyst; Naphthol Green B; hydroxyl radical; antimony trisulphide.

INTRODUCTION

In the entire world, everyone is facing a major problem of water pollution by industrial effluents. Although industries are obliged to make their effluents harmless by different methods, water pollution is continuously increasing. Although researchers are already employing different methods for the removal of dye from wastewater, photochemistry may still play an important role for solving this problem, as sunlight is readily available all over the world. Different heterogeneous catalyst may be used as photocatalysts for the removal of different dyes. Photodegradation of Methylene blue using sunlight and TiO_2 was investigated by Nogueria and Jardin.[1] Mercury(II) ions were photocatalytically eliminated from aqueous solutions in presence of ZnO powder.[2] Ameta *et al.*[3] investigated the effect of surfactants on the photobleaching of Basic Blue-24. Cao and Suils[4] reported the photo-oxidation of propan-2-ol to acetone using amorphous manga-

* Corresponding author. E-mail: ameta_sc@yahoo.com
doi: 10.2298/JSC100425082A

nese oxide as catalyst. Sharma *et al.*[5] observed the photocatalytic bleaching of Crystal violet in aqueous suspensions of zinc oxides. Fu *et al.*[6] reported the photoreduction of hexachloroplanitate(IV) on cadmium sulphide while Wang and Zhuang.[7] performed the photocatalytic reduction of Cr(VI) over CdS powder under visible light. The photochemical reduction of Cr(VI) on CdS was investigated by Domenech and Munoz.[8]

Mansilla and Villasnov[9] investigated the ZnO-catalysed photodegradation of Kraft-Black liquor, which is an effluent from pulp and paper industries. ZnS was used for the photoreduction of carbon dioxide by Kanemoto *et al.*[10] Ameta *et al.*[11] used semiconducting iron(III) oxide as the photocatalyst for the bleaching of Methylene blue, Crystal violet and Malachite green dyes. The photocatalytic reduction of the dye Methylene Blue by Bi_2S_3/CdS nanocomposites was realised by Kobasa and Tarasenko.[12] Biodegradation of Rose Bengal by *Phanerochaete chrysosporium* was performed by Gogna *et al.*[13] The mechanism of the photoreduction of silver ions over tungsten oxide was reported by Sviridov and Kulak.[14] The photoreduction of carbon dioxide and water into formaldehyde and methanol in aqueous suspensions of WO_3 was studied by Blajeni *et al.*[15]

EXPERIMENTAL

Antimony trisulphide was selected as the heterogeneous photocatalyst as it is coloured and thus absorbs a major part of sunlight

A 1.0×10^{-3} M stock solution of Naphthol green B was prepared by dissolving 0.0878 g of the dye in 100.0 mL doubly distilled water. The optical density (*O.D.*) of this dye solution at λ_{max} = 635 nm was determined using a Systronics Model 106 spectrophotometer.

The dye solution was placed in equal amounts into four beakers (50 mL of the dye solution was kept in four beakers):

i) The first beaker containing Naphthol green B solution was kept in the dark.

ii) The second beaker containing Naphthol green B solution was exposed to the light of a 200 W tungsten lamp.

iii) The third beaker containing Naphthol green B solution and 0.10 g antimony trisulphide was kept in dark.

iv) The fourth beaker containing Naphthol green B solution and 0.10 g antimony trisulphide was exposed to the light of a 200 W tungsten lamp.

After keeping these beakers for a few hours, the optical density of the solution in each beaker was measured (visible light spectrum). It was found that the solutions of the first three beakers had almost the same optical density as their initial value while the solution of the fourth beaker had decreased. From this observation, it becomes clear that this reaction required the presence of both light and the semiconductor antimony trisulphide. Hence, this reaction is photocatalytic in nature.

In further experiments, the pH of the dye solution, the concentration of Naphthol green B, the amount of antimony trichloride, and the light intensity were varied.

RESULTS AND DISCUSSION

An aliquot of 2.0 mL was taken out from the reaction mixture and its optical density was observed at 635 nm at regular time intervals. It was observed that the amount of Naphthol green B decreased with increasing light exposure time.

A plot of log *O.D.* against time was found to be linear. The rate constant was calculated from the expression:

$$k = 2.303 \times \text{slope}$$

The data from a typical run are given in Table I.

TABLE I. The results of a typical photodegradation experiment. [Naphthol green B] = = 1.50×10^{-5} M; antimony trisulphide amount = 0.18 g in 50 mL; light intensity = 50.0 mW cm^{-2}; pH 8.0; rate constant, $k = 8.95 \times 10^{-4}$ s^{-1}

Time, min	Optical density (*O.D.*)	2+ log *O.D.*
0.0	0.407	1.6096
5.0	0.245	1.5092
10.0	0.245	1.3892
15.0	0.188	1.2553
20.0	0.132	1.1206
25.0	0.100	1.0000
30.0	0.076	0.8808
35.0	0.058	0.7634
40.0	0.044	0.6434
45.0	0.033	0.5185
50.0	0.025	0.3979
55.0	0.019	0.2787
60.0	0.014	0.1461

Effect of pH

The pH of the solution is likely to affect the degradation of Naphthol green B. The effect of pH on the rate of degradation of Naphthol green B was investigated in the pH range 5.0–10.0. The results are reported in Table II.

On increasing the pH of the reaction medium above its optimum value (pH 8.0), the semiconductor surface becomes covered with adsorbed hydroxyl ions, making it negatively charged. This negatively charged surface will not permit a close approach of dye molecules near the semiconductor surface and therefore the reaction rate is retarded.

Effect of dye concentration

The effect of variation of the dye concentration was studied by taking different concentrations of Naphthol green B. The obtained results are tabulated in Table III.

The rate of photocatalytic degradation of dye increased with increasing dye concentration up to a certain value. Beyond this concentration, the rate of photo-

catalytic degradation started to decrease. This may be explained by the fact that as the concentration of dye was increased, more dye molecules were available for excitation and consecutive energy transfer and as a result, an increase in the rate was observed. A decrease in rate of photocatalytic degradation was observed with further increase in the dye concentration, which may be attributed to the fact that the dye started acting as an internal filter for the incident light and hence did not permit the desired light intensity to reach and excite a large number of the semiconductor particles. Thus, a corresponding decrease in the rate of photocatalytic degradation of the dye was observed.

TABLE II. Effect of pH on the rate of the photodegradation of the dye. [Naphthol green B] = = 1.50×10^{-5} M; antimony trisulphide amount = 0.18 g in 50 mL; light intensity = 50.0 mW cm^{-2}

pH	k / 10^{-4} s^{-1}
5.0	5.28
5.5	5.63
6.0	6.57
6.5	6.77
7.0	6.99
7.5	7.97
8.0	8.95
8.5	6.67
9.0	6.07
9.5	5.33
10.0	4.60

TABLE III. Effect of Naphthol green B concentration on the rate of its photodegradation. Light Intensity = 50.0 mW cm^{-2}; antimony trisulphide amount = 0.18 g in 50 mL; pH 8.0

[Naphthol green B]$\times10^5$, M	k / 10^{-4} s^{-1}
0.4	1.01
0.6	2.10
0.8	4.24
1.0	6.41
1.5	8.95
2.0	8.39
2.5	7.63
3.0	7.10
3.5	6.71
4.0	5.47
4.5	3.10

Effect of amount of semiconductor

The amount of semiconductor is also likely to affect the process of dye degradation and hence, different amounts of photocatalyst were used. The results are reported in Table IV.

TABLE IV. Effect of the amount of semiconductor on the rate of photodegradation of the dye. [Naphthol green B] = 1.50×10^{-5} M; pH 8.0; light intensity = 50.0 mW cm^{-2}

Antimony trisulphide amount (in 50 mL solution, g	k / 10^{-4} s^{-1}
0.04	0.94
0.06	1.86
0.08	2.48
0.10	4.10
0.12	5.59
0.14	6.99
0.16	8.24
0.18	8.95
0.20	8.92
0.22	8.94
0.24	8.96

The rate constants for the photodegradation of the dye initially increased with increasing amount of antimony trisulphide but after reaching a certain fixed value of the semiconductor, they became virtually constant. This may be because as the amount of semiconductor was increased, the exposed surface area increased and as a result, the rate of the reaction increased. However, after a certain limit, if the amount of semiconductor was further increased, there would be no corresponding increase in the exposed surface area of the photocatalyst. Furthermore, any increase in the amount of the semiconductor after this particular amount would only increase the thickness of the layer at the bottom of the vessel, once the bottom of the reaction vessel was completely covered by the semiconductor. This multilayer structure would not permit all the semiconductor particles to be exposed to light and as such, the rate of the reaction became almost constant. Thus, saturation like behaviour was observed. This was further confirmed by stirring the reaction mixture, whereby the rate again increased. This point of saturation depends on the dimensions of the vessel. It was shifted to higher values when large vessels were used and to the lower ones with smaller vessels.

Effect of light intensity

To investigate the effect of the light intensity on the photocatalytic degradation of Naphthol green B, the distance between the light source and the exposed surface area was varied. The intensity of light at each distance was measured using a Suryamapi (CEL Model SM 201). The results are summarized in Table V.

The rate of photocatalytic degradation of the dye was found to increase with increasing light intensity, but after a certain limit, the rate decreased with further increasing light intensity. An increase in the intensity of light increases the number of photons striking the semiconductor particles per unit area per unit time. As a result, more electron–hole pairs are generated, which results in an

overall increase in the rate of the reaction. However, at higher light intensities, some thermal side reactions may also commence and hence, the rate of photocatalytic degradation decreases on increasing the light intensity.

TABLE V. Effect of the light intensity on the rate of photodegradation of the dye. [Naphthol green B] = 1.50×10^{-5} M; antimony trisulphide amount = 0.18 g in 50 mL; pH 8.0

Light intensity[a], mW cm^{-2}	k / 10^{-4} s^{-1}
20.0	5.11
30.0	5.97
40.0	6.25
50.0	8.95
60.0	8.52
70.0	8.06
80.0	7.90

[a]60 % of light was absorbed by the system; the results are given only for the incident light

It has been observed that the rate of photocatalytic degradation of the dye increased on increasing the pH of the reaction medium (pH 8.0; Table II). The optimum was observed in alkaline medium. This indicates that hydroxyl radicals were the reactive species in the photocatalytic degradation of the dye, as the hydroxyl ions would be converted to hydroxyl radicals by the photogenerated holes:

$$SC \xrightarrow{h\nu} h^+(VB) + e^-(CB) \quad (1)$$

$$h^+ + OH^- \rightarrow {}^\bullet OH \quad (2)$$

$${}^\bullet OH + \text{Dye} \rightarrow \text{Products} \quad (3)$$

The participation of $^\bullet$OH radicals as the active oxidizing species in the photocatalytic bleaching of the dye was confirmed by performing the studied reaction in presence of an $^\bullet$OH radical scavenger, *i.e.*, propan-2-ol, whereby the rate of the reaction was drastically reduced.

CONCLUSIONS

The Naphthol green B in the solution was degraded using the semiconducting antimony trisulphide as a photocatalyst. The role of $^\bullet$OH radicals, which is responsible for degradation of the dye, was confirmed by performing the reaction in the presence of an $^\bullet$OH radical scavenger.

И З В О Д

ФОТОДЕГРАДАЦИЈА НАФТОЛ ЗЕЛЕНОГ Б У ПРИСУСТВУ ПОЛУПРОВОДНИКА АНТИМОН-ТРИСУЛФИДА

RAKSHIT AMETA[1], P. B. PUNJABI[2] и SURESH C. AMETA[2]

[1]Department of Pure & Applied Chemistry, University of Kota, Kota - 324010 (Rajasthan) и [2]Department of Chemistry, M. L. Sukhadia University, Udaipur -313002 (Rajasthan) India

Разне методе се тренутно користе за уклањање боја из раствора, али у већини случајева се користе или хомогени катализатори или адсорбенти. Ове методе имају својих предности и недостатака. У изложеном раду је коришћен антимон-трисулфид као хетерогени катализатор. Испитивано је неколико параметара који утичу на брзину реакције, као што су pH, концентрација боје, количина полупроводника и интензитет светла. На крају је изложен претпостављени механизам у којем је приказана улога хидроксил радикала у деградацији нафтол зеленог Б.

(Примљено 25. априла, ревидирано 24. јуна 2010)

REFERENCES

1. R. E. P. Nogueria, W. F. Jardin, *J. Chem. Educ.* **70** (1993) 861
2. J. Domenech, A. Prieto, *Electrochim. Acta* **31** (1986) 1317
3. R. Ameta, C. Kumari, C. V. Bhat, S. C. Ameta, *Ind. Quim.* **33** (1998) 36
4. H. Cao, S. L. Suils, *J. Am. Chem. Soc.* **116** (1994) 5335
5. A. Sharma, P. Rao, R. P. Mathur, S. C. Ameta, *J. Photochem. Photobiol., A* **86** (1995) 197
6. H. Fu, G. Lu, S. Li, *J. Photochem. Photobiol. A* **114** (1998) 88
7. Z. H. Wang, Q. X. Zhuang, *J. Photochem. Photobiol., A* **75** (1993) 105
8. J. Domenech, J. Munoz, *J. Chem. Res. Synop.* **106**, (1987)
9. H. D. Mansilla, J. Villasnov, *J. Photochem. Photobiol., A* **78** (1994) 267
10. K. Kanemoto, J. Shiragoni, C. Pac, S. Yanagida, *J. Phys. Chem.* **96** (1992) 3521
11. R. Ameta, J. Vardia, P. B. Punjabi, S. C. Ameta, *Ind. J. Chem. Tech.* **13** (2006) 114
12. I. M. Kobasa, G. P. Tarasenko, *Theor. Exp. Chem.* **38** (2002) 255
13. E. Gogna, R. Vohra, P. Sharma, *Lett. Appl. Microbiol.* **14** (2008) 58
14. D. V. Sviridov, A. I. Kulak, *High Energy Chem.* **24** (1990) 195
15. B. A. Blajeni, M. Halmann, J. Manassen, *Sol. Energy* **25** (1980) 165.